Probing the nonequilibrium dynamics of driven soft matter

A thesis submitted for the degree of

Doctor of Philosophy

in the

Jawaharlal Nehru University

by

Rajkumar Biswas



Soft Condensed Matter Group
Raman Research Institute
Bangalore, INDIA

December 2022

Dedicated to

My Parents and My Sisters

Declaration

I hereby declare that the work presented in this thesis is completely original. This research work is supervised by Professor Ranjini Bandyopadhyay at the Raman Research Institute in Bengaluru, India. This dissertation represents my own work, unless otherwise specified. No part of this thesis has been submitted elsewhere for the award of any degree, diploma, membership, fellowship, or other similar title from any institution or university. I also certify that this thesis has been passed through the **Turnitin** plagiarism detection system.

Prof. Ranjini Bandyopadhyay **Rajkumar Biswas**

(Thesis Supervisor)

Soft Condensed Matter Group

Raman Research Institute

Bengaluru-560080, India

Copyright © Rajkumar Biswas, 2022.

Certificate

This is to certify that the thesis entitled "**Probing the nonequilibrium dynamics of driven soft matter**" submitted by **Rajkumar Biswas** for the award of the degree of Doctor of Philosophy of Jawaharlal Nehru University is his original work. This has not been published or submitted to any other University for any other Degree or Diploma.

Prof. Tarun Souradeep
Director
Raman Research Institute
Bengaluru-560080, India

Prof. Ranjini Bandyopadhyay
(Thesis Supervisor)

Acknowledgements

I would like to thank my thesis advisor, Professor Ranjini Bandyopadhyay, for the opportunity to work with her, as well as for her excellent guidance, constant support, and encouragement throughout the duration of my thesis work. I am grateful to her for encouraging independent thought, believing in my abilities, and providing a friendly lead whenever necessary. I am also grateful to the members of my advisory committee, Prof. Sayantan Majumdar and Prof. V. A. Raghunathan, for their encouragement and assistance with numerous academic issues.

I would like to thank Dr. Debasish Saha for instructive discussions related to the work presented in Chapter 3. I would like to thank Vaivhab RS Parmar and Anson G Thambi for their invaluable assistance in Chapter 4 and 5, encompassing experimental setup, data acquisition, and writing manuscript. I would like to thank Arsalan Ashraf for a calibration code. I want to thank Prof. Smarajit Karmakar and his student Anoop Mutneja for providing the molecular dynamics simulation codes used in Chapter 6 and their useful insights for the project. The project in Chapter 7 is conducted in collaboration with Anson G Thambi. I want to thank Prof. Abhishek Dhar for providing laboratory facilities at ICTS and for engaging in valuable discussions. I want to thank Prof. Sandeep Kumar for letting me use the chemistry lab facilities. I would also like to thank Prof. Y. Hatwalne, Prof. R. Pratibha, Prof. Arun Roy, Dr. Gautam V. Soni for their helpful discussions and encouragement.

I am extremely grateful to my senior lab mates, Dr. Paramesh Gadige and Dr. Sanjay Kumar Behera for their patient assistance in getting me acquainted

with the experimental setup and insightful discussions. I enjoyed the company and assistance of my lab mates Zaibudeen, Tamal, Chandeshwar, Palak, Venketesh, Vaibhav, Yogesh, Anson, Sonali, Jasim, Sayantan, Vipin, Ganesh, Riddhika, and Tonmoy. I'd like to thank Mr. K. M. Yatheendran for his assistance with confocal, scanning electron microscopy, and cryo-electron microscopy imaging. Mrs. K. N. Vasudha assisted me with the differential scanning calorimetry experiments, and I am grateful to her. I appreciate everyone in the RRI workshop for all of their assistance.

I would like to thank K. Radhakrishna and Mrs. M.S. Chaithanya, the secretaries of the SCM group, for all the help they have provided me with logistics like purchasing chemicals and lab components, coordinating transportation, filing travel claims, and more. Many thanks to Mr. Raja and Mr. Murali for all of their hard work each and every day. All of the library employees have been very helpful, and I appreciate all of their efforts. For all of the assistance I received from the accounts and purchases teams, I am very grateful. I appreciate the help that I have received from the staff in the computer lab over the years with things like software installations and internet connectivity.

I am grateful to the director, Professor Tarun Souradeep, for his assistance with numerous academic matters. I would like to thank Mr. Naresh, the administrative officer in charge, for his assistance with numerous administrative issues. I am grateful to the entire administrative staff for their assistance and support, especially Mrs. K. Radha, Mrs. Marisa, Mrs. Vidya, Mr. Sachin, Mrs. Shailaja, and Mrs. Harini. I would like to thank Mr. Muneeswaran from the department of electrical engineering. I would like to thank everyone at RRI for their cooperation and support, including the canteen and hostel staff.

I appreciate the time that I have spent with each and every RRI student, for the laughter we had, the advice we gave each other, and the stimulating conversations we had on a wide range of issues. I'd like to thank my friends Vishnu, Chandeshwar, Arsalan, Ashish, Palak, Pooja, Sushil, Sukhveer, Saurabh, Sebanti, Sachidananda,

Anindya, Nishant, Sanjay, Sreeja, Anson, Meera, Soumya, Madhu, Dipak, Anand, Swarnak, Abhishek, Pradosh, Bapan, Tanuman, Agnibha, Ranita, Sanchari. I had a wonderful time with the other boarders at Vyalikaval and RMV hostel, where we shared meals, went to the movies, and celebrated festivals like Durga puja, Swarasati puja, Diwali and others. Hostel's cooks, Mangala ji, Soujanya ji, Deepa ji, Uma ji, Sharda ji, Padma ji, Ratnama ji deserve my gratitude for providing us with homely food everyday.

I am always grateful to my teacher Partha Sir. I want to thank Irabati Chakraborty for her continuous support. Finally, I would want to express my sincerest thanks, love, and respect to my parents and my sisters Tuku and Mani for their unwavering support, inspiration, and assistance throughout every up and down of my life.

Synopsis

Correlating microstructural details of an aging colloidal clay suspension with its rheological response is a challenging problem. The many-body interactions in soft systems such as clay suspensions are responsible for their structural and dynamical complexity. It is not fully clear how suspension structures grow with time (age), nor are the effects of such microstructural evolutions on the sample's rheological properties completely understood. We have employed falling ball viscometer and optical tweezers to study interparticle interactions at microscopic lengthscales. Furthermore, the fascinating dynamical properties of dense and jammed systems are not well studied. In this thesis, we have employed simple microscopy techniques to observe the dynamics of dense systems (colloidal and granular) at particle length scales.

Chapter 1 discusses the relevant information required to understand the thesis work. This chapter includes a brief introduction to colloidal systems, and the structure and dynamics of charged clay suspensions and externally vibrated granular systems. The rheological properties of aging Laponite suspensions are discussed in detail. This is followed by a discussion on the dynamics of dense suspensions, with a focus on hydrogel systems.

Chapter 2 explains the experiment techniques and synthesis methods that were used in this thesis. The following experimental setups are discussed – a custom-made falling ball viscometer, a rheometer, an optical tweezer setup, high speed camera used for fast data acquisition, a confocal microscope used in our studies of dense suspensions, an electrodynamics shaker used in the study of the dynamics of vibrated

granular media, and an electron microscope used for studying microstructural details of the colloidal samples used in this thesis. Methods of data analysis employed to understand our experimental data will also be discussed.

Chapter 3 describes the settling dynamics of falling spheres inside a Laponite suspension. Millimetre sized steel balls are used to probe aging Laponite clay suspensions. The motion of the ball is tracked using a high speed camera. The data is analysed to understand the destructuring of aqueous Laponite suspensions due to the passage of the falling ball. A simple toy model is formulated to explain the experimental data.

Chapter 4 describes microrheological studies using optical tweezers (OT). A micron sized bead is used to probe aqueous Laponite suspensions. Oscillatory microrheology is performed using the OT. Elastic and viscous moduli for different aging times and concentrations are measured at several applied oscillatory frequencies. The microrheological results are compared with bulk rheology data. The evolution of structures in Laponite suspensions can be inferred from these experiments. Our conclusions about suspension microstructures are also verified with cryo-SEM imaging. We note that the sizes of the pores of the suspension structures are related to the microrheological measurements of mechanical moduli.

Chapter 5 explains micro rheology experiments with a Laponite suspension in the presence of an electric field. Since Laponite particles are charged in aqueous suspension, the structures of Laponite are sensitive to electric fields. The effect of electric field on the aging of aqueous Laponite suspensions is systematically investigated using the OT. We see that the electric field can be varied to tune the aging property of the sample.

In **Chapter 6**, the dynamics of dense suspensions are explored using confocal microscopy. Understanding the dynamics of dense suspensions is extremely important for different applications. In this work, PNIPAM hydrogel particles are synthesised with different size polydispersities. Mean square displacements are calculated to quantify the average dynamics. The two point self-correlation of positions is

measured, while dynamical heterogeneities in the system are characterised from the variance of the two point correlation functions. The experimental results are compared with simulation results by calculating the number of correlated particles using molecular dynamics simulations considering hard sphere inter-particle interactions.

Chapter 7 reports the study of granular particles vibrated between two plates coupled to an electrodynamic shaker. We use a digital camera to study the particle dynamics by varying the acceleration and frequency of the vibrated platform, the control parameters in our experiment. The effects of these control parameters on the granular dynamics for different shapes and sizes of the granular particles are recorded. Analysis of the observed dynamics includes estimations of the translational and orientational mean square displacements, the auto-correlations of displacements, dynamical heterogeneities and the number fluctuations in the vibrated system.

Chapter 8 summarizes this thesis work and suggests future directions of research.

Prof. Ranjini Bandyopadhyay
(Thesis Supervisor)
Soft Condensed Matter Group
Raman Research Institute
Bangalore 560080 INDIA

Rajkumar Biswas
(Student's name)

List of Publications

1. Rajkumar Biswas, Debasish Saha, and Ranjini Bandyopadhyay. Quantifying the destructuring of a thixotropic colloidal suspension using falling ball viscometry. Physics of Fluids 33.1 (2021): 013103.

2. Rajkumar Biswas, Vaibhav RS Parmar, Anson G Thambi and Ranjini Bandyopadhyay. Correlating microscopic viscoelasticity and structure of an aging colloidal gel using active microrheology and cryogenic scanning electron microscopy. Soft Matter, 2023,19, 2407-2416.

3. Rajkumar Biswas, Anoop Mutneja, Smarajit Karmakar and Ranjini Bandyopadhyay. Influence of particle size polydispersity on dynamical heterogeneities in dense particle packings.(Manuscript under preparation)

Contents

Declaration iii

Acknowledgements v

Synopsis viii

1 Introduction 1

1.1 Colloidal suspension . . . 1

1.2 Colloidal interactions . . . 2

1.2.1 van der Waals Forces . . . 2

1.2.2 Electrostatic repulsion . . . 3

1.2.3 DLVO interaction . . . 4

1.2.4 Lennard-Jones potential . . . 6

1.3 Glass transition . . . 7

1.4 Optical forces on colloids . . . 10

1.5 Rheology . . . 12

1.5.1 Viscoelastic material . . . 13

1.6 Laponite® suspension . . . 14

1.7 Thermoresponsive particles . . . 16

1.8 Dry granular systems . . . 18

1.9 Thesis organisation . . . 18

2 Materials and Methods 28

2.1 Sample preparation 28
2.1.1 Preparation of Laponite suspension 28
2.1.2 Sample cell for microscopy 29
2.1.3 Functionalisation of dye and synthesis of PNIPAM particles . 30
2.2 Instruments and Techniques 31
2.2.1 Rheometer 31
2.2.2 Falling ball viscometer 33
2.2.3 High speed imaging 38
2.2.4 Optical tweezer 38
2.2.5 Cryo-FESEM 41
2.2.6 Confocal microscope 42
2.2.7 Electrodynamic shaker 43

3 Quantifying the destructuring of a thixotropic colloidal suspension using falling ball viscometry 49
3.1 Introduction 49
3.2 Experimental Methods 53
3.3 Results 54
3.3.1 Time dependence of viscosity 54
3.3.2 Falling ball experiments 57
3.3.3 Mathematical model 59
3.4 Conclusions 63

4 Correlating microscopic viscoelasticity and structure of an aging colloidal gel using active microrheology and cryo-FESEM 72
4.1 Introduction 72
4.2 Materials and Methods 76
4.3 Results and Discussion 77
4.4 Conclusions 89

5 AC electric field induced controlled aging of aqueous Laponite suspension 99

5.1 Introduction . . . 99

5.2 Materials and Methods . . . 102

5.3 Results and Discussion . . . 103

5.3.1 Bulk rheology . . . 103

5.3.2 Micro-rheology . . . 105

5.4 Conclusions . . . 109

6 Influence of particle size polydispersity on dynamical heterogeneities in dense particle packings 115

6.1 Materials and methods . . . 119

6.2 Results and Discussion . . . 120

6.2.1 Experimental Results . . . 120

6.2.2 Molecular dynamics simulation . . . 126

6.3 Conclusions . . . 131

7 Dynamical heterogeneities in 2-D granular polydisperse systems 141

7.1 Introduction . . . 141

7.2 Materials and Methods . . . 144

7.3 Results and Discussion . . . 145

7.4 Conclusions . . . 153

8 Summary and future directions 157

List of Figures

1.1 Different systems from a molecule to a living insect are shown based on their length scales. This diagram is inspired by [10]. 2

1.2 (a) Electric double layer is shown for a negatively charged particle surrounded by different counterions. (b) Schematic plot of van der Waals attraction (Eqn.1.1), electrostatic repulsion (Eqn.1.3), DLVO (Eqn.1.4) and Lennard-Jones (Eqn.1.5) interactions in colloidal systems. 5

1.3 The glass transition temperatures T_g are used to scale the data in the Angell plot of viscosity *vs.* inverse temperature. The straight lines in the Angell plot illustrate the Arrhenius dependence of viscosity on temperature for strong glass formers (SiO_2, GeO_2, etc.). For brittle glass formers (toluene, m,o - xylene, etc.), viscosity exhibits non-Arrhenius behaviour. This plot is adapted with permission from [28]. 7

1.4 The volume fraction-dependent phase diagram of monodisperse hard spheres. The solid arrows represent equilibrium states, whereas the dashed arrows represent non-equilibrium states. This diagram is adapted from [2]. 9

1.5 (a) A bead is shown trapped in a medium using a focused laser. (b) The net force acting on a bead is due to a focused laser when the position of a bead is slightly above the focus point. (c) The net force acting on a bead when the bead position (dashed red line) is horizontally away from the trap centre (dashed green line) is shown. p_1, p_2, p_1', p_2' are the momenta carried by light and dp_1 and dp_2 are the changes in the momenta in (b) and (c). 11

1.6 (a) Amplitude sweep measurement, where solid symbols indicate storage modulus G′ and hollow symbols represent viscous modulus G″, for a Laponite suspension having concentration 3.00% w/v at aging time 90 mins. (b) Frequency sweep measurement is shown for a Laponite suspension having concentration 3.00% w/v at aging time 90 mins. The peak in G″ in (a) and the frequency independence of G′ and G″ with G′ > G″ in (b) signify soft glassy rheology. 13

1.7 (a) Empirical formula for Laponite. (b) Figure illustrating the 2:1 crystalline structure of a Laponite platelet. (c) A Laponite platelet. The illustrations are adapted from [57]. 15

1.8 Heat flow measured in DSC after applying a temperature ramp to PNIPAM suspensions. The sudden change in heat flow indicates a transition (LCST) at 32° C. (b) The average hydrodynamic diameter of PNIPAM particles are measured using DLS at different temperatures in dilute suspension. We see that particles deswell rapidly at LCST =32° C. 17

2.1 Schematic diagram of sample cell using glass slide and glass coverslips. 29

2.2 A simple illustration of semi-batch process for synthesising PNIPAM particles. 30

2.3 (a) Photograph of Anton Paar MCR 501 rheometer. (b) Important components of a rheometer shown in this illustration. 32

2.4 The schematic diagrams of parallel plate and double gap geometries are shown along with calculations of important parameters. These figures are adapted from [9]. 33

2.5 (a) Schematic diagram of the experimental setup for ball-drop experiments. (b) A cylindrical tube (length 65 cm and diameter 4 cm) filled with sample is placed inside a water bath at 25°C. (c) The electromagnet used to drop steel balls. (d) High-speed camera—IDT Motion Pro Y4-S2. (e) Trajectory of a falling ball in the viscometer displayed in (b), tracked using a video spot tracker (CISMM), is shown by a yellow line. 34

2.6 (a) Viscosities of three glycerol-water mixtures having different proportions of glycerol and water are measured in a rheometer at 25° C. Time dependents velocities of balls having diameters 3 – 6 mm falling in Newtonian fluids (glycerol water mixtures displayed in (a) having viscosities 0.065, 0.039 and 0.016 Pa.s) are shown in (b), (c) and (d) respectively. The hollow symbols represent the experimental data (error represented using vertical bars) and solid black lines are the fits to $V = V_0 + (V_0 - V_{ter})\exp(t/\tau)$, where V_0, V_{ter} and τ are fitting parameters. (e) The ratio of viscosities measured using the falling ball viscometer and rheometer. The correction factors computed according to the Schiller and Naumann criterion are plotted versus Reynolds number. 35

2.7 Schematic diagram of the optical tweezer set-up. The infrared laser beam is indicated in red. 39

2.8 (a) Distance travelled by the sample stage is measured as a function of the voltage applied to the piezo actuator. The calibration factor, computed from the slope of the curve, is 0.251 μm/V. (b) Position calibration of the QPD is performed by shifting a bead attached to a glass coverslip along the x-axis of the sample cell (shown in Section 2.1.2) by a predetermined distance from the laser's beam centre. The QPD signal is acquired during this movement and plotted against the motion of the trapped bead. We determine the sensitivity of the QPD, 1.51 nm/QPD unit, by fitting the linear region of the curve with a straight line. 40

2.9 (a) Power spectrum of a trapped bead is plotted at two different laser powers and fitted (blue lines) with Lorentzian function. (b) Trap stiffness is plotted as a function of laser power for 1 μm polystyrene bead trapped in water along both x and y axes. 41

2.10 Schematic illustration of a confocal microscope setup is shown. The blue beam is the excitation laser and the green beam is the fluorescent signal coming from the sample. 43

2.11 (a) The schematic illustration of our set-up is shown while recording a video of the granular particles during stage vibration. (b) This configuration is used to calibrate the vibration amplitude and frequency by capturing the movement of the red spot using a high speed camera. 44

2.12 Fourier transform of the vertical stage oscillation, as obtained by tracking a red spot in the side of the shaker. Red dashed line indicates the peak of the signal. The displacement of the red spot due to vertical vibrations of the shaker plate is plotted $vs.$ time in the inset. 45

3.1 The time evolution of viscosity of a Laponite suspension (concentration 2.8% w/v). In the inset, viscosity is plotted with shear rate for 2.8% w/v Laponite suspensions at different aging times (t_w = 1, 2, 3 hrs). While the time-evolution of viscosity in the main figure was acquired for a single sample, the data in the inset was acquired on fresh samples aged to 1 hr, 2 hrs and 3 hrs respectively. 55

3.2 Shear stress is measured by varying shear rate for different aging times of 2.8% w/v Laponite suspensions using a rheometer. Fresh samples were used in each of the 3 experiments. The corresponding viscosity vs. shear rate data is plotted in the inset of Fig.3.1. 55

3.3 Time dependent viscosity of 2.8% w/v Laponite suspensions, of aging times t_w = 1 hr and 3 hr, subjected to constant shear rates of 100 and 180 sec^{-1} at 25°C. 56

3.4 (a) Displacement *vs.* time of the steel balls (diameter = 2, 3, 4, 5, 6 mm) falling through Laponite suspensions of concentration 2.8% w/v at 1 hr aging time (t_w). (b) Velocity *vs.* time is calculated from the displacement data in (a). The error bars are calculated using the protocol specified for balls falling in a medium [30]. 57

3.5 In (a), (b), (c) and (d), velocities of the ball centroids for balls of diameters 2mm , 3mm , 5mm and 6mm respectively, falling through Laponite suspensions of different aging times (t_w), are plotted. Coloured symbols represent experimental data, coloured vertical bars are the corresponding error bars [30] and continuous black lines are the fits to Eqn.3.7. 59

3.6 Destructuring rate, β, *vs.* ball diameter, D, is plotted for different aging times (t_w) of Laponite suspensions. 65

4.1 (a) Isotherm curve (relative heat released, H) for Laponite suspensions having polystyrene particles, when compared with pure Laponite suspension at 25°C temperature for two different particle sizes vs. measurement time. Polystyrene (PS) particles attached to the branches of the Laponite suspension networks (white connected regions) for particles of diameter (b) 1 μm (c) 1.5 μm and (d) 3.34 μm. 77

4.2 Schematic illustration showing the temporal evolution of Laponite microstructure in the presence of a polystyrene probe particle. Top panel: The probe particle attaches to the Laponite microstructure, with the number of contacts depending on particle size. Bottom panel: Individual Laponite particles self-assemble at higher aging times to form network structures through house of cards and overlapping coin assemblies. 79

4.3 Sinusoidal displacement of the sample stage *vs.* time; Bottom: Force experienced by the trapped probe particle. 80

4.4 The blue curve with solid circles indicates the stage position with time. The peaks in the signal are detected using scipy module in Python. The peaks in the stage oscillation signals are indicated using yellow squares. The force on the trapped particle is shown by the red curve with red triangles. The black squares indicate the peaks of the force signal. 81

4.5 G' (solid blue symbols) and G'' (hollow orange symbols) and the corresponding error bars are shown by the shaded regions of the same colour. The maximum possible ranges of the crossover values of the moduli and angular frequencies are marked using the dashed horizontal and vertical lines. 82

4.6 (a) Elastic moduli G' (solid symbols) and viscous moduli G'' (hollow symbols) obtained in microrheological measurements using a probe particle of diameter $D = 1$ μm and plotted $vs.$ angular frequencies of the sample stage for different Laponite suspension concentrations C_L at an aging time $t_w = 90$ min. The vertical dashed lines represent the crossover frequencies where $G' = G''$ for data acquired at different C_L. In the inset, the frequency-dependent complex viscosities $\eta^* = \sqrt{G'^2 + G''^2}/\omega$ are plotted for the same Laponite concentrations. (b) Crossover modulus G_{co} (black) and relaxation time τ (red) of the underlying Laponite suspensions are plotted for different Laponite suspension concentrations C_L. 83

4.7 (a) Elastic and viscous moduli, G′ and G″ respectively, are estimated using oscillatory active microrheology for a 2.75% w/v Laponite suspension at different aging times t_w. (b) Crossover modulus G_{co} (black) and relaxation time τ (red) of the underlying Laponite suspensions are plotted for different Laponite suspension aging times t_w. 84

4.8 (a) G′ and G″ are estimated for a 2.75% w/v Laponite suspension at aging time $t_w = 90$ minutes using oscillatory active microrheology with probe particles of different sizes D. (b) Crossover modulus G_{co} (black) and relaxation time τ (red) of the underlying Laponite suspensions are plotted for different trapped probe particle sizes D. . 85

4.9 Macroscopic or bulk elastic and viscous moduli, G′ and G″ respectively, of a Laponite suspension of concentration $C_L = 3.00\%$ w/v at aging time $t_w = 90$ min measured using a rheometer. 86

4.10 Cryo-FESEM images of Laponite suspensions of different concentrations C_L and aging times t_w **(a)** $C_L = 2.5$ % w/v, $t_w = 90$ mins, **(b)** $C_L = 2.75$ % w/v, $t_w = 90$ mins, **(c)** $C_L = 2.75$ % w/v, $t_w = 150$ mins, **(d)** $C_L = 3.0$ % w/v, $t_w = 90$ mins. 87

4.11 Pore size ratio $\langle D_p \rangle / D$, the ratio of average pore diameter $\langle D_p \rangle$ and the diameter of the trapped particle (D=1 μm), is plotted vs. crossover modulus G_{co} obtained from OT-based active microrheology for different Laponite concentrations C_L at $t_w = 90$ min. In the inset, the pore size ratio is plotted for different sizes of probe particles D = 1 μm, 1.5 μm, 3.34 μm for Laponite suspension concentration C_L = 2.5% and aging time $t_w = 90$ min. 88

5.1 (a) A parallel plate geometry connected to a function generator is shown. The yellow patch is the insulating material used to insulate the rotating motor of a rheometer from the voltage source. The samples are filled between the parallel plates and shown in blue color. (b) The sample cell for electric field experiments used in the optical tweezer setup. The brown colour indicates the copper tape, which is connected to a function generator. 102

5.2 Elastic (G') and viscous (G'') moduli are plotted $vs.$ strain amplitudes after applying different electric fields during 90 mins of aging to Laponite suspensions of concentration $C_L = 3.00\%$ w/v. Measurements are made immediately after the field is switched off. 104

5.3 (a) Complex viscosity $vs.$ strain amplitude is shown for various electric fields applied for 90 mins to Laponite suspensions of $C_L = 3.00\%$ and $t_w = 90$ mins. Complex viscosities in the linear regime, shown by the dashed lines, are used to calculate average complex viscosity values which are shown in (b) and plotted vs. electric field. 105

5.4 Power spectral density is plotted $vs.$ frequency for a Laponite suspension of $C_L = 2.5\%$ w/v at $t_w = 30$ mins subjected to AC electric field of 0.5 V/mm (frequency 1 kHz). The black line is a fit to a Lorentzian function, $\frac{A}{f^2+f_c^2}$. The red vertical dashed line indicates the position of corner frequency obtained from the fit. 106

5.5 (a) Viscosity is plotted with aging time for different electric field strengths for Laponite concentration $C_L = 2.5\%$ w/v. (b) The viscosity of Laponite suspensions at $t_w = 30$ mins aging time *vs.* electric field is plotted. 108

6.1 The hollow symbols denote histogram plots of the diameter distributions of PNIPAM particles obtained from different synthesis batches. The solid curves are fits to Gaussian functions whose widths and heights are used to calculate the size polydispersity indices (PDIs) of the PNIPAM particles. The insets show confocal images of dense suspensions having PDIs (a) 13.62% and (b) 22.20%. 121

6.2 (a) Mean square displacements (MSDs) are plotted *vs.* time for dense PNIPAM suspensions constituted by particles of different PDIs at suspension area fraction $A_p \approx 0.65$. The black dashed line represents diffusive dynamics. In the inset, MSD is plotted for PNIPAM suspensions comprising particles of PDI = 13.62% for different area fractions (the arrow indicates increasing area fraction). (b) Two-point density correlation functions, Q_2 are plotted *vs.* time for suspensions of different particle PDIs at a fixed area fraction ($A_p = 0.65$). Q_2 plots for PNIPAM suspensions of different area fractions (0.52, 0.59, 0.65) for a fixed particle PDI = 13.62% are shown in the inset. 122

6.3 (a) Q_2 is plotted for different probe lengths a in μm (shown in the legend) for suspensions of PNIPAM particles of PDI 13.62%, prepared at an area fraction of 0.65. (b) The corresponding χ_4 *vs.* time is plotted. 124

6.4 (a) χ_4 is plotted *vs.* time for a probe length a^* at which the peak height is maximum for dense PNIPAM suspensions of different size polydispersities (PDIs) and area fractions A_p. (b) χ_4 decreases as temperature increases for PNIPAM suspensions of area fraction = 0.65, constituted by particles of PDI = 20.18%. Simultaneously, we see from the inset that particle MSDs increase with increase in temperature. 126

6.5 (a) Mean square displacements, MSDs, of the simulated particles *vs.* time, shown for different particle PDI values for volume fraction ϕ = 0.6230. (b) Four-point susceptibilities, χ_4, *vs.* time for distinct polydispersity indices (ϕ = 0.6230). In the inset, the corresponding two-point correlation functions, Q_2, are shown. 127

6.6 (a) MSDs extracted from MD simulations are plotted *vs.* time steps for three different temperatures 0.8, 0.9 and 1 at volume fraction 0.6230. (b) MSDs *vs.* time steps for different volume fractions and Q_2 is shown in the inset for T = 0.9. (c) χ_4 is shown for the same temperatures as in (a) and volume fraction 0.6230 and Q_2 is shown in the inset. (d) χ_4 is shown for the same volume fractions as in (b) at T = 0.9. 129

6.7 Number of correlated particles in cooperatively rearranging regions (CRRs), obtained from experiments (black) and simulations (red), are plotted for different particle PDIs for dense suspensions. 130

6.8 A three-dimensional phase diagram depicting jamming to unjamming transitions in dense suspensions for increase in temperature and particle size polydispersity, and for decrease in number density. The jammed region (blue dashed lines) lies around the origin. Arbitrary black solid lines are drawn to visualise the jamming to unjamming transition, achieved by appropriately changing temperature, particle number density or size polydispersity. 131

7.1 (a) Image of electro-dynamic shaker from DESPL(DEV-005). (b) Top view of the top plate: four different spatial regions of the top plate loaded with semolina grains are indicated in black boxes. (c) The area occupied by the grains divided by the total plate area, as analysed from photos using ImageJ, are expressed in terms of normalised intensities. The normalised intensities of the four boxes are plotted with time when the plate is subjected to sinusoidal vibration. 142

7.2 (a) The image of the sample plane is taken using the camera from the top. (b) The corresponding binary image is shown. 145

7.3 (a) Histogram plots of number of particles for two different polydisperse samples are shown. (b) Radial distribution function $g(r)$ *vs.* r is plotted for PDI = 21.81% at area fraction of 0.73. 146

7.4 Mean square displacements (MSDs) are plotted at different area fractions for two different particle PDIs. The blue dashed line (slope = 1) represents diffusive nature of particle dynamics. 148

7.5 χ_4 *vs.* time is shown for (a) PDI = 21.81% and (b) PDI = 36.36% for different area fractions. The corresponding Q_2 are shown in the insets. 149

7.6 Number of correlated particles is plotted *vs.* area fraction for different PDIs. In the inset, the peak values of χ_4, χ_4^*, are shown. 152

List of Tables

2.1 Viscous drag and wall effect corrections for Newtonian glycerol-water mixtures, fluids computed according to the protocols specified in this section. 37

3.1 Parameters measured by fitting Eqn.3.7 to the data in Fig.3.5. 64

5.1 Corner frequencies obtained for OT based microrheology experiments for different aging times and electric fields are shown for Laponite suspensions of $C_L = 2.5\%$ w/v and for different ages t_w. 107

6.1 The flow rate of the solution of reaction ingredients during synthesis of PNIPAM particles to achieve various size distributions (PDIs). . . 120

6.2 The optimal probe lengths, a^*, used for analyses of both experiments and simulations, are tabulated for suspensions of different PDIs and packing fractions. 123

6.3 Parameters extracted from fits of stretched exponential functions to Q_2, shown as black lines in Fig.6.2(b) and in the inset of Fig.6.5(b). Along with the fitted parameters, we have also tabulated the peak values of χ_4, plotted in Figs.6.4(a) and 6.5(b), for experiments and simulations. 125

7.1 Probe length where χ_4 peak is maximum, Q_2 value at the time where peak in χ_4 appears, peak value of χ_4 and number of correlated particles (N_{corr}) are tabulated for two PDIs at different area fractions. . 151

Chapter 1

Introduction

1.1 Colloidal suspension

A colloidal suspension is a heterogeneous system having two components, a dispersed phase and a dispersion medium. Such systems can be composed of liquid or solid particles dispersed in a continuous liquid, gas or solid medium as well as gaseous particles dispersed in liquid or solid medium [1–5]. The particles in the dispersed phase have diameter lying between 10 nm to 1 μm and their motion is influenced by thermal forces [6]. The range of colloidal sizes is set by a balance between the gravitational and diffusive fluxes of colloidal particles in suspension [6, 7]. A colloidal particle can, therefore, be more than a hundred times larger compared to an atom. A solution is a homogeneous mixture of solutes (atoms or molecules) dissolved in a solvent. Unlike in a solution, particles in a colloidal suspension are large enough to scatter or reflect light [8]. The scattering of blueish light from colloidal suspensions is known as Tyndall effect [9] and this effect can be used to distinguish between a solution and a colloidal suspension. The size ranges of colloids when compared to other systems are shown from the molecular lengthscale to the length of a living insect in Fig.1.1. Colloidal systems can be classified into different categories such as aerosol (solid or liquid particles dispersed in gaseous medium), emulsion (liquid particles in liquid medium), suspension (solid particles in liquid medium), etc. Fog is

an example of aerosol which consists of dispersed liquid particles in a gaseous phase. Smoke is also an aerosol composed of solid particles dispersed in air. Emulsions are a unique type of colloidal suspension in which two immiscible liquids coexist. Milk, paint, and mayonnaise are some common examples of emulsions.

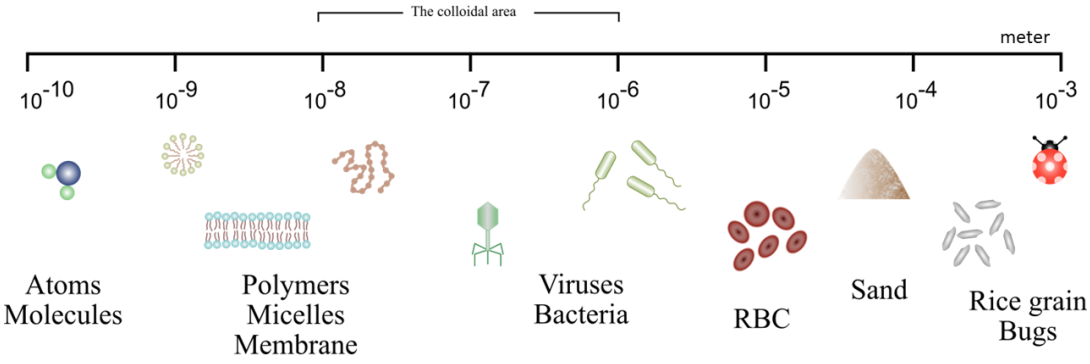

Figure 1.1: Different systems from a molecule to a living insect are shown based on their length scales. This diagram is inspired by [10].

1.2 Colloidal interactions

Colloidal particles in aqueous suspensions have been used in various experiments in this thesis. The interactions among these particles play an important role in the emergent suspension properties. Suspension rheological characteristics, local particle dynamics and the impact of external perturbations are intricately linked to the interactions between particles. The subsequent subsections delve into distinct categories of interactions, establishing connections with the work presented in this thesis.

1.2.1 van der Waals Forces

van der Waals forces are attractive in nature and act between all atoms and molecules. The van der Waals attraction originates from three distinct sources: dispersion (London), induction (Debye), and orientation (Keesom) interactions [11]. The dispersion

energy can be understood as a correlation of electron motions in neighbouring non-overlapping molecular systems. The induction energy arises from the polarization of one molecule by the permanent dipole moments of neighbouring molecules, while the orientation energy results from a correlation of the motions of rotating permanent dipole moments of neighbouring molecules. These short-range forces depend on the distance between the atoms or molecules. In the case of two atoms or molecules having permanent dipole moments, an attractive force exists between them arising from dipole-dipole interactions [12]. In neutral atoms or molecules, short-lived dipoles are formed due to the fast-moving electrons around the nucleus. London dispersion interaction appears between these dipoles when they begin to pair with each other to reduce the interaction energy [13, 14]. As colloidal particles are composed of several molecules, pairwise London interactions are added to get the total van der Waals interaction between two non-polar particles. van der Waals interaction energy between two parallel plates having separation of l is given as [15],

$$V_{VD}(r) = -\frac{H}{12l^2} \tag{1.1}$$

where, H is the Hamaker constant with typical order of $\approx 10^{-20} J$.

1.2.2 Electrostatic repulsion

If colloidal particles having surface charges are added to an electrolyte solution, the counterions from the solution get attracted towards the surface of the colloidal particles for achieving neutrality. These counterions form a fixed layer around the particle, known as the Stern layer [14, 16]. However, these counterions cannot neutralise the surface charges completely. To achieve neutrality, a second layer of charges accumulates around the colloidal particle. Due to thermal motion, the counterions of this layer tend to diffuse around the particle. The surface charges of the colloidal particle along with the Stern and diffuse layers form the electric double layer, shown in Fig.1.2(a).

When two colloidal particles come close to each other and overlap, the electric double layers of each of these particles distort which leads to electrostatic repulsion. This phenomenon is known as electric double-layer repulsion. The range over which this repulsion is experienced is known as Debye screening length $(1/\kappa)$ [15]. The expression for this length scale is given below,

$$\frac{1}{\kappa} = \left(\frac{\epsilon_0 \epsilon_r k_B T}{\sum_i (z_i e)^2 n_i} \right)^{0.5} \tag{1.2}$$

where, ϵ_r is the relative permittivity of the medium, ϵ_0 is the permittivity of free space, k_B is the Boltzmann constant, T is the temperature of the suspension, z_i is the valency of the i-th species of counterions of concentration n_i and e is the charge of an electron.

The counterions in the Stern layer remain closely attached to the colloidal particle, whereas the diffuse layer is comparatively more mobile. A layer of the adjacent fluid adheres to a colloidal particle as it moves in the dispersion medium. The boundary of this layer is known as the slipping plane. The potential at this slipping plane is called the zeta potential [17]. When two charged plates are separated by a distance $2d$, the energy per unit area of their double layer interaction (V_{EDL}) can be calculated by considering a slight overlap in the two layers [14],

$$V_{EDL}(d) = \left(\frac{64 n^o k_B T \alpha^2}{\kappa} \right) exp(-2\kappa d) \tag{1.3}$$

where n^o is the ionic concentration of the counterions and $\alpha = \tanh(ze\phi/4k_BT)$, z is the valency of the counterions and $\phi = \psi_s - \psi_0$, where ψ_s is the surface electric potential of the particle, ψ_0 is the constant potential in the bulk solution.

1.2.3 DLVO interaction

Derjaguin and Landau proposed a theory for the stability of colloidal suspensions in 1941 [18], which suggested strong but short-range van der Waals attractions, which were balanced by the stabilising influence of electrostatic repulsions. Verwey

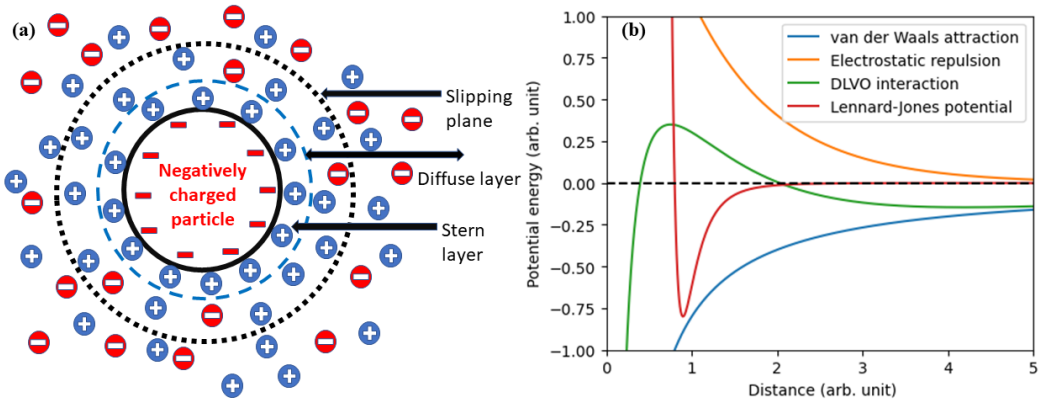

Figure 1.2: (a) Electric double layer is shown for a negatively charged particle surrounded by different counterions. (b) Schematic plot of van der Waals attraction (Eqn.1.1), electrostatic repulsion (Eqn.1.3), DLVO (Eqn.1.4) and Lennard-Jones (Eqn.1.5) interactions in colloidal systems.

and Overbeek independently arrived at the same conclusion seven years later [19]. The attractive potential energy from van der Waals interaction and the repulsive potential energy from electrical double layers at the surface of the colloidal particle contribute to the overall potential energy of a colloidal system. This is known as the DLVO theory and is given by,

$$V_{DLVO} = V_{VD} + V_{EDL} \tag{1.4}$$

Here, V_{VD} denotes the van der Waals attraction from Eqn.1.1, which results from the pair interactions between all atoms or molecules in colloidal particles. The repulsive electrostatic interaction between two screened colloidal particles is denoted by V_{EDL} (Eqn.1.3). Fig.1.2(b) depicts a schematic plot of V_{VD}, V_{EDL}, and V_{DLVO} as a function of the separation between two colloids. At a critical distance between colloidal particles, the DLVO potential reaches its peak. If the height of the energy barrier in the DLVO theory is greater than thermal energy (k_BT), flocculation

between two colloidal particles can be prevented. The addition of salt (contains co-ions and counterions) decreases the repulsion between colloidal particles and, consequently, the height of the DLVO peak. At a particular threshold concentration of salt, colloidal particle surfaces are completely screened and the peak in DLVO interaction disappears. The further addition of counterions results in the irreversible aggregation or flocculation of colloidal particles.

1.2.4 Lennard-Jones potential

When two atoms or molecules come close to each other, there exist attractive and repulsive forces between them. The attractive force arises due to the dipole-dipole interaction. The repulsive force arises from the repulsion of electron clouds of the two molecules when they come too close to each other. This repulsive force is a direct consequence of Pauli's exclusion principle, which forbids two or more electrons to share a single state. The mathematical form of the Lennard Jones potential is given below [20–22],

$$V_{LJ}(r) = 4\epsilon \left[\left(\frac{\sigma}{r}\right)^{12} - \left(\frac{\sigma}{r}\right)^{6} \right] \tag{1.5}$$

Here, r is the distance between two particles. ϵ is the depth of the potential and σ is the distance at which the potential between two particles is zero. The inverse sixth power term is the attractive part of the potential which describes the long-range dipole-dipole interaction. The inverse twelfth power term is primarily introduced as a square of the attractive term for mathematical simplicity. This term can model the short-range Pauli repulsion efficiently. The Lennard Jones potential is the simplest model to approximate the van der Waals attraction and repulsion due to overlapping shown in Fig.1.2(b).

1.3 Glass transition

Colloidal and molecular glasses both comprise densely packed constituents that are kinetically constrained. This results in ubiquitous glassy features such as aging and slow dynamics. The much larger sizes of colloidal particles when compared to their molecular counterparts make suspensions of the former a useful model system [23]. Near the glass transition point, the viscosity of glass forming systems becomes incredibly high, and their dynamics freeze. Structure-wise, however, these systems stay in liquid form below the glass transition point [24]. Glassy systems are characterised by metastable states that are out of equilibrium and exhibit aging behaviour [25, 26]. Both colloidal and molecular glasses exhibit dynamical heterogeneity around the glass transition point with the length scale associated with this heterogeneity growing as the glass transition is approached [27].

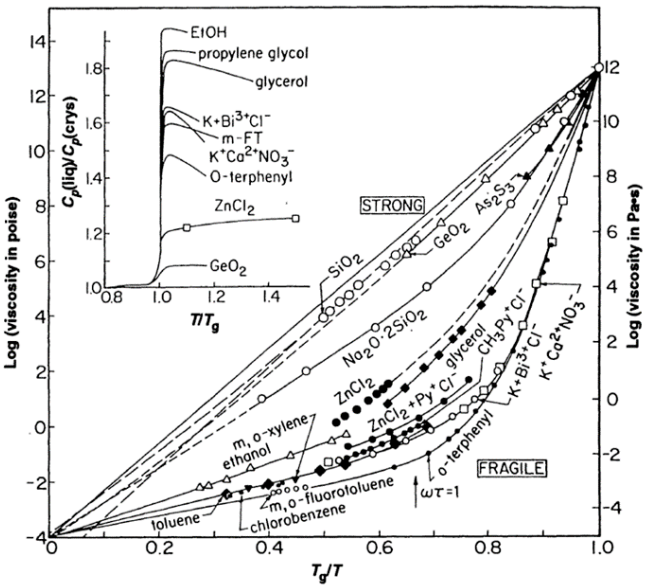

Figure 1.3: The glass transition temperatures T_g are used to scale the data in the Angell plot of viscosity *vs.* inverse temperature. The straight lines in the Angell plot illustrate the Arrhenius dependence of viscosity on temperature for strong glass formers (SiO_2, GeO_2, etc.). For brittle glass formers (toluene, m,o - xylene, etc.), viscosity exhibits non-Arrhenius behaviour. This plot is adapted with permission from [28].

Molecular glass formers (SiO_2, GeO_2, m,o - xylene, etc.) can be quenched rapidly by decreasing the temperature to form glasses. A supercooled state in a liquid can be achieved by cooling the material below its freezing point rapidly enough to prevent crystallisation. Supercooled liquids and associated glass transitions exhibit a number of fascinating characteristics like non-exponential relaxation process including a sharp increase in viscosity and heat capacity at glass transition temperature T_g [29, 30]. Crystalline order can be prevented if the liquid is cooled below its melting point T_m at a rate larger than the crystal nucleation rate. The molecules' structural relaxation or α-relaxation timescale becomes larger than the laboratory timescale below the glass transition temperature T_g [31]. In the available literature, the temperature where structural relaxation becomes 100 seconds is known as the glass transition point T_g [31]. Similarly, viscosity also increases with decrease in temperature as discussed earlier for relaxation time scales. It has a value of around 10^{12} Pa.s at the transition point.

For some materials where the activation energy is independent of temperature, viscosity increases according to the Arrhenius relation as shown in Fig.1.3. In some other glass formers, the temperature dependent viscosity deviates from the Arrhenius form, and this deviation defines the fragility of the material. In these materials, the α-relaxation timescale τ_α and viscosity η follow the Vogel-Fulcher-Tammann (VFT) equation shown below [32, 33],

$$\eta = \eta_0 \exp\left[\frac{DT_0}{T - T_0}\right] \tag{1.6}$$

$$\tau_\alpha = \tau_0 \exp\left[\frac{DT_0}{T - T_0}\right] \tag{1.7}$$

D is the material dependent fragility index. Here T_0 is called the Vogel temperature at which η diverges [31]. Strong glass formers have a large value of D. For fragile glasses, viscosity and relaxation time changes rapidly near T_0.

Colloidal suspensions are mixtures of tiny (10 nm - 1 μm radius) solid particles in a suspending liquid [2]. Their glass transition is determined by particle con-

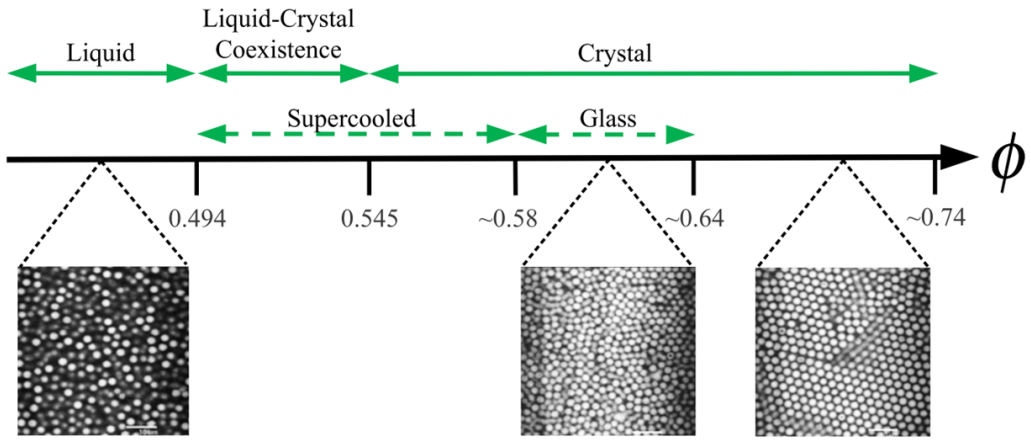

Figure 1.4: The volume fraction-dependent phase diagram of monodisperse hard spheres. The solid arrows represent equilibrium states, whereas the dashed arrows represent non-equilibrium states. This diagram is adapted from [2].

centration rather than temperature. Particles exhibit Brownian motion and readily diffuse across the sample at low concentrations. With increasing concentrations, the particles randomly pack together, and the sample viscosity increases considerably as a function of concentration. Brownian motion allows the sample to equilibrate below the glass transition concentration, yet the sample is structurally still a liquid. Equilibration on experimental time scales is no longer possible above the glass transition concentration, and the sample develops yield stress like a conventional elastic material. A phase diagram is shown for hard monodisperse (size polydispersity <5%) spheres as a function of volume fraction in Fig.1.4. The liquid like nature of the suspension remains up to a volume fraction ϕ of 0.494. By further increasing the volume fraction, the suspension enters into a supercooled region which persists between ϕ = 0.494 - 0.58. The glassy state is observed between 0.58 to 0.64, which corresponds to the random loose and close packing fractions for monodisperse spherical particles [2, 34]. In the supercooled regime, below the glass transition point, particle dynamics exhibit heterogeneity. This heterogeneity is significantly influ-

enced by size polydispersity of the particles, which is very common in nature. A subsequent chapter in this thesis investigates the effect of size polydispersity on the dynamics of supercooled particles.

1.4 Optical forces on colloids

Kepler hypothesised radiation pressure by observing the deflection of a comet's tail due to the effect of sunlight. Later, a similar theory was also proposed by Maxwell in his theory of electromagnetism [35]. Light consists of fundamental particles called photons. A photon carries momentum depending on the wavelength of light, and the momentum is determined using the formula [36],

$$p = \frac{h}{\lambda} \tag{1.8}$$

where p is the linear momentum of each photon pointing in the direction of light propagation, λ is the wavelength and h is the Planck's constant, $h = 6.626 \times 10^{-34} Js$.

In the 1970s, Arthur Ashkin used a laser to manipulate a micron-sized bead by using the force exerted by a laser [37, 38]. The technique involves focusing a laser light very tightly to a diffraction limited spot by using an objective lens having a high numerical aperture. Generally, a Gaussian laser beam is used for optical trapping. A dielectric bead with a refractive index higher than that of the medium experiences a force towards the laser's high intensity region, which is the focus point [39]. There are two kinds of forces which act on the dielectric bead, namely, the scattering force and the gradient force. Scattering force acts on the particle in the direction of the laser. The force acting due to a change in the intensity of the laser is known as gradient force and acts towards the direction of highest laser intensity. In Fig.1.5(a), a bead in a sample cell is trapped in the medium using light. For a stable trapping process, the gradient force pulling the particle towards the focus must be higher than the scattering force which pushes the particle away from the focus point. To satisfy this, an objective lens with high numerical aperture is required. To explain the gradient

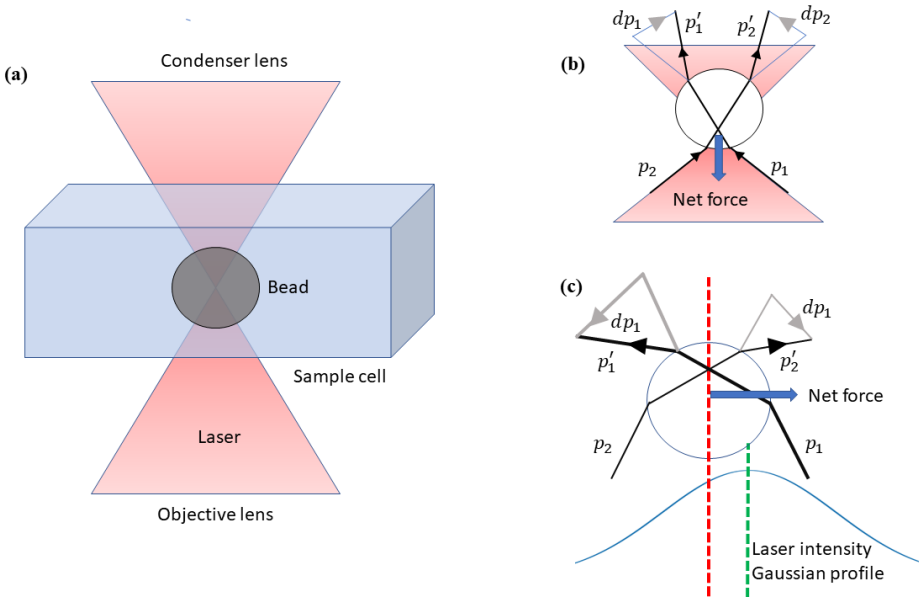

Figure 1.5: (a) A bead is shown trapped in a medium using a focused laser. (b) The net force acting on a bead is due to a focused laser when the position of a bead is slightly above the focus point. (c) The net force acting on a bead when the bead position (dashed red line) is horizontally away from the trap centre (dashed green line) is shown. p_1, p_2, p_1', p_2' are the momenta carried by light and dp_1 and dp_2 are the changes in the momenta in (b) and (c).

force we considered two situations where the particle is above the trap in Fig.1.5(b) and away from the focus point (maximum intensity) in Fig.1.5(c). The momentum of photons are denoted by p. The net force shown in these figures is always towards the centre of the trap. If the displacement of the trapped bead is small, the gradient force experienced by the particle is proportional to the displacement from the trap centre. The proportionality constant is known as the spring constant and the force is Hookean or spring like in nature. The particle confined within the optical trap serves as a valuable tool for measuring the local mechanical properties of the sample.

Depending on the size (D) of the trapped bead compared to the wavelength (λ) of the laser, the theory of optical trapping can have two different regimes: Rayleigh and Mie [40]. In the Rayleigh regime ($D << \lambda$), the particle size is significantly less than the wavelength of the laser. In this regime, the particles are considered point dipoles. The Mie theory ($D \approx \lambda$) is for a particle of size similar to the wavelength of light. In this regime, general ray optics can be applied to calculate the change in

momentum transfer which is related to gradient and scattering forces.

1.5 Rheology

Rheology is the study of the viscous (flow) and elastic (deformation) responses of matter. The complex shear modulus of a generic material can be used to express its linear viscoelastic (LVE) properties [41], $G^*(\omega) = G'(\omega) + iG''(\omega)$, ω is the angular frequency. G^* is a complex number whose real and imaginary parts provide information regarding the elasticity and viscosity of the investigated material. Typically, these are denoted as the storage (G') and loss (G'') moduli, respectively. The usual method for determining the LVE characteristics of a material involves the application of an oscillating shear strain, $\gamma(\omega, t) = \gamma_0 \exp(i\omega t)$ and the measurement of the resultant oscillatory shear stress, which can be written as [6],

$$\sigma(\omega, t) = \sigma_0 e^{i(\omega t + \phi(\omega))} \tag{1.9}$$

where ϕ is the phase difference, σ_0 and γ_0 are respectively the stress and strain amplitudes. The relationship between complex shear modulus and the two experimental functions defining stress (σ) and strain (γ) are as follows,

$$G^*(\omega) = \sigma/\gamma \tag{1.10}$$

$$G^*(\omega) = \frac{\sigma_0}{\gamma_0}\cos(\phi(\omega)) + i\frac{\sigma_0}{\gamma_0}\sin(\phi(\omega)) \tag{1.11}$$

Equation 1.11 denotes the real and imaginary parts of the complex shear modulus (G^*), where the elastic modulus, $\mathrm{G}' = \frac{\sigma_0}{\gamma_0}\cos(\phi(\omega))$ and viscous modulus, $\mathrm{G}'' = \frac{\sigma_0}{\gamma_0}\sin(\phi(\omega))$. In order to obtain a complete picture of the structure and dynamics of a material, it is crucial to have an understanding of the viscoelastic properties over a wide range of frequencies. The frequency dependent behaviour of bulk viscoelastic moduli has been correlated to the material's molecular interaction and topological

structure at different lengthscales [42].

Microrheology refers to the study of rheology at microscopic lengthscales [43]. Typically, passive and active microrheology are used to investigate the rheological properties of a medium [44–47]. For these methods, a micron-sized bead is utilised as a tracer particle to investigate the properties of the medium. Thermal energy (k_BT) is responsible for the motion of the tracer particle in passive microrheology. Trajectories of the tracer particle are measured optically using either microscopy or light scattering techniques. By measuring the mean-square displacement of the tracer particle, the viscoelastic moduli of the medium can be determined from the generalised Stokes-Einstein relation [48]. In active microrheology, the tracer particle experiences an external force which can be generated using a magnetic or electric field, light or a chemical reaction [49].

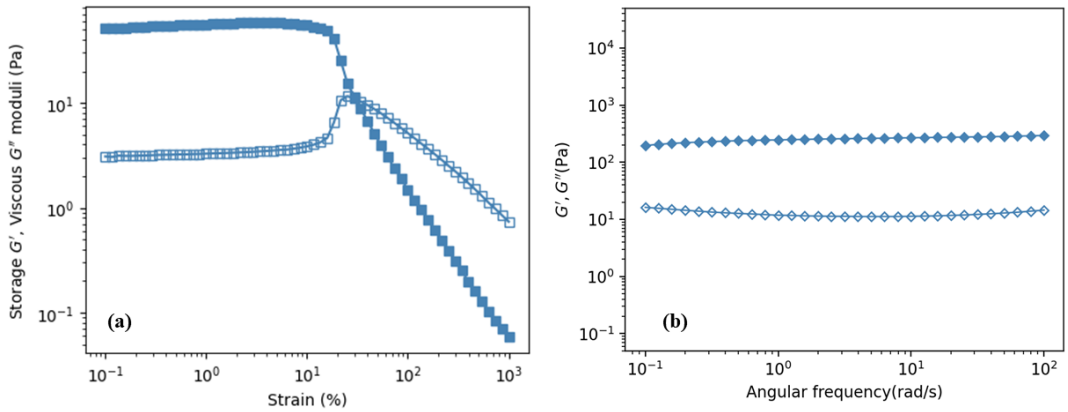

Figure 1.6: (a) Amplitude sweep measurement, where solid symbols indicate storage modulus G′ and hollow symbols represent viscous modulus G″, for a Laponite suspension having concentration 3.00% w/v at aging time 90 mins. (b) Frequency sweep measurement is shown for a Laponite suspension having concentration 3.00% w/v at aging time 90 mins. The peak in G″ in (a) and the frequency independence of G′ and G″ with G′ > G″ in (b) signify soft glassy rheology.

1.5.1 Viscoelastic material

Viscoelasticity is a material property wherein the material simultaneously displays viscous and elastic responses when subjected to deformation [41]. Generally, the

relation between stress and strain is studied to understand the mechanical characteristics of different materials. In the case of a viscoelastic material, the relationship between stress and strain is a function of time. The deformation rate also affects their mechanical properties, which means the stress-strain behaviour of a viscoelastic material changes at different strain rates. Representative data for oscillatory measurements using a rheometer is shown in Fig.1.6. During an amplitude or strain sweep, the frequency of the perturbation is fixed to a constant value while the deformation increases. For a frequency sweep measurement, the deformation (strain) remains constant as the frequency increases. Creep and stress relaxation are the key features exhibited by viscoelastic materials [41]. Under constant stress, a viscoelastic material deforms slowly and gradually; this characteristic is known as creep. The gradual reduction of stress when a viscoelastic material is kept under constant strain is defined as stress relaxation. All complex viscoelastic materials can be modelled as a combination of an ideal spring (perfectly elastic element) and a dashpot (completely dissipative element). Two of the most fundamental models of viscoelasticity are Maxwell and Kelvin models [41, 50, 51]. The Maxwell model comprises a spring and a dashpot in series while a Kelvin model connects the two elements is parallel.

1.6 Laponite® suspension

Laponite® is a synthetic sodium lithium magnesium silicate clay having a structure similar to that seen in hectorite clay minerals [52]. Laponite particles are disk-shaped with a diameter of 25-30 nm and a thickness of approximately 1 nm [53] as shown in Fig.1.7. Two varieties of Laponite clay are typically available: Laponite XLG and Laponite RD, with the former containing less heavy metals. Laponite XLG is used for the experiments presented in this thesis. A single Laponite particle consists of an octahedral magnesia layer sandwiched between two tetrahedral silica layers. Laponite particles form one dimensional stacks called tactoids in dry powder form by sharing sodium atoms in the interparticle gallery. When Laponite powder is added

to water, water molecules enter the inter gallery area of the tactoids, and sodium ions dissociate in water. The majority of the particle's periphery is composed of MgOH groups, which undergo protonation depending on the pH of the solvent [54]. The rims acquire a positive charge in deionised Milli-Q water, and the particle's surface acquires a negative charge due to the detachment of sodium ions [55]. The electrical double layer surrounding each Laponite particle exhibits a gradual and continuous evolution over timescales up to a few hours due to the exfoliation of Laponite platelets from the tactoids and the simultaneous leaching of Na^+ ions from the particle faces. An increase in the number of counterions participating in the electric double layer reduces the electrostatic repulsive forces between particles. The positive edge of a Laponite particle interacts with the negatively charged face of another Laponite particle to initiate the formation of suspension microstructures via overlapping coins (OC) and house of cards (HoC) arrangements [56]. As time passes, Laponite particles self-assemble to form system-wide fragile microstructures as a result of a physical aging process. The phase diagram of Laponite suspensions depends on its concentration and salt content. Ruzicka and Zaccarelli [57] summarised the

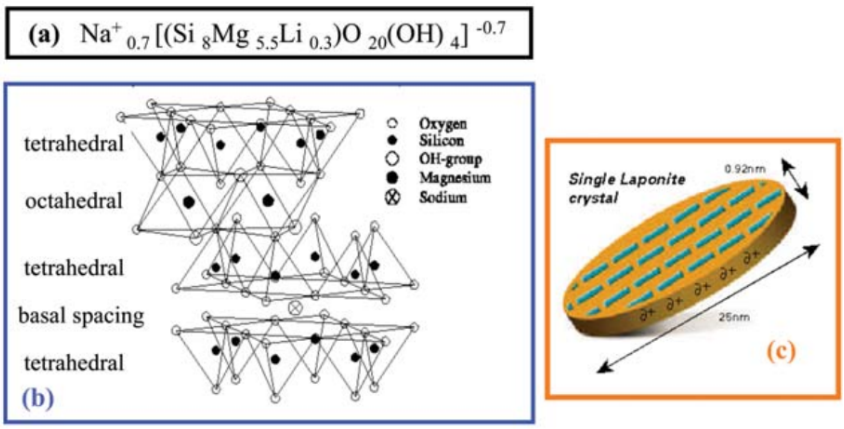

Figure 1.7: (a) Empirical formula for Laponite. (b) Figure illustrating the 2:1 crystalline structure of a Laponite platelet. (c) A Laponite platelet. The illustrations are adapted from [57].

phase diagram observed by several groups during the past two decades. The interparticle interaction can be both attractive and repulsive due to the asymmetric

charge distributions on the surfaces of the Laponite particles. Face-to-edge contacts between Laponite particles in suspension for a particular added salt concentration range give rise to complex microstructures over time. Aging is defined as the spontaneous evolution of material properties in metastable Laponite suspensions, which occurs due to the evolution of electrostatic interactions in the suspension [58]. In general, for Laponite concentrations of more than 2%, the viscosity and elasticity of the suspension increase as a function of time and concentration [59]. This increase in relaxation time scales due to an increase in viscosity, observed via dynamical light scattering, demonstrates that Laponite suspensions undergo a physical aging process [60]. In soft matter physics, the formation of Laponite microstructures and the study of their rheological properties has been a fascinating topic, and Laponite suspensions have been often used to model the glass transition dynamics of kinetically constrained systems such as molecular glasses [61–63]. Subsequent chapters delve into the examination of both microstructural evolution and mechanical changes of the samples resulting from the aging process.

1.7 Thermoresponsive particles

Thermoresponsive poly(N-isopropylacrylamide) or PNIPAM microgel particles are studied in this thesis and are composed of PNIPAM polymer chains that are crosslinked [64]. Swollen PNIPAM microgel particles in an aqueous medium below the lower consulate solution temperature (LCST) are composed of around 2% to 3% crosslinked polymer chains, while the rest is water [65]. PNIPAM particles in such an aqueous medium remain in a swollen state, such that the water inside the PNIPAM particles can be in two different configurations. Due to hydrogen bonding interactions between water molecules and amide groups of PNIPAM, the water molecules associated with polymer chains are immobilised [66]. However, the water molecules that are not associated with polymer chains remain free. By increasing temperature beyond the LCST, PNIPAM particles go from a swollen to a collapsed state. This reversible

transition occurs due to switching of particles interaction between hydrophilic (at low temperature) to hydrophobic (at high temperature) and can be observed as a function of temperature. The diameters of the swollen PNIPAM particle decrease very sharply near 32° C. This transition temperature is the lower consolute solution

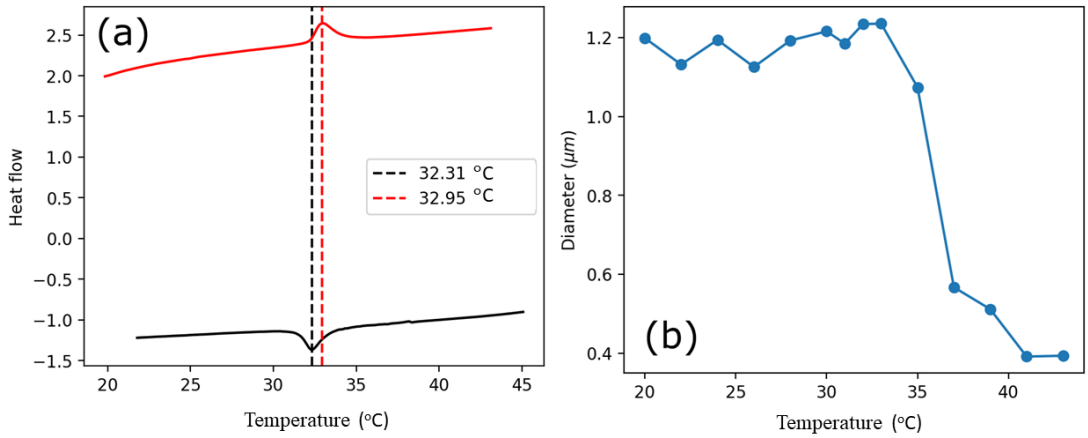

Figure 1.8: Heat flow measured in DSC after applying a temperature ramp to PNIPAM suspensions. The sudden change in heat flow indicates a transition (LCST) at 32° C. (b) The average hydrodynamic diameter of PNIPAM particles are measured using DLS at different temperatures in dilute suspension. We see that particles deswell rapidly at LCST =32° C.

temperature (LCST) that was briefly mentioned before. The enthalpy of hydrogen bond formation between a water molecule and the amide groups of PNIPAM polymer chains determines the LCST of PNIPAM particles. As the temperature rises, these hydrogen bonds begin to break down and water molecules are released from the polymer chains, causing microgels to collapse or deswell. This thermoresponsive nature is studied using differential scanning calorimetry (DSC) and dynamic light scattering (DLS) techniques [67, 68]. In differential scanning calorimetry, the heat change is measured, which is associated with the enthalpy of the medium. The hydrodynamic radius of PNIPAM particles is calculated for a dilute suspension at different temperatures using dynamic light scattering. The experimental results from DSC and DLS measurements are shown in Figs.1.8(a) and (b) respectively.

1.8 Dry granular systems

Granular systems are ubiquitous in our daily lives [69]. They are observed almost everywhere. Examples of dry granular systems include nuts, coal, sand, cereals, rice, ball bearings, medicinal powders, etc. Due to their macroscopic sizes, these systems are athermal [70]. The minimum particle size for granular systems is generally around 10 microns [71]. Granular materials are not affected by Brownian motion. They exhibit jamming [72–74], which is a transition from a fluid-like to a disordered solid-like state that occurs out of thermal equilibrium as a result of compression or shear. The absence of cohesion in dry granular materials means granular solids only exist in the presence of externally imposed stresses, such as gravity, compression, or shear. So the interaction between these dry particles is almost cohesionless and they only interact via repulsive contact forces [75]. Thermodynamically, granular systems are far from equilibrium [76]. Jammed granular systems are generally trapped in a local energy well, but it is possible to find a lower energy minimum by perturbing the system. The metastable state of granular packings is similar to glassy materials observed in molecular glasses and dense colloidal or polymeric suspensions.

1.9 Thesis organisation

Chapter 1 offers a brief overview of colloidal systems and their interparticle interactions. In addition, it addresses the fundamentals of rheology, optical forces on colloids and the phases that emerge in soft matter systems. The samples, i.e. suspensions constituted by Laponite clay, thermoresponsive particles and non-Brownian grains (mm-sized Teflon balls in our case), are briefly discussed in this chapter. Protocols for sample preparations and the instruments used are described in Chapter 2. Experiments in Chapter 3 demonstrate the absence of terminal velocity for balls falling through aging Laponite clay suspensions. A simple model is proposed to comprehend the motion of the falling ball within this complex fluid. Chapter

4 correlates the microstructure of a Laponite suspension with its microrheological features. Active microrheology based on optical tweezers is employed to investigate the viscoelastic properties, and cryo-FESEM is used to image the microstructures constituted by self-assembling Laponite particles. Using an AC electric field, the evolution of these microstructures formed by Laponite particles in aqueous suspension can be controlled. In chapter 5, such controlled aging in the presence of AC fields is measured using both a rheometer and an optical tweezer. The effect of size polydispersity on the dynamics of dense PNIPAM particles is next studied. The heterogeneous nature of the suspension dynamics is reported and compared to our molecular dynamics simulation results in Chapter 6. A shaker is used to agitate a dry granular system comprising size polydisperse Teflon balls in Chapter 7. The growth of dynamical heterogeneity is investigated with increasing area fractions. The eighth chapter summarises the findings reported in this thesis and proposes future research directions.

Bibliography

[1] R. J. Hunter. Foundations of colloid science. *Oxford University Press.*, 2001.

[2] Gary L Hunter and Eric R Weeks. The physics of the colloidal glass transition. *Reports on Progress in Physics*, 75(6):066501, 2012.

[3] J M Coulson, J F Richardson, J H Harker, and J R Backhurst. *Coulson and Richardson's Chemical Engineering*. Pergamon Press, 2002.

[4] David Julian McClements and Eric Dickinson. *Advances in Food Colloids*. Springer, 1996.

[5] O. V. Kruglova, Pieter-Jan Demeyer, Kuo Zhong, Yuxue Zhou, and Koen Clays. Wonders of colloidal assembly. *Soft Matter*, 9:9072–9087, 2013.

[6] Jan Mewis and Norman J Wagner. *Colloidal Suspension Rheology*. Cambridge university press, 2012.

[7] Wilson C K Poon. Colloidal suspensions. In *The Oxford Handbook of Soft Condensed Matter, edited by EM Terentjev & DA Weitz*. Oxford University Press, 2015.

[8] K Krishnamurtt. The scattering of light in colloidal solutions and gels. *Nature*, 124(3131):690–691, 1929.

[9] Dan B Rootman, Joseph L Lin, and Robert Goldberg. Does the tyndall effect describe the blue hue periodically observed in subdermal hyaluronic acid gel placement? *Ophthalmic Plastic & Reconstructive Surgery*, 30(6):524–527, 2014.

[10] C Bernardini, SD Stoyanov, LN Arnaudov, and MA Cohen Stuart. Colloids in flatland: a perspective on 2d phase-separated systems, characterisation methods, and lineactant design. *Chemical Society Reviews*, 42(5):2100–2129, 2013.

[11] H. Margenau. Van der waals forces. *Reviews of Modern Physics*, 11(1):1, 1939.

[12] Jacob N Israelachvili. The nature of van der waals forces. *Contemporary Physics*, 15(2):159–178, 1974.

[13] Hugo C Hamaker. The london—van der waals attraction between spherical particles. *Physica*, 4(10):1058–1072, 1937.

[14] Hendrick Van Olphen. *An Introduction to Clay Colloid Chemistry: For Clay Technologists, Geologists and Soil Scientists*. Wiley, 1977.

[15] Jacob N. Israelachvili. Intermolecular and surface forces. Elsevier, 1985.

[16] GH Bolt. The ionic distribution in the diffuse double layer. In *Developments in Soil Science*, volume 5, pages 1–26. Elsevier, 1979.

[17] Terence Cosgrove. *Colloid science: principles, methods and applications*. John Wiley & Sons, 2010.

[18] Boris V. Derjaguin and Lev Shchur Landau. Theory of the stability of strongly charged lyophobic sols and of the adhesion of strongly charged particles in solutions of electrolytes. *Progress in Surface Science*, 43:30–59, 1941.

[19] Charles Edward Marshall. Theory of the stability of lyophobic colloids. the interaction of particles having an electric double layer. *Journal of Polymer Science*, 4:413–414, 1949.

[20] John Edward Jones. On the determination of molecular fields.—ii. from the equation of state of a gas. *Proceedings of the Royal Society of London. Series A, Containing Papers of a Mathematical and Physical Character*, 106(738):463–477, 1924.

[21] Terrell L Hill. *Statistical Mechanics: Principles and Selected Applications*. Dover Publications, 2013.

[22] Aneesur Rahman. Correlations in the motion of atoms in liquid argon. *Physical Review*, 136(2A):A405, 1964.

[23] Eric R Weeks. Introduction to the colloidal glass transition. *ACS Macro Letters*, 6:27–34, 2017.

[24] Vassiliy Lubchenko and Peter G Wolynes. Theory of structural glasses and supercooled liquids. *Annual Review of Physical Chemistry*, 58:235–266, 2007.

[25] W van Megen and HJ Schöpe. Non-equilibrium dynamics of the glass transition: new perspectives from colloidal hard spheres. *arXiv preprint arXiv:2109.14435*, 2021.

[26] Gregory B. McKenna. Dynamics and mechanics below the glass transition: The non-equilibrium state. *Computational Materials Science*, 4:349–360, 1995.

[27] Gerold Adam and Julian H Gibbs. On the temperature dependence of cooperative relaxation properties in glass-forming liquids. *The Journal of Chemical Physics*, 43(1):139–146, 1965.

[28] C Austen Angell. Formation of glasses from liquids and biopolymers. *Science*, 267(5206):1924–1935, 1995.

[29] Pablo G. Debenedetti and Frank H. Stillinger. Supercooled liquids and the glass transition. *Nature*, 410:259–267, 2001.

[30] U. Bengtzelius, W. Gotze, and Alf Sjolander. Dynamics of supercooled liquids and the glass transition. *Journal of Physics C: Solid State Physics*, 17:5915–5934, 1984.

[31] CA Angell. Relaxation in liquids, polymers and plastic crystals—strong/fragile patterns and problems. *Journal of Non-Crystalline Solids*, 131:13–31, 1991.

[32] C Austen Angell. Entropy and fragility in supercooling liquids. *Journal of Research of the National Institute of Standards and Technology*, 102(2):171, 1997.

[33] Srikanth Sastry. The relationship between fragility, configurational entropy and the potential energy landscape of glass-forming liquids. *Nature*, 409(6817):164–167, 2001.

[34] Francesco Sciortino and Piero Tartaglia. Glassy colloidal systems. *Advances in Physics*, 54:471 – 524, 2005.

[35] James Clerk Maxwell. A treatise on electricity and magnetism. *Nature*, 7:478–480.

[36] Louis de Broglie. The reinterpretation of wave mechanics. *Foundations of Physics*, 1:5–15, 1970.

[37] Arthur Ashkin. Acceleration and trapping of particles by radiation pressure. *Physical Review Letters*, 24:156–159, 1970.

[38] Arthur Ashkin. History of optical trapping and manipulation of small-neutral particle, atoms, and molecules. *IEEE Journal of Selected Topics in Quantum Electronics*, 6:841–856, 2000.

[39] Arthur Ashkin, James M Dziedzic, John E Bjorkholm, and Steven Chu. Observation of a single-beam gradient force optical trap for dielectric particles. *Optics Letters*, 11(5):288–290, 1986.

[40] David J Lockwood. Rayleigh and mie scattering. In *Encyclopedia of Color Science and Technology*. Springer, New York, NY, 2016.

[41] Christopher W Macosko. *Rheology: Principles, Measurements, and Applications*. Wiley, 1994.

[42] Sanjay K Singh. *Mechanical behaviour of viscoelastic material with changing microstructure*. PhD thesis, Memorial University of Newfoundland, 1993.

[43] Manlio Tassieri. *Microrheology with Optical Tweezers: Principles and Applications*. CRC Press, 2016.

[44] Daryl C. Preece, Rebecca L. Warren, R M L Evans, Graham M. Gibson, Miles J. Padgett, Jonathan M. Cooper, and Manlio Tassieri. Optical tweezers: wideband microrheology. *Journal of Optics*, 13:044022, 2011.

[45] Andrew B Matheson, Lynn Paterson, Amanda J Wright, Tania Mendonca, Manlio Tassieri, and Paul A Dalgarno. Optical tweezers with integrated multiplane microscopy (optimum): a new tool for 3d microrheology. *Scientific Reports*, 11(1):5614, 2021.

[46] Juho Pokki, Iliana Zisi, Ester Schulman, Dhiraj Indana, and Ovijit Chaudhuri. Magnetic probe-based microrheology reveals local softening and stiffening of 3d collagen matrices by fibroblasts. *Biomedical microdevices*, 23(2):27, 2021.

[47] Thomas Andrew Waigh. Microrheology of complex fluids. *Reports on Progress in Physics*, 68:685 – 742, 2005.

[48] Todd M. Squires and Thomas G. Mason. Fluid mechanics of microrheology. *Annual Review of Fluid Mechanics*, 42:413–438, 2010.

[49] Eric M Furst and Todd M Squires. *Microrheology*. Oxford University Press, 2017.

[50] Jean Lemaitre. *Handbook of materials behavior models, three-volume set: nonlinear models and properties*. Elsevier, 2001.

[51] Tharwat F Tadros. *Rheology of dispersions: principles and applications*. John Wiley & Sons, 2011.

[52] Benny K G Theng, F Bergaya, and G Lagaly. *Handbook of Clay Science*. Elsevier Science, 2006.

[53] Mark Kroon, Gerard H Wegdam, and Rudolf Sprik. Dynamic light scattering studies on the sol-gel transition of a suspension of anisotropic colloidal particles. *Physical Review E*, 54(6):6541, 1996.

[54] Pek-Ing Au, Siti Hassan, Jishan Liu, and Yee-Kwong Leong. Behaviour of laponite® gels: rheology, ageing, ph effect and phase state in the presence of dispersant. *Chemical Engineering Research and Design*, 101:65–73, 2015.

[55] Santosh L Tawari, Donald L Koch, and Claude Cohen. Electrical double-layer effects on the brownian diffusivity and aggregation rate of laponite clay particles. *Journal of Colloid and Interface Science*, 240(1):54–66, 2001.

[56] Maxime Delhorme, Bo Jönsson, and Christophe Labbez. Monte carlo simulations of a clay inspired model suspension: the role of rim charge. *Soft Matter*, 8:9691–9704, 2012.

[57] Barbara Ruzicka and Emanuela Zaccarelli. A fresh look at the laponite phase diagram. *Soft Matter*, 7(4):1268–1286, 2011.

[58] F Schosseler, S Kaloun, M Skouri, and JP Munch. Diagram of the aging dynamics in laponite suspensions at low ionic strength. *Physical Review E*, 73(2):021401, 2006.

[59] Barbara Ruzicka, L Zulian, E Zaccarelli, R Angelini, M Sztucki, A Moussaïd, and Giancarlo Ruocco. Competing interactions in arrested states of colloidal clays. *Physical Review Letters*, 104(8):085701, 2010.

[60] Debasish Saha, Yogesh M Joshi, and Ranjini Bandyopadhyay. Investigation of the dynamical slowing down process in soft glassy colloidal suspensions: comparisons with supercooled liquids. *Soft Matter*, 10(18):3292–3300, 2014.

[61] Jason P Rich, Gareth H McKinley, and Patrick S Doyle. Size dependence of microprobe dynamics during gelation of a discotic colloidal clay. *Journal of Rheology*, 55(2):273–299, 2011.

[62] A Shahin and Yogesh M Joshi. Physicochemical effects in aging aqueous laponite suspensions. *Langmuir*, 28(44):15674–15686, 2012.

[63] Ajay Negi and Chinedum Osuji. Dynamics of a colloidal glass during stress-mediated structural arrest. *Europhysics Letters*, 90(2):28003, 2010.

[64] Brian R. Saunders and Brian Vincent. Microgel particles as model colloids : theory, properties and applications. *Advances in Colloid and Interface Science*, 80:1–25, 1999.

[65] Ashish K. Lele, Mamta Hirve, Manohar V. Badiger, and Raghunath Anant Mashelkar. Predictions of bound water content in poly(n-isopropylacrylamide) gel†. *Macromolecules*, 30:157–159, 1997.

[66] M. Heskins and James E. Guillet. Solution properties of poly(n-isopropylacrylamide). *Journal of Macromolecular Science, Part A*, 2:1441–1455, 1968.

[67] Tomasz Śliwa and Maciej Jarzębski. Dynamic light scattering investigation of pnipam-co-maa microgel solution. *Current Topics in Biophysics*, 37:29 – 33, 2015.

[68] Yanwei Ding, Xiaodong Ye, and Guangzhao Zhang. Microcalorimetric investigation on aggregation and dissolution of poly(n-isopropylacrylamide) chains in water. *Macromolecules*, 38:904–908, 2005.

[69] Philippe Coussot. Rheometry of pastes, suspensions, and granular materials: applications in industry and environment. 2005.

[70] Peter K Morse and Eric I Corwin. Echoes of the glass transition in athermal soft spheres. *Physical Review Letters*, 119(11):118003, 2017.

[71] HJ Herrmann. Granular matter. *Physica A: Statistical Mechanics and its Applications*, 313(1-2):188–210, 2002.

[72] G Marty and Olivier Dauchot. Subdiffusion and cage effect in a sheared granular material. *Physical Review Letters*, 94(1):015701, 2005.

[73] Robert P Behringer and Bulbul Chakraborty. The physics of jamming for granular materials: a review. *Reports on Progress in Physics*, 82(1):012601, 2018.

[74] Hernán A Makse, David L Johnson, and Lawrence M Schwartz. Packing of compressible granular materials. *Physical Review Letters*, 84(18):4160, 2000.

[75] Alexei V Tkachenko and Thomas A Witten. Stress propagation through frictionless granular material. *Physical Review E*, 60(1):687, 1999.

[76] Pierre-Gilles de Gennes. Granular matter: a tentative view. *Reviews of Modern Physics*, 71(2):S374, 1999.

Chapter 2

Materials and Methods

2.1 Sample preparation

2.1.1 Preparation of Laponite suspension

Laponite® is a hygroscopic clay that exists in powder form. We conduct all the experiments reported in chapters 3-5 using Laponite XLG [1]. Laponite powder is heated in an oven for 16 to 20 hours at 120° C to remove moisture. To prepare Laponite suspension [2, 3], dried Laponite powder is gradually added to Milli-Q water under stirring conditions. In powder form, Laponite exists in one dimensional stacks called tactoids [4]. By slowly mixing the Laponite powder with Milli-Q water, we ensure that there are no lumps in the suspension. The suspension becomes turbid after mixing Laponite powder. As swelling of the Laponite tactoids takes place [5], the suspension slowly becomes clear within 10–15 min. The suspension is stirred for 45 min. After that, the suspension is loaded into different sample cells. In this thesis work, we have performed falling ball, rheological and optical tweezer measurements to probe Laponite suspensions. For rheometer- and OT-based experiments, a 0.45 micron Millipore sheet is used to filter the suspension. Due to the high sample volume (700 ml) required in the falling ball viscometer, we omit the filtering process for falling ball experiments. The physical aging of the

Laponite suspension is parametrised in terms of its aging time t_w, the time elapsed since suspension preparation. The onset of the aging process ($t_w = 0$) is defined as the moment when suspension loading in the sample cell is completed.

2.1.2 Sample cell for microscopy

All microscopy experiments have been performed using conventional sample cells. In order to prepare these sample cells, glass slides and cover slips are required. We make a solution of Hellmanex® III and water to clean the glass slides and coverslips. Using a microwave, the solution is heated until bubbles appear. The glass slide and cover slips are then dipped into the solution and sonicated for five minutes. Following the initial round of sonication, Milli-Q water is used to clean the slide and coverslips and another round of sonication is performed. This procedure is repeated

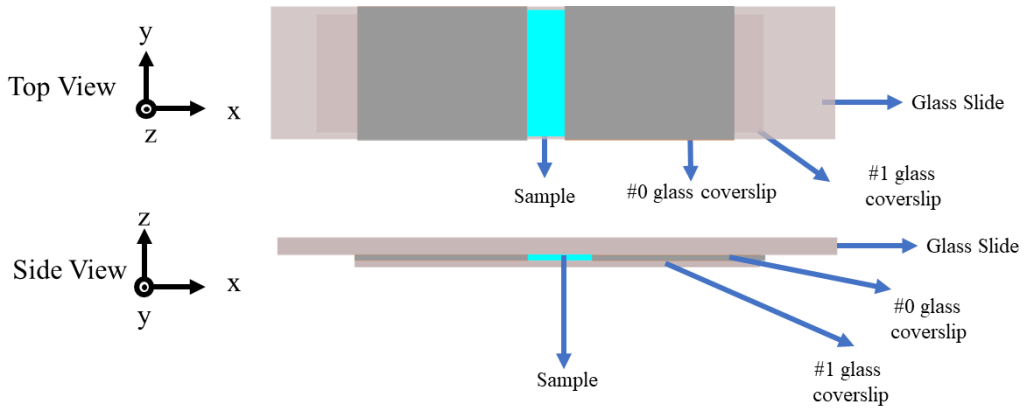

Figure 2.1: Schematic diagram of sample cell using glass slide and glass coverslips.

multiple times. Finally, an oven set to 80° C is used to dry the glass slides and cover slips. Using UV glue, we adhere two #0 coverslips to the glass slide while leaving a 5 mm gap to load the sample. The same glue is used to sandwich these #0 coverslips with a #1 coverslip. We next leave the sample cell exposed to UV light for 5 minutes to allow for solidification. The schematic diagram of the sample cell is shown in Fig.2.1.

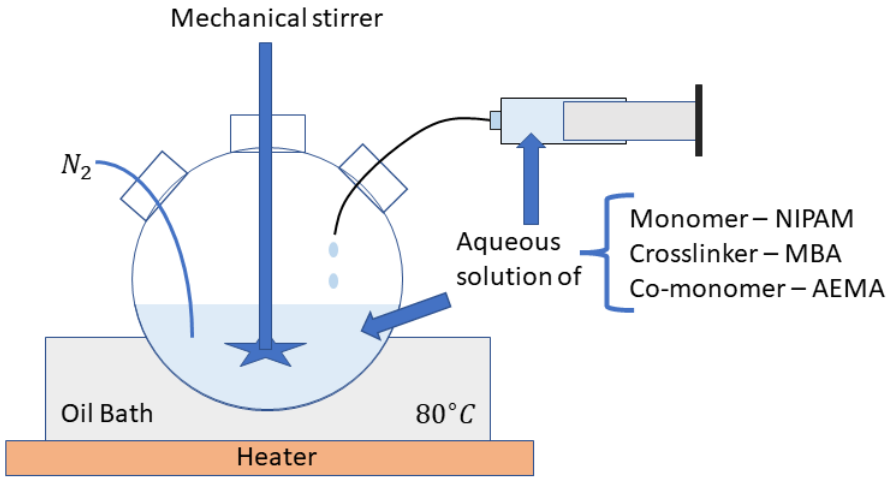

Figure 2.2: A simple illustration of semi-batch process for synthesising PNIPAM particles.

2.1.3 Functionalisation of dye and synthesis of PNIPAM particles

To functionalise fluorescein dye (Sigma-Aldrich), we add 3 g of fluorescein with 80 ml of dry tetrahydrofuran in a 250 ml round bottom flask. After mixing it for 5 min under nitrogen purging, 28 ml of triethyleamine is added. This mixture is stirred for 15 min in a nitrogen environment. The round bottom flask is kept in an ice bath and slowly 2 ml of acryloyl chloride is added while stirring. The mixture is kept overnight to equilibrate and eventually filtered to remove the triethylammonium chloride salt. The filtered sample is treated with nitrogen gas for 5 min and then kept in a desiccator equipped with rotor pump to dry the sample. The dried fluorescent crosslinker is stored at 4°C in a refrigerator and used during further synthesis of PNIPAM particles.

For PNIPAM particle synthesis, we add 2 g N-isopropylacrylamide (NIPAM $\geq$ 99%), 0.05 g N, N – methylenbisacrylamide (MBA), 0.0083 g of 2-aminoethyl methacylate hydrochloride (AEMA) and 0.1 g of functionalised fluorescein in 50 mL of Milli-Q water in a three-necked round bottom flask (RB) [6, 7]. The middle neck of the RB flask is connected to a reflux condenser. The RB flask is kept inside an oil

bath to maintain uniform temperature as shown in Fig.2.2. The other two necks of the round bottom flask are used as N_2 inlet and outlet. The ingredients in the RB flask are stirred at 500 rpm for 20 minutes under N_2 purging. After that, 30 mL of the sample is taken out using a syringe for later use. The temperature of the oil bath is increased to 80°C and 0.0114 g ammonium persulfate (APS) dissolved in 2 mL of water is added to initiate the polymerisation reaction via free radical precipitation. Nucleation sites start to form within 5 mins. The previously extracted 30 mL sample is injected using a syringe pump at a flow rate that is varied between 0.5 ml/min and 0.8 ml/min. After the process is completed, the PNIPAM latexes are cooled down rapidly in an ice bath. To remove unwanted compounds and impurities, the purified fluorescent PNIPAM particles are obtained by repeated centrifugation.

2.2 Instruments and Techniques

2.2.1 Rheometer

Rheometers are used to characterise materials based on their mechanical properties. Viscoelasticity describes the property of materials wherein they simultaneously exhibit flows like fluids and deformations like elastic materials in response to mechanical perturbations. The field of study that focuses on flow and deformation of these materials is called rheology [8]. Depending on the control parameter, a rheometer can either be stress-controlled or strain-controlled. All of the rheological tests in this thesis are performed using a stress-controlled Anton Paar MCR 501 rheometer [9], a compact and modular device. MCR 501 is a stress-controlled rheometer in which a known torque is applied and the resultant strain is measured. This rheometer features a synchronous motor supported by air bearings. The motor inside the rheometer has permanent magnets. These magnets are positioned on a tiny rotor disc and generate a continuous magnetic field, allowing for a response that is free from delay. The rotor rotates in synchrony with the field generated by a set of coils. The existence of air bearings enables the motor to move with mini-

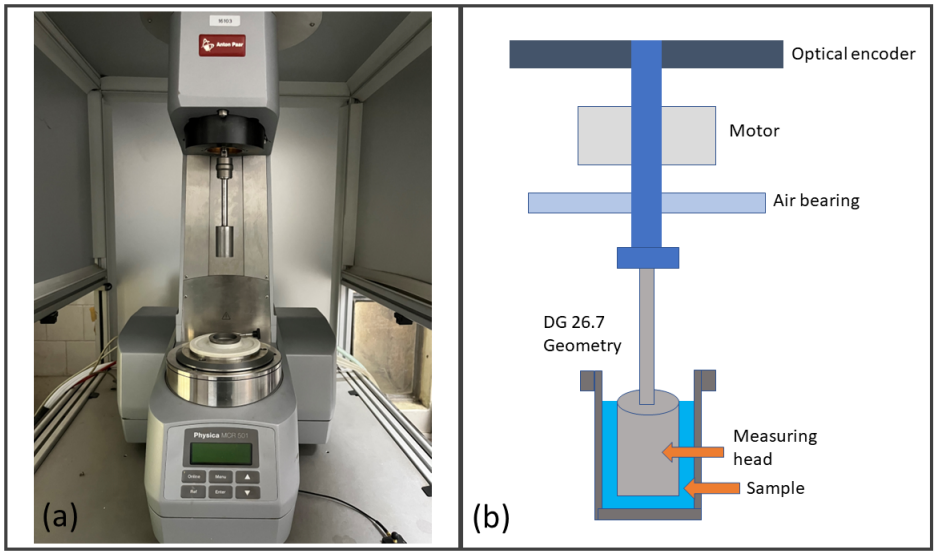

Figure 2.3: (a) Photograph of Anton Paar MCR 501 rheometer. (b) Important components of a rheometer shown in this illustration.

mal friction and a series of filters keeps the compressed air dust and moisture free. The MCR 501 rheometer includes a high-resolution optical encoder to detect strain. This optical encoder offers precise angular deflection measurements with a precision of less than 1 μrad. A photograph of the MCR 501 rheometer used by us and a schematic illustration of the different components are shown in Figs.2.3(a) and (b) respectively.

We use the parallel plate and double gap (DG) measuring heads for this thesis work. For parallel plate geometry, the schematic diagram of which is displayed on the left panel of Fig.2.4, a relatively small sample volume is necessary. Due to the adjustable gap, various measuring conditions like application of an external uniform electric field can be simultaneously achieved. Highly viscous samples, dispersions, gels, pastes and soft solids can be examined using this geometry. Another benefit is the simple and efficient cleaning process for this geometry due to its shape. DG geometry (Fig.2.4, right panel) consists of a cylindrical hollow measuring head and a cylindrical base with the sample filled in between. DG geometries allow for a large contact area between the sample and the surface measuring head. With these geometries, one can test liquids with low viscosity (water) with a high torque

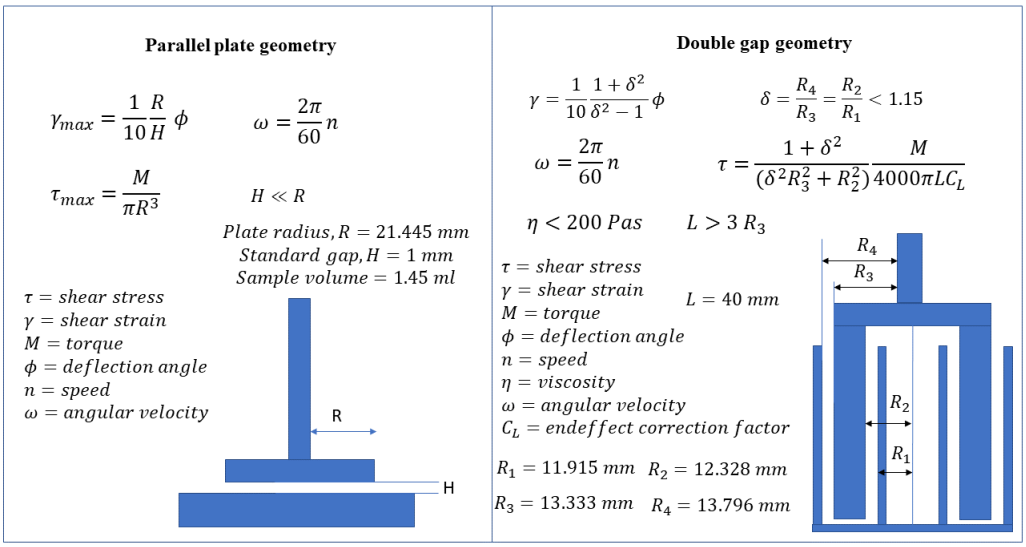

Figure 2.4: The schematic diagrams of parallel plate and double gap geometries are shown along with calculations of important parameters. These figures are adapted from [9].

resolution. Advantages of such a system include its large exposed surface area and thermal stability. Also, turbulence occurs only at extremely high shear rates.

2.2.2 Falling ball viscometer

The falling ball viscometer is a well-established and widely used technique for measuring the viscosity of Newtonian fluids. The schematic diagram of our falling ball viscometer is shown in Fig.2.5(a). The viscometer is inserted in a water bath whose temperature is maintained at 25°C by using a temperature controller (Polyscience Digital, Inc.). The sample (≈ 700 ml) is loaded into the cylindrical viscometer shown in Fig.2.5(b). An electro-magnet shown in Fig.2.5(c) is used to drop steel balls along the vertical axis of the tube and is positioned at a fixed height of 1.5 cm above the surface of the sample. The path followed by the ball is recorded with an IDT Motion Pro Y4-S2 high-speed camera [Fig.2.5(d)] at 100 fps for all balls. The position of the falling ball is tracked from the recorded images by using a video spot tracker software (Computer Integrated Systems for Microscopy and Manipulation). Samples are filled in the falling ball viscometer up to a height of 56 cm–57 cm.

According to the work of Tanner [10], end effects are insignificant if the ball is away from the bottom of the container by a distance that is more than the viscometer radius. Following this, and since the radius of our viscometer is 2 cm, we track the falling balls for a maximum of 54 cm from the top of the container (or 2 cm from the bottom). The yellow line in Fig.2.5(e) is a representative ball trajectory and is constructed from the position of the ball centroid in each frame. The velocity of the falling ball is calculated by time-differentiating the positions of the ball centroids using a central differential formula.

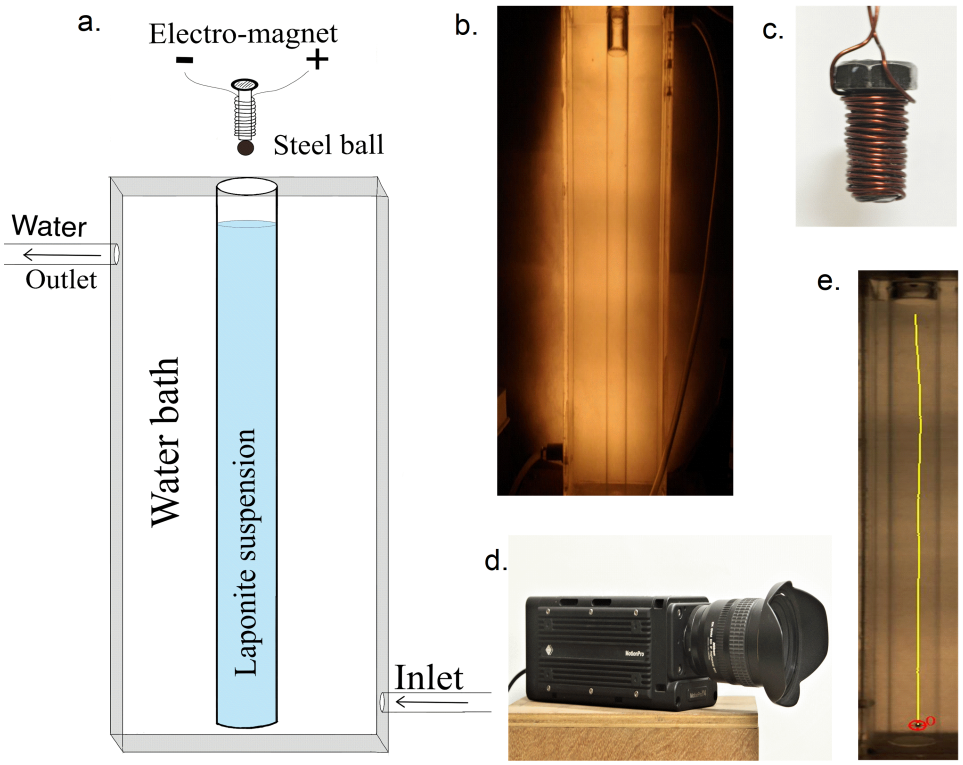

Figure 2.5: (a) Schematic diagram of the experimental setup for ball-drop experiments. (b) A cylindrical tube (length 65 cm and diameter 4 cm) filled with sample is placed inside a water bath at 25°C. (c) The electro-magnet used to drop steel balls. (d) High-speed camera—IDT Motion Pro Y4-S2. (e) Trajectory of a falling ball in the viscometer displayed in (b), tracked using a video spot tracker (CISMM), is shown by a yellow line.

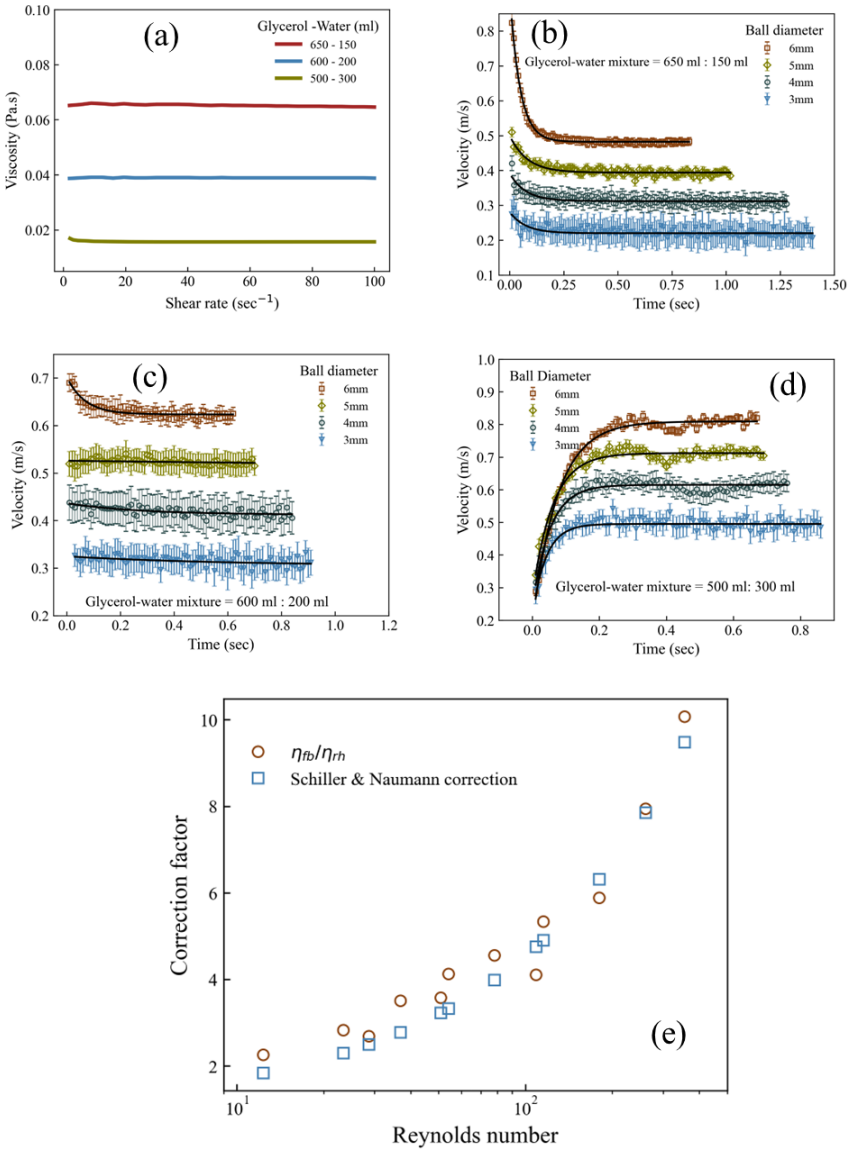

Figure 2.6: (a) Viscosities of three glycerol-water mixtures having different proportions of glycerol and water are measured in a rheometer at 25° C. Time dependents velocities of balls having diameters 3 – 6 mm falling in Newtonian fluids (glycerol water mixtures displayed in (a) having viscosities 0.065, 0.039 and 0.016 Pa.s) are shown in (b), (c) and (d) respectively. The hollow symbols represent the experimental data (error represented using vertical bars) and solid black lines are the fits to $V = V_0 + (V_0 - V_{ter})\exp(t/\tau)$, where V_0, V_{ter} and τ are fitting parameters. (e) The ratio of viscosities measured using the falling ball viscometer and rheometer. The correction factors computed according to the Schiller and Naumann criterion are plotted versus Reynolds number.

Calibration of falling ball viscometer

To calibrate the falling ball viscometer, we use Newtonian fluids of different viscosities. We prepare standard Newtonian fluid samples by mixing water and glycerol of different volumes. The viscosities of these mixtures are first measured using a rheometer as shown in Fig.2.6(a). Falling ball viscometry is then used to track the motion of a ball falling through the mixture. The viscosity of the mixture is computed from the terminal velocity of the ball. The time dependent velocities of the balls of different sizes falling through glycerol-water mixtures are displayed in Figs.2.6(b,c,d). We find that the flow regime for these experiments falls in the intermediate Reynolds number regime. Reynolds number of the flow surrounding the falling ball is calculated using the following formula, $Re = V_{ter} D \rho_f / \eta$, where V_{ter} represents the terminal velocity achieved by the ball, D is the diameter of the ball, ρ_f stands for the density of the fluid, and η denotes the dynamic viscosity of the fluid. So the viscosities measured using the rheometer and falling ball viscometry for the same mixture do not match and a correction factor is required to calibrate the falling ball viscometer. The correction factor for drag are computed for various Reynolds numbers and are plotted in Fig.2.6(e). All calculated parameters are shown in Table 2.1. The viscosity in the 2nd column of the table is reported from the articles based on Cheng's work [11, 12]. The correction factor for computing viscosity due to non-laminar flow at the intermediate Reynolds numbers studied here is given by the Schiller and Naumann criterion [13, 14]. We also calculate the wall effect [15] and it is found to be negligible for our experimental set-up.

Drag correction:

Drag coefficient, C_d for very small Reynolds number where the flow remains laminar is given by,

$$Re < 1 : C_d = 24/Re \tag{2.1}$$

Viscosity measured using rheometer $(Pa.s)$	Viscosity from literatures $(Pa.s)$	Diameter of the ball (m)	Terminal velocity (m/s)	Reynolds number	Drag coefficient C_D	Corrected viscosity from terminal velocity$(Pa.s)$	Ratio of ball and tube diameter	Wall factor
0.065	0.075	0.006	0.482	54.172	1.474	0.080	0.15	0.995
		0.005	0.393	36.860	1.815	0.081	0.125	0.995
		0.004	0.311	23.361	2.370	0.079	0.1	0.999
		0.003	0.219	12.347	3.583	0.079	0.075	0.999
0.039	0.041	0.006	0.623	115.307	1.022	0.042	0.15	0.999
		0.005	0.505	78.024	1.228	0.044	0.125	0.999
		0.004	0.412	50.831	1.524	0.043	0.1	0.999
		0.003	0.305	28.597	2.099	0.041	0.075	0.999
0.016	0.015	0.006	0.809	355.514	0.640	0.016	0.15	0.999
		0.005	0.711	260.668	0.723	0.016	0.125	0.999
		0.004	0.614	180.078	0.841	0.014	0.1	0.999
		0.003	0.494	108.739	1.050	0.013	0.075	0.999

Table 2.1: Viscous drag and wall effect corrections for Newtonian glycerol-water mixtures, fluids computed according to the protocols specified in this section.

Drag coefficient for low and intermediate Reynolds number (Re) as given by Schiller and Naumann criterion [13, 14],

$$1 < Re < 1000 : C_d = 24/Re * (1 + 0.15Re^{0.687}) \tag{2.2}$$

Wall correction

The wall factor given by Kehlenbeck and De Felice is [15],

$$f_{wall} = (1 - l^p)/(1 + (l/l_o)^p) \tag{2.3}$$

where $l = D/D_t$, D is diameter of the ball, D_t = diameter of the tube and both l_o and p are functions of Re as follows,

$$(l_o - 0.283)/(1.2 - l_o) = 0.041Re^{0.524} \tag{2.4}$$

$$Re \leq 35 : p = 1.44 + 0.5466Re^{0.434} \tag{2.5}$$

$$Re > 35 : p = 2.3 + 37.3Re^{(-0.8686)} \tag{2.6}$$

We see from Table.2.1 and Fig.2.6(e) that the Schiller-Naumann correction pro-

duces an excellent match between viscosity data obtained in a rheometer and in a falling ball viscometer. Furthermore, we see that the wall effect is less than 1% in all the experiments.

2.2.3 High speed imaging

For high speed imaging, a Nikon AF-S NIKKOR 12-24mm lens is attached to an IDT MotionPro Y4-S2 CMOS camera [16]. A photograph of the camera is shown in Fig.2.5(d). For high speed imaging of an object falling through a medium, we use an intense light source with a white sheet. This is required to diffuse the light uniformly. The camera has maximum resolution of 1024×1024 and maximum frame rate of 4500 frames per second. Minimum exposure time for this device is 1 μs. The sensor is CMOS-Polaris II of size 13.9 × 13.9 mm.

2.2.4 Optical tweezer

We use a Thorlabs optical tweezer (OT) module [17] for our experiments. The schematic of the OT setup is shown in Fig.2.7. A continuous wave solid-state fibre laser (YLR-5-1064-LP, IPG Photonics USA) generates a Gaussian beam profile at a wavelength of 1064 nm. The beam is expanded by lenses L1 and L2 to fill the back aperture of an objective lens. The expanded beam is then passed into a high numerical aperture (NA =1.3) objective lens (Oil immersion, UPLFLN100XO2) of magnification 100X using dichroic and M2 mirrors. The objective focuses the beam to a diffraction-limited spot inside a sample cell. The highly focused beam can trap an object in three dimensions. The light scattered by the trapped particle is collected by a condenser lens (Nikon 10x) and then imaged on a position sensing quadrant photodiode (QPD - PDQ80A, Fig.2.7) to measure the nanometer-scale displacements of the trapped probe particle and the forces exerted on it. The voltage signals from the QPD are recorded at a sampling frequency of 1000 Hz using a data acquisition card (National Instruments, USA) and custom software (LabView 2021). A sample cell containing a sample is mounted on the piezoelectric sample stage

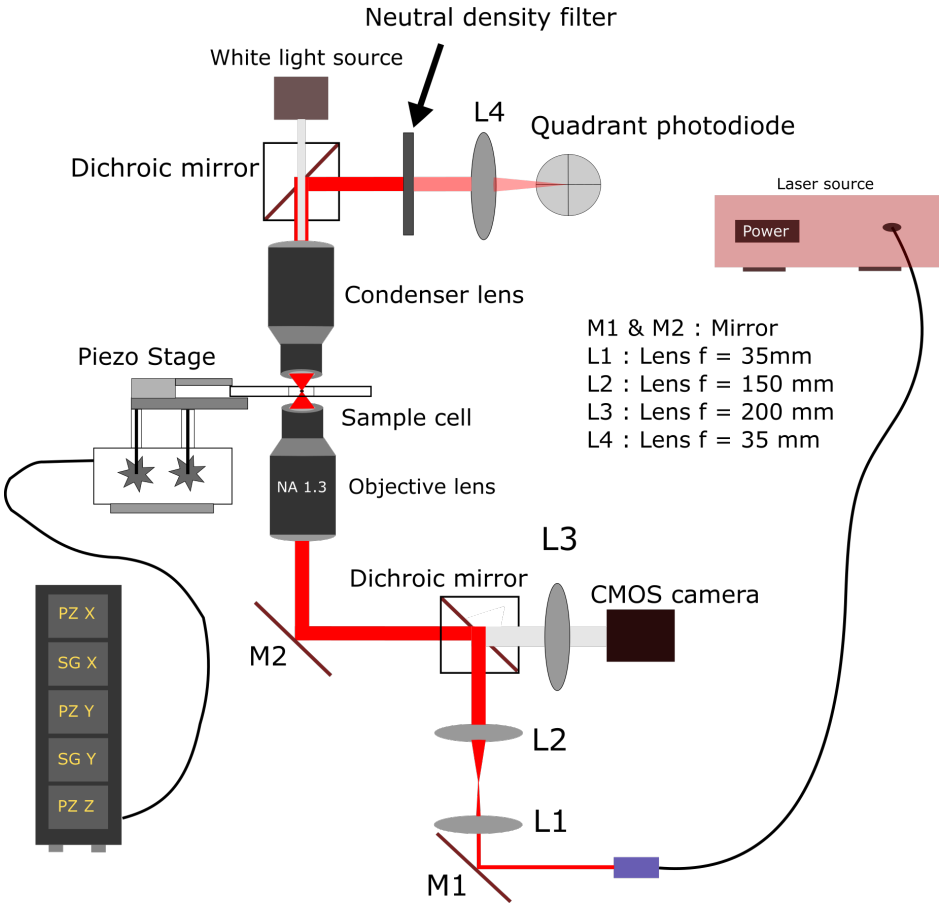

Figure 2.7: Schematic diagram of the optical tweezer set-up. The infrared laser beam is indicated in red.

(TBB1515/M, Thorlabs), which is oscillated at the desired amplitude and frequency using a 3-axis XYZ translational stage (NanoMax-TS, Thorlabs), three piezoelectric actuators (TPZ001, Thorlabs) and two strain gauges (TSG001, Thorlabs). The sample cell is constructed using one glass slide and one #1 coverslip (thickness $\approx$ 150 μm, Blue Star, India) and #0 coverslips (thickness $\approx$ 100 μm) as the spacers, as shown in Fig.2.1(a). All the experiments were performed at room temperature $\approx$ 22°C.

Calibration of optical tweezer

The sample stage consists of a slide holder with a 3-axis XYZ translational stage, piezoelectric actuators and strain gauges. We apply a voltage to the piezoelectric

actuators which results in the movement of the sample stage in the desired direction. The strain gauges measure the accurate position of the sample stage for feedback controlled spatial movement. The conversion factor for calibrating the voltage applied to the piezoelectric actuators to the net distance travelled by the sample stage is next computed. We prepare a glass microchannel containing a tiny amount of polystyrene beads suspended in 0.5 mM NaCl aqueous solution. The beads get attached to the glass coverslip in a high salt environment which allows us to acquire the bead position using a CMOS camera as we apply a voltage to the piezoelectric actuators. The slope of the plot of stage displacement versus voltage applied to the piezoelectric actuators gives a voltage to displacement conversion factor of 0.25 μm/V as seen from Fig.2.8(a).

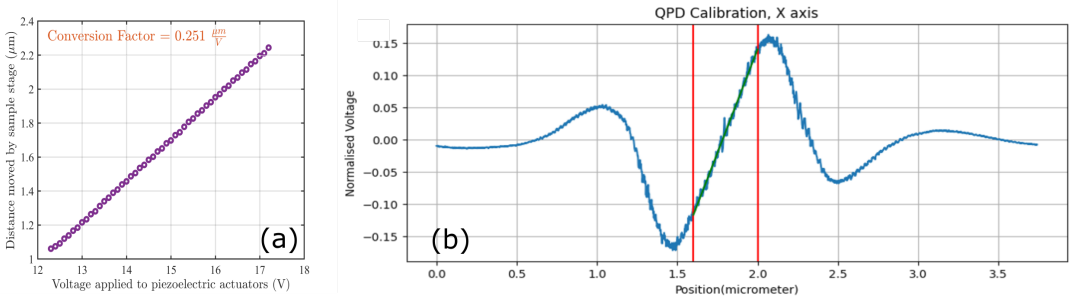

Figure 2.8: (a) Distance travelled by the sample stage is measured as a function of the voltage applied to the piezo actuator. The calibration factor, computed from the slope of the curve, is 0.251 μm/V. (b) Position calibration of the QPD is performed by shifting a bead attached to a glass coverslip along the x-axis of the sample cell (shown in Section 2.1.2) by a predetermined distance from the laser's beam centre. The QPD signal is acquired during this movement and plotted against the motion of the trapped bead. We determine the sensitivity of the QPD, 1.51 nm/QPD unit, by fitting the linear region of the curve with a straight line.

High-frequency position measurement of an optically trapped bead using a quadrant photodiode requires a relation between QPD output voltage and bead position data. To determine this relation, also called QPD sensitivity, we moved a bead attached to the glass coverslip along the x and y axes such that the bead passes through the centre of the laser spot while the QPD output voltages are simultaneously measured. The QPD output voltage is linearly related to the bead position in a narrow trap region between the two parallel red lines as displayed in Fig. 2.8(b).

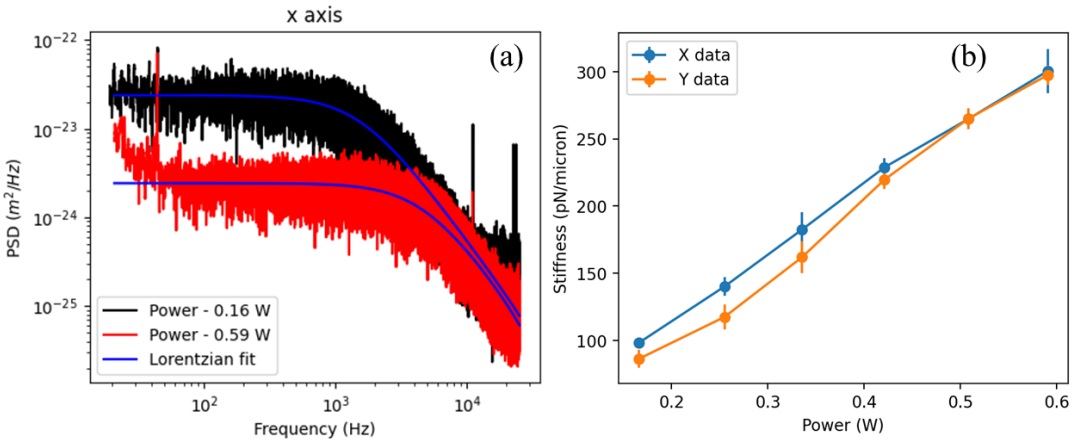

Figure 2.9: (a) Power spectrum of a trapped bead is plotted at two different laser powers and fitted (blue lines) with Lorentzian function. (b) Trap stiffness is plotted as a function of laser power for 1 μm polystyrene bead trapped in water along both x and y axes.

The slope of the linear region yields a QPD sensitivity of 1.51 nm/QPD unit.

The trap stiffness depends on applied laser power [18]. We trap a polystyrene bead (1 μm) suspended in water and measure its movement at a sampling frequency of 50 kHz. The Fourier transform of the bead position is fitted to the Lorentzian function, PSD $= A/(f^2 + {f_c}^2)$ shown in 2.9(a), where A depends on the surrounding temperature, f is the frequency, $f_c = \kappa/2\pi\gamma$ is the corner frequency and γ is the coefficient of viscosity of the medium [18]. The trap stiffness κ increases with laser power. The data is plotted in Fig.2.9(b).

2.2.5 Cryo-FESEM

We use a field emission scanning electron microscope from Carl Zeiss [19] with an electron beam strength of 5 kV. This instrument is used in this thesis to image microstructures in Laponite suspensions. For imaging purposes, a freshly prepared Laponite suspension is loaded in a capillary tube (Capillary Tube Supplies Ltd, UK) with a diameter of 1 mm using capillary flow. The capillary tube is next

sealed and kept undisturbed at room temperature for the desired aging time. The tubes loaded with the sample were then vitrified quickly in liquid nitrogen slush at $-207°C$ and transferred into a vacuum chamber at $-150°C$ (PP3000T Quorum technology). Next the tubes filled with the frozen sample were cryo-fractured using an in-built knife. The sample is next sublimated at a temperature of $-90°C$ for 20 minutes to remove the water content at the upper surface. Finally, a layer of platinum is coated on the sample surface for enhanced contrast during scanning electron microscopy. The surface images of the Laponite suspension were produced by capturing back-scattered secondary electrons. All the cryo-FESEM images were analysed using ImageJ software (developed by Wayne Rasband, NIH, US).

2.2.6 Confocal microscope

A confocal microscope can acquire high resolution images using an optical sectioning method. In a traditional fluorescent microscope, the whole sample is illuminated using light. As a result, out of focus light from the sample contributes to forming blurry images. The confocal microscope was developed to overcome this problem [20, 21]. The general idea is to introduce a pinhole aperture to block the light contributed by the background. This is implemented by keeping a pinhole at the conjugate plane of the specimen plane. This is followed by a second pinhole which is placed in front of a photo-multiplier tube (PMT) detector, so that it can only detect signals originating from a small region. To scan the whole specimen along x and y directions, a galvo-mirror is used. In confocal microscopy, a three-dimensional image of a sample can also be reconstructed from a series of two-dimensional images captured at different depths within the sample [22]. Upon acquiring images from several small sections, the data is merged to generate a complete three dimensional image of the sample. Confocal microscopy images of aqueous suspensions of PNIPAM particles are acquired for this thesis using a Leica TCS SP8 confocal microscope system with a 100x Nikon plan oil immersion objective having numerical aperture NA = 1.40. A general schematic illustration of the confocal setup is shown in Fig.2.10. Since

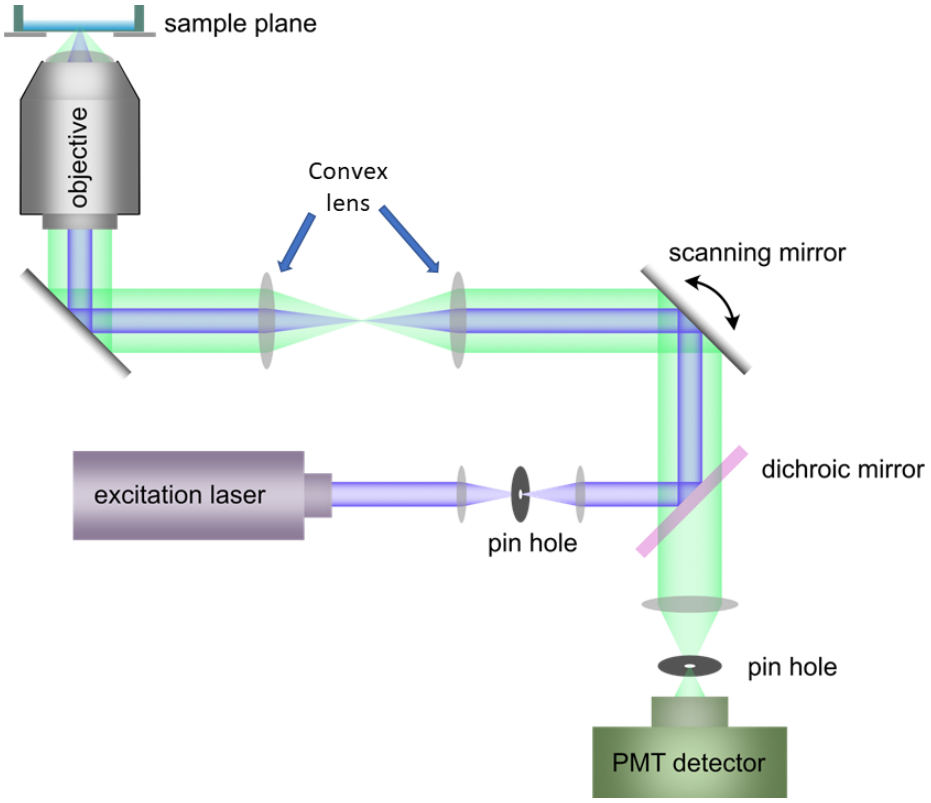

Figure 2.10: Schematic illustration of a confocal microscope setup is shown. The blue beam is the excitation laser and the green beam is the fluorescent signal coming from the sample.

swollen PNIPAM particles in an aqueous solvent have a refractive index that is similar to water, it is not possible to distinguish them in brightfield microscopy. A fluorescein dye is attached to the PNIPAM particles and excited using a 488 nm argon laser in the confocal microscope setup. A photo-multiplier sensor is used as a detector for the output signals having longer wavelengths.

2.2.7 Electrodynamic shaker

An electrodynamic vibration shaker is a common instrument to test the effect of vibration on granular materials. For our experiments, we employed the DEV-005 shaker from DESPL. It is made up of two major components: the power supply and the shaker. There are two coils within the shaker. The shaker is simply an electrodynamic assembly that consists of a double-fold magnetic circuit with a sta-

tionary and moving coil. A field coil is a stationary coil. The moving coil is linked to the upper level, where tests are carried out. The force F on the vibrating plate is calculated using the following formula,

$$F = I \times B \times L \tag{2.7}$$

where I is the current in the drive coil, B is the magnetic flux density generated by the field coil and L is the length of the drive coil.

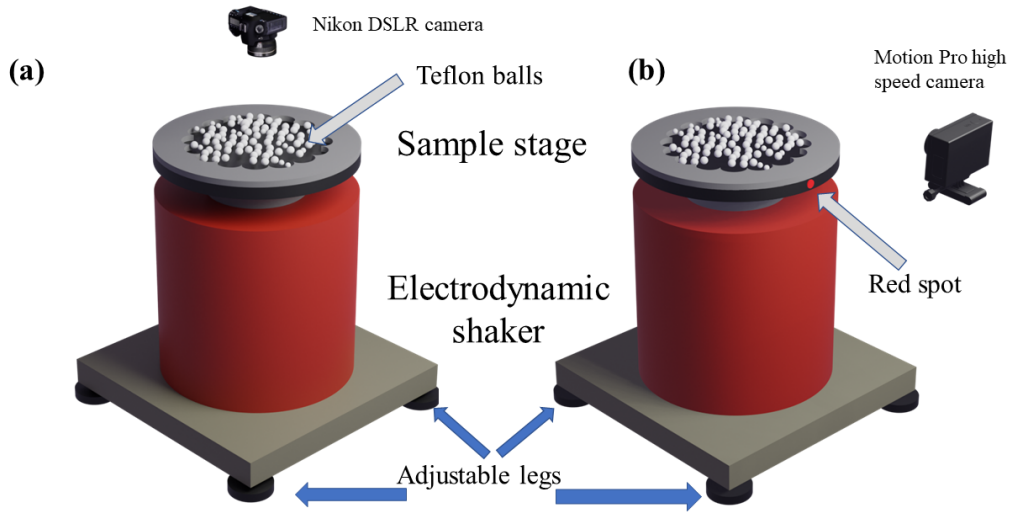

Figure 2.11: (a) The schematic illustration of our set-up is shown while recording a video of the granular particles during stage vibration. (b) This configuration is used to calibrate the vibration amplitude and frequency by capturing the movement of the red spot using a high speed camera.

By varying the current, amplitude A and frequency f of the shaker stage can be varied and adjusted to the desired value. Generally, the vibration of a shaker is quantified using a non-dimensional acceleration, Γ and it can be calculated using the following relation [23],

$$\Gamma = \frac{A(2\pi f)^2}{g} \tag{2.8}$$

To calibrate the vertical vibration of the shaker, we utilise a high-speed camera

(Motion PRO Y4-S2) aligned perpendicularly with the direction of the vibrations or oscillations of the shaker and record images at a frame rate of 300 per second. A schematic illustration of the set-up is shown in Fig.2.11(a). We mark a red spot on the vibrating plate (Fig.2.11(b)). This red spot is tracked using a video spot tracker (Computer Integrated Systems for Microscopy and Manipulation) and displacements of the stage are obtained with time. The predetermined calibration factor of the high-speed camera (pixel to micrometre) enables us to determine the vertical stage displacement amplitude with micrometre accuracy. The obtained displacements of the red spot with time is then Fourier transformed to find the vibration frequency (f) shown in Fig.2.12. For all our experiments, we keep stage oscillation amplitude $A = 47\ \mu m$ and frequency $f = 78$ Hz, resulting in a non-dimensional acceleration ($\Gamma = 1.15$ calculated using Eqn.2.8) greater than one.

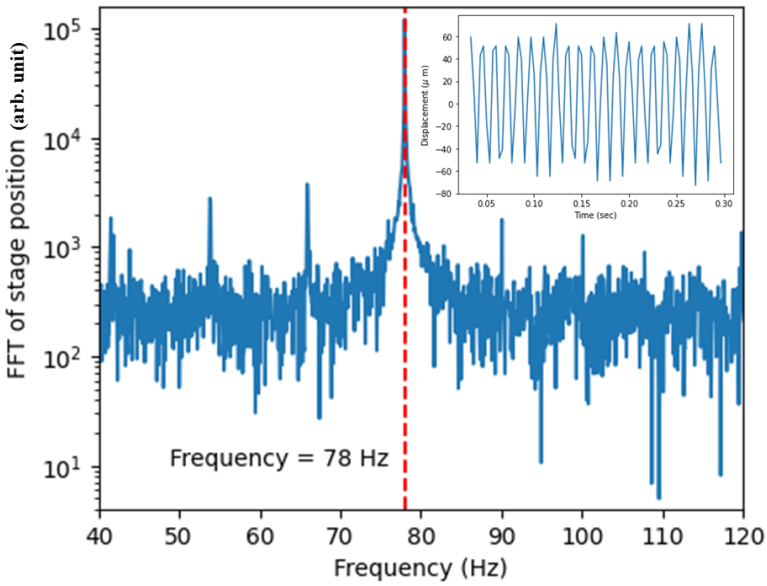

Figure 2.12: Fourier transform of the vertical stage oscillation, as obtained by tracking a red spot in the side of the shaker. Red dashed line indicates the peak of the signal. The displacement of the red spot due to vertical vibrations of the shaker plate is plotted *vs.* time in the inset.

Bibliography

[1] Barbara Ruzicka and Emanuela Zaccarelli. A fresh look at the laponite phase diagram. *Soft Matter*, 7(4):1268–1286, 2011.

[2] Rajkumar Biswas, Debasish Saha, and Ranjini Bandyopadhyay. Quantifying the destructuring of a thixotropic colloidal suspension using falling ball viscometry. *Physics of Fluids*, 33(1):013103, 2021.

[3] Debasish Saha, Yogesh M Joshi, and Ranjini Bandyopadhyay. Kinetics of the glass transition of fragile soft colloidal suspensions. *The Journal of Chemical Physics*, 143(21), 2015.

[4] Samim Ali and Ranjini Bandyopadhyay. Use of ultrasound attenuation spectroscopy to determine the size distribution of clay tactoids in aqueous suspensions. *Langmuir*, 29(41):12663–12669, 2013.

[5] Samim Ali and Ranjini Bandyopadhyay. Evaluation of the exfoliation and stability of na-montmorillonite in aqueous dispersions. *Applied Clay Science*, 114:85–92, 2015.

[6] Tim Still, Ke Chen, Ahmed M Alsayed, Kevin B Aptowicz, and AG Yodh. Synthesis of micrometer-size poly (n-isopropylacrylamide) microgel particles with homogeneous crosslinker density and diameter control. *Journal of Colloid and Interface Science*, 405:96–102, 2013.

[7] Sanjay Kumar Behera, Debasish Saha, Paramesh Gadige, and Ranjini Bandyopadhyay. Effects of polydispersity on the glass transition dynamics of aqueous

suspensions of soft spherical colloidal particles. *Physical Review Materials*, 1(5):055603, 2017.

[8] Christopher W Macosko. *Rheology: Principles, Measurements, and Applications*. Wiley, 1994.

[9] Anton paar mcr 501 rheometer users manual. *https://www.isis.stfc.ac.uk/Pages/sans-rheometer-user-information9814.pdf*.

[10] RI Tanner. End effects in falling-ball viscometry. *Journal of Fluid Mechanics*, 17(2):161–170, 1963.

[11] Nian-Sheng Cheng. Formula for the viscosity of a glycerol- water mixture. *Industrial & Engineering Chemistry Research*, 47(9):3285–3288, 2008.

[12] Andreas Volk and Christian J Kähler. Density model for aqueous glycerol solutions. *Experiments in Fluids*, 59(5):75, 2018.

[13] Walter RA Goossens. Review of the empirical correlations for the drag coefficient of rigid spheres. *Powder Technology*, 352:350–359, 2019.

[14] L Schiller. Über die grundlegenden berechnungen bei der schwerkraftaufbereitung. *Z. Vereines Deutscher Inge.*, 77:318–321, 1933.

[15] RP Chhabra, S Agarwal, and K Chaudhary. A note on wall effect on the terminal falling velocity of a sphere in quiescent newtonian media in cylindrical tubes. *Powder Technology*, 129(1-3):53–58, 2003.

[16] Idt cameras specification manual, integrated design tools, inc., 2010. *https://idtvision.com/products/cameras/y-series-cameras/?cn-reloaded=1*.

[17] Modular optical tweezers - thorlabs, inc. *https://www.thorlabs.com*.

[18] Jan Gieseler, Juan Ruben Gomez-Solano, Alessandro Magazzù, Isaac Pérez Castillo, Laura Pérez García, Marta Gironella-Torrent, Xavier Viader-Godoy,

Felix Ritort, Giuseppe Pesce, Alejandro V Arzola, et al. Optical tweezers—from calibration to applications: a tutorial. *Advances in Optics and Photonics*, 13(1):74–241, 2021.

[19] User's guide: Ultra-plus fesem, carl zeiss , 2013. *www.zeiss.com*.

[20] JG White, WB Amos, and M Fordham. An evaluation of confocal versus conventional imaging of biological structures by fluorescence light microscopy. *The Journal of Cell Biology*, 105(1):41–48, 1987.

[21] W Brad Amos, JG White, and Michael Fordham. Use of confocal imaging in the study of biological structures. *Applied Optics*, 26(16):3239–3243, 1987.

[22] Stephen W Paddock. *Confocal Microscopy: Methods and Protocols*. Humana Totowa, NJ, 1999.

[23] Prakhyat Hejmady, Ranjini Bandyopadhyay, Sanjib Sabhapandit, and Abhishek Dhar. Scaling behavior in the convection-driven brazil nut effect. *Physical Review E*, 86(5):050301, 2012.

Chapter 3

Quantifying the destructuring of a thixotropic colloidal suspension using falling ball viscometry

3.1 Introduction

The settling dynamics of objects in a non-Newtonian aging suspension leads to very interesting modifications of Stokesian flows. It is well known that for an object falling through a Newtonian medium under gravity, a terminal velocity, V_{ter}, arises due to a balance between the surface drag on the object and its buoyant weight. For low Reynolds numbers, the flow around the surface of the object remains laminar. In this regime, the drag force is linearly proportional to the velocity. The relation between terminal velocity and drag coefficient of an object falling through a viscous medium at low Reynolds numbers ($Re < 1$) was first determined by Stokes in 1851 [1]. The differential equation for a falling ball inside a Newtonian fluid can be written as, $m\dot{V} = -\kappa V + F_b$, where $\dot{V}$ = time derivative of the instantaneous velocity V of the ball, κ = drag coefficient, m = mass of the ball, F_b = buoyant force. Solving this

equation, we can write the expression for velocity, V:

$$V = V_{ter} + (V_0 - V_{ter}) \exp(-t/\tau) \tag{3.1}$$

where V_0 = initial velocity and $V_{ter} = (\rho_s - \rho)gD^2/18\eta$, $\tau = m/\kappa$, where $\kappa = 3\pi\eta D$, η = viscosity of the fluid, D = diameter of the ball, ρ_s = density of the ball, ρ = density of the fluid, g = acceleration due to gravity. For high Reynolds numbers $(10 - 500)$, the flow does not remain laminar around the ball even though it attains a steady state. Eqn.3.1 can be used for a range of Reynolds numbers by including the appropriate correction factor for drag [2]. The dependence of the drag coefficient on the Reynolds number has been investigated extensively for Newtonian fluids [3–6]. For intermediate Reynolds number, an empirical form of correction factor was proposed by Schiller and Naumann [2, 4]. It has also been reported that fluid motion around a ball remains symmetric in Newtonian fluids, while the symmetry is broken when the ball falls through an aging viscoelastic fluid with a finite yield stress [7, 8].

Novel dynamical behaviours emerge in viscoelastic materials such as polymers, gels and particulate suspensions due to shear thinning, shear thickening, non-zero normal stresses and yield stresses [9–11]. The bulk rheological response of a non-Newtonian complex structured fluid can be correlated with its structural details at microscopic length scales. Bio-materials like human blood [12], collagen [13], silk fibre [14] exhibit thixotropic behaviour. These complex bio-materials are used in disease detection and treatment, cell carrier therapy, bio-printing etc. The quality of common everyday materials such as toothpaste, cosmetics, paint, mayonnaise, clays etc., can also be improved by understanding their non-Newtonian flow [15]. The recovery of oil from soil, which consists of different clay compounds, sand, organic matter, oil and water in varying proportions, can be enhanced with the knowledge of the flow of particles in non-Newtonian fluids [16].

Recently, flow patterns around objects falling through Xanthan gum suspensions have been studied [17]. Falling ball viscometry is a simple but elegant technique to

study non-Newtonian fluids. In this method, the motion of a ball falling through a medium is tracked to obtain information about the properties of the latter. Such experiments can effectively probe the complex flow properties of fluids whose structures continually evolve with time [18]. In a worm-like micellar solution, the motion of a falling ball can lead to instabilities [19, 20], with larger balls seen to oscillate in the direction of their fall due to shear induced structural deformation of the underlying medium during their passage. Oscillatory motion was also observed for rising bubbles in a worm-like micellar solution [21]. The velocity of a spherical ball in Bentonite clay suspensions was found to increase continuously over a period of time [22]. For non-Newtonian fluids in general, observations like shear dependent viscosity, fore-aft asymmetry, negative wake and change in yielding behaviour with aging time make the motion of the falling object more complicated [7].

In this work, the motion of a ball falling through aging Laponite suspensions is studied. A detailed discussion on the aging of Laponite suspension can be found in section 1.6 of Chapter 1. The rheological behaviour of aging Laponite suspensions has a strong dependence on the preparation protocol. It can vary noticeably between a freshly prepared sample and one that has been rejuvenated (where aging has been reinitialized by shearing a spontaneously evolving suspension). A partial irreversibility in aging behaviour upon rejuvenation is also observed [23] and understood by considering that the structural build-up in Laponite suspensions for long aging times cannot be destroyed even by applying very large shear deformations. A dichotomic aging behaviour, indicating different aging dynamics in freshly prepared and rejuvenated Laponite suspensions, was observed using X-ray photon correlation spectroscopy and dynamic light scattering [24]. It has been reported that a ball dropped in a rejuvenated Laponite suspension gets stuck inside the fluid [18] or oscillates during its fall [25]. The critical stress value that has to be exerted by the ball to exhibit these contrasting behaviours depends on the ball size and density, and the aging time, t_w, defined as the time since preparation of the Laponite suspension [26]. It is observed that the medium in the immediate neighbourhood of

the surface of the ball fluidizes due to the shear-induced viscous thinning that arises from the disruption of the micro-structure due to the passage of the ball. Regions far from the ball are less fluid-like in comparison [27]. Most falling ball experiments performed in Laponite suspensions have used rejuvenated samples [18, 25]. Since falling ball viscometry has not been performed in spontaneously aging Laponite suspensions to the best of our knowledge, we have conducted a systematic study to probe the evolution of the underlying microscopic structures in freshly prepared Laponite suspensions.

In this chapter, balls of different sizes are dropped into freshly prepared Laponite suspensions having different initial states of structure that depend on the suspension age quantified by the waiting time, t_w, since sample preparation. The motion of the ball falling in Laponite suspensions is captured using a high speed camera and is observed to differ qualitatively from the trajectory of a ball falling through a Newtonian fluid. We note that while a ball falling through a Newtonian liquid of comparable viscosities reaches a steady state within the experimental time window, the velocity of a ball dropped in the Laponite suspension continues to increase, with the increase being more dramatic for the larger balls used in this study. Interestingly, the larger balls used in this study, when dropped in the Laponite suspensions of ages 1-3 hrs explored here, do not reach a steady state over the entire duration of the experiment. We modify an existing rheological model [28] for time-dependent changes in the structure of an aging non-Newtonian fluid to explain our experimental observations. We show here that when the time of fall of the ball is much faster than the aging time of the medium, fits of our experimental ball-drop data to the model can be used to successfully extract the destructuring time scales of aging Laponite suspensions.

3.2 Experimental Methods

Sample preparation protocols and basics of our falling ball viscometery are discussed in section 2.1.1 and 2.2.2 of Chapter 2. After filtration, a freshly prepared Laponite suspension ($\approx$ 700 ml) is loaded into the cylindrical viscometer. Once sample loading is complete, the top of the cylindrical tube is covered with parafilm to isolate the Laponite suspension from the atmosphere. The suspension is left to age, and its micro-structure is allowed to develop spontaneously due to the physical aging process. The aging time of the Laponite suspension is assigned the value $t_w = 0$ as soon as sample loading is completed. Aging time is measured from the moment the viscometer is loaded until the time the ball is dropped in the viscometer. The sample age is monitored continuously using a stopwatch for the entire duration of the experiment. The parafilm that is used to cover the Laponite suspension immediately after loading is removed just before the ball is dropped. An electro-magnet is used to drop steel balls along the vertical axis of the tube and is positioned at a fixed height of 1.5 cm above the surface of the Laponite suspension. This method of ball-drop is adopted since Laponite suspensions, particularly of higher ages, were seen to stick to the surface of the ball when the latter is immersed entirely in the suspension. The instant at which the falling ball enters the Laponite medium is recorded as time $t = 0$. The corresponding ball velocity is designated as initial velocity, V_0. Experiments are performed at several aging times corresponding to different structural states of the Laponite suspensions. After predetermined aging times t_w, the parafilm cover is removed and steel balls (density 7815 $\pm$ 50 kg/m^3) of different sizes are dropped with minimal ball rotation by switching off the electro-magnet. The velocity of the falling ball is calculated from the position *vs.* time data by time-differentiating the positions of the ball centroids using a central differential formula [29]. The error in velocity is estimated using the formula [30], $\delta V = \sqrt{\delta r_j^2 + \delta r_{j+1}^2}/\Delta t$, where j is the frame number and the uncertainty in position ($\delta r = \sqrt{\delta x^2 + \delta y^2}$) is the fitting error in estimating the mean of the intensity profile of the ball along the y and x

directions (direction of the fall of the ball and the direction perpendicular to it, i.e., parallel to the plane of the camera, respectively) using the Gaussian function. The time interval, Δt, is calculated from the frame rate of the camera. The data is fitted to a mathematical model using Jupyter notebook (Python v3.7). Experiments are performed using Newtonian fluids of viscosities comparable to those of the Laponite suspensions used here. The effects of the viscometer wall [31, 32] and Reynolds number on the motion of the falling ball have been estimated from these experiments (calibrations for drag and wall effects are also discussed in section 2.2.2). The effects of the wall are found to be negligible in these measurements.

For rheological measurements [33, 34], a stress controlled Anton Paar MCR-501 rheometer is used. The temperature is fixed at 25°C using a water circulation system. A double gap geometry (DG - 26.7, outer diameter = 13.796 mm, inner diameter = 11.915 mm, cell height = 42 mm, sample volume = 3.8 ml) is used for our experiments as discussed in section 2.2.1 of Chapter 2. Aqueous suspensions of dried Laponite of concentration 2.8 % w/v are stirred for 1 hr at 400 rpm to break up big particle clusters. For each experimental run, the sample is loaded slowly into the annular region of the geometry using a syringe. Silicone oil of viscosity 5 cSt is used as solvent trap oil to minimize sample evaporation. A shear rate of 500 sec^{-1} is applied for 5 minutes to break any remaining particle clusters. This procedure ensures an identical initial state and is essential for the acquisition of reproducible data. A low shear (1 sec^{-1}) is applied for subsequent data acquisition and a freshly prepared sample is allowed to age spontaneously in the rheometer geometry upto a predetermined t_w before the start of each measurement.

3.3 Results

3.3.1 Time dependence of viscosity

As discussed earlier, the time-dependent evolution of inter-particle screened repulsive forces in Laponite suspensions gives rise to a gradual and continuous micro-

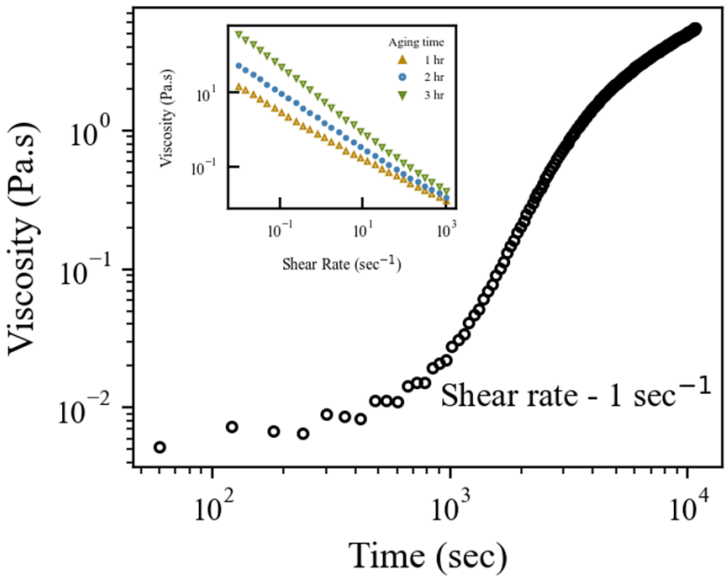

Figure 3.1: The time evolution of viscosity of a Laponite suspension (concentration 2.8% w/v). In the inset, viscosity is plotted with shear rate for 2.8% w/v Laponite suspensions at different aging times (t_w = 1, 2, 3 hrs). While the time-evolution of viscosity in the main figure was acquired for a single sample, the data in the inset was acquired on fresh samples aged to 1 hr, 2 hrs and 3 hrs respectively.

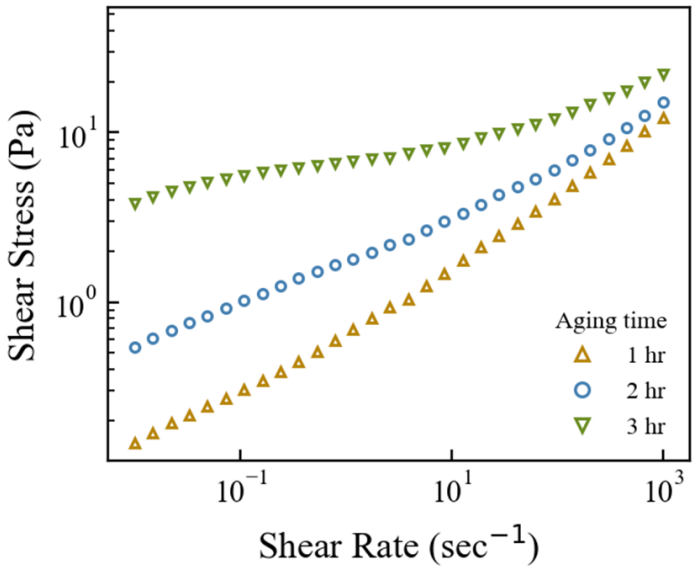

Figure 3.2: Shear stress is measured by varying shear rate for different aging times of 2.8% w/v Laponite suspensions using a rheometer. Fresh samples were used in each of the 3 experiments. The corresponding viscosity vs. shear rate data is plotted in the inset of Fig.3.1.

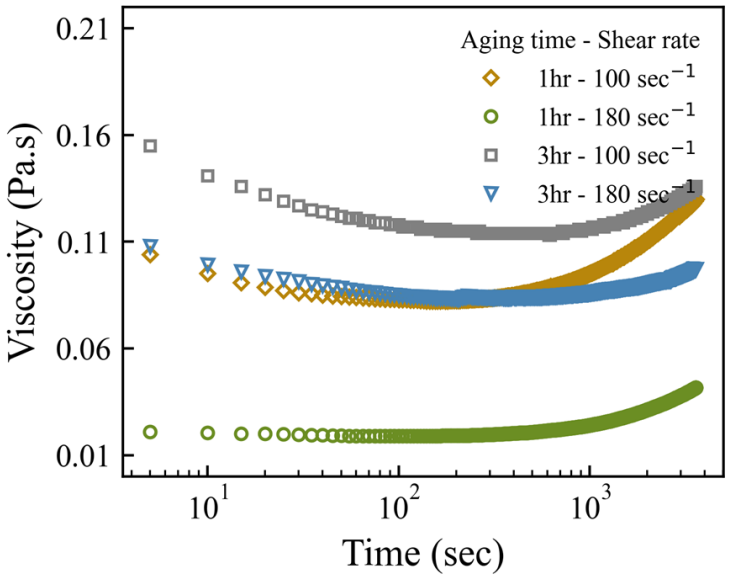

Figure 3.3: Time dependent viscosity of 2.8% w/v Laponite suspensions, of aging times t_w = 1 hr and 3 hr, subjected to constant shear rates of 100 and 180 sec^{-1} at 25°C.

structural build-up. Consequently, Laponite suspensions show physical aging which manifests in experiments as a spontaneous evolution of the viscoelastic moduli. In Fig.3.1, the viscosity of a 2.8% w/v freshly prepared Laponite suspension, recorded with time under a low shear rate (1 sec^{-1}) for 3 hr, is displayed. The viscosity is seen to spontaneously increase with time, signalling the progress of the physical aging phenomenon. To study the relation between shear stress and shear rate, a fresh sample is used in each experiment and a low shear rate is applied continuously during the aging process. After reaching the desired duration of aging i.e. 1, 2 or 3 hrs, a ramp of shear rate is applied to the aged sample. The shear rate dependent viscosities of Laponite suspensions of aging times t_w = 1,2,3 hours are plotted in the inset of Fig.3.1.As expected [35], the viscosity decreases with shear rate for all sample aging times explored here. The shear stress vs. shear rate plots for Laponite suspensions at ages t_w = 1,2,3 hrs are shown in Fig.3.2. Time-dependent changes in the viscosity of Laponite suspensions are measured for two different shear rates 100 and 180 sec^{-1} and are plotted in Fig.3.3. It is seen from this figure that the imposition of constant shear rates results in a decrease in the suspension viscosity at earlier

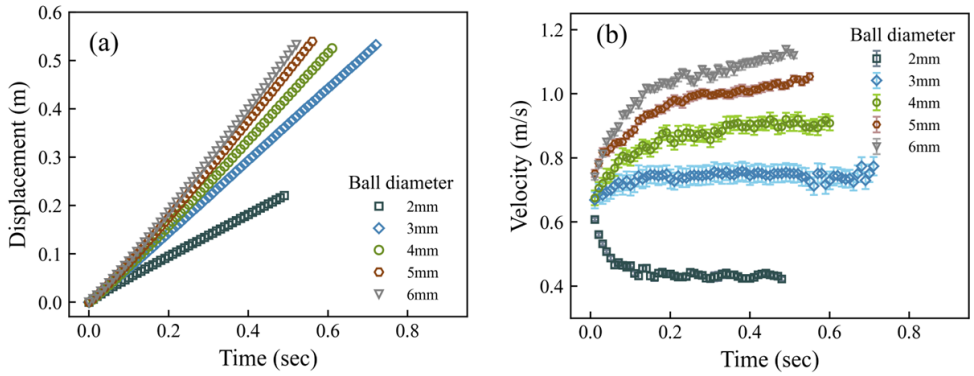

Figure 3.4: (a) Displacement *vs.* time of the steel balls (diameter = 2, 3, 4, 5, 6 mm) falling through Laponite suspensions of concentration 2.8% w/v at 1 hr aging time (t_w). (b) Velocity *vs.* time is calculated from the displacement data in (a). The error bars are calculated using the protocol specified for balls falling in a medium [30].

times. This observation can be attributed to the breakup of sample microstructures by the high shear rates that are imposed in these experiments. At longer times, the viscosity shows an increase due to the increased rate of structural recovery. These competing effects give rise to a non-monotonic viscosity profile that is sensitive to sample age and the imposed shear rate.

3.3.2 Falling ball experiments

The experiments reported here track millimeter-sized steel balls falling through spontaneously evolving Laponite suspensions. Freshly prepared Laponite suspensions that are allowed to age for t_w =1,2,3 hrs are used. The viscosity of the suspension increases gradually due to the physical aging mechanism discussed earlier. A ball that is dropped through an aging viscoelastic suspension is expected to induce shear thinning of the medium due to break up of the fragile structures present in its path. For all the experiments reported here, Laponite suspension concentration is kept fixed at 2.8% w/v.

The extent of shear thinning of the surrounding medium due to passage of the ball can be evaluated approximately by relating it to the data plotted in Fig.3.3. The shear rate imposed by the ball is estimated using the relation $\dot{\gamma} = V/D$, where

V and D are, respectively, the instantaneous velocity and the diameter of the falling ball. For the velocities of the falling balls, V, measured here and the diameters, D, of all the balls used, the shear rates imposed by the balls always lie within the range 100-200 sec^{-1} in our experiments. A comparison with Fig.3.3 shows that the aging Laponite samples lie in the shear-thinning regime within this range of shear rates. A ball falling through a Laponite suspension would therefore disintegrate the local structures in its path.

Fig.3.4 shows representative data when balls are dropped in a Laponite suspension that has been aged for 1 hr. In Fig.3.4(a), the displacements of balls having different diameters (2mm, 3mm, 4mm, 5mm and 6mm) are plotted. The overall slopes of the displacement curves tend to decrease with decreasing ball diameters. The velocities are plotted *vs.* time for different ball sizes in Fig.3.4(b). As expected, the larger balls with higher inertia travel with greater velocities through the Laponite suspension medium. The ball of diameter 2mm, released at a high non-zero initial velocity, eventually reaches a lower terminal velocity. In contrast, the velocities of the balls of diameters 3-6 mm increase continuously with time throughout our experimental time window, with the increase becoming more prominent for the larger balls. Error in velocity due to tracking is calculated [30] and plotted with vertical bars.

Data for all the ball-drop experiments, acquired for balls of sizes between 2 mm and 6 mm falling through Laponite suspensions of different ages, are plotted in Fig.3.5. We observe from Fig.3.5(a) that the velocity of the 2 mm ball decays with time and attains a steady state terminal velocity during the experimental time window for all Laponite suspensions at aging times, t_w= 1 hr, 1.5 hr, 2.5 hr. For all the Laponite aging times investigated here, the velocities of the balls of larger diameters (3mm, 5mm and 6mm) continue to increase during the experimental time window, with the increase being maximum for the largest ball (Figs.3.5(b-d)). Such continuous increase in velocity without attainment of terminal velocity in the experimental time window accessible in our experiments indicates the prevalence

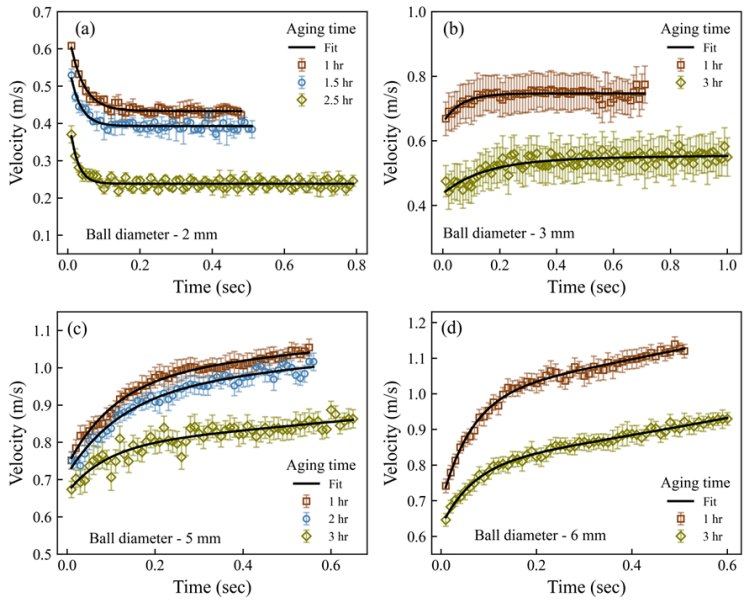

Figure 3.5: In (a), (b), (c) and (d), velocities of the ball centroids for balls of diameters 2mm , 3mm , 5mm and 6mm respectively, falling through Laponite suspensions of different aging times (t_w), are plotted. Coloured symbols represent experimental data, coloured vertical bars are the corresponding error bars [30] and continuous black lines are the fits to Eqn.3.7.

of medium destructuring over structural recovery under these conditions. As the sample age increases, the ball velocity decreases in all the experiments. Vertical bars with lighter shades of the symbol colours are plotted to represent the errors in Fig.3.5.

3.3.3 Mathematical model

Moore (1959) [28] proposed a mathematical model to explain the micro-structural evolution of thixotropic materials. In this model, the time-dependent structure of an aging fluid is represented by a dimensionless structural parameter, λ. This model incorporates λ with the following physical interpretation: $\lambda = 0$ for a fully broken or destructured state of the fluid (or when the structure is yet to form at the microscopic level), while $\lambda = 1$ for a fully structured fluid state, i.e., when the structure is not broken at all.

In an aging Laponite suspension that is locally destructured by a ball falling

through it, the time evolution of the structural parameter, λ, has to be governed by restructuring/structural recovery and destructuring/structural breakdown of the suspension,

$$\frac{d\lambda}{dt} = F(\lambda) - G(\lambda, \dot{\gamma}) \tag{3.2}$$

In the above equation, $F(\lambda)$ and $G(\lambda, \dot{\gamma})$ are associated with the rates of the restructuring and destructuring processes that progress simultaneously in a Laponite suspension having an instantaneous state λ. Eqn.3.2 can be simplified by considering a constant restructuring rate $F = 1/\theta$ and a destructuring function $G = \alpha\lambda\dot{\gamma}$ that varies linearly with local shear rate [36, 37], i.e., $d\lambda/dt = 1/\theta - \alpha\lambda\dot{\gamma}$. Here, $\dot{\gamma}$ is the shear rate imposed by the falling ball and $1/\theta$ and α are parameters related to the restructuring and destructuring rates of the medium respectively.

The restructuring rate of the Laponite suspension is decided by its physical properties such as aging time, concentration and instantaneous state. As the Laponite suspension ages with time, the structure evolves identically throughout the medium. In the present scenario, since the structural length scales of interest are much larger than the size of a single Laponite particle, the viscosity can be assumed to be equal at all points in the undisturbed sample. The high shear rates of approximately 100-200 sec^{-1} experienced by the regions in the immediate neighbourhood of the falling ball are expected to result in shear thinning of the surrounding Laponite medium due to the breakdown of the fragile microscopic structures. This can be seen in Fig.3.3 where we note that structural recovery takes over only after 1000 seconds when suspensions are subjected to these high shear rates. The time of fall of the ball is less than 1 second and therefore smaller than the time scale over which the structural parameter is expected to change due to the physical aging process. The destructuring due to the passage of the ball is expected to dominate over the restructuring process and $F(\lambda)$ in Eqn.3.2 can be neglected. To model the destructuring of the medium in our falling ball experiments, we make the following assumptions:

i) The ball falls inside the sample while shearing only the immediate vicinity of

its surface. During the passage of the ball, it interacts with each point in the medium that lies in its path. Therefore the time evolution of the structural parameter of the medium, $d\lambda_f/dt$, should be proportional to the time taken by the ball to travel its diameter, D/V.

ii) As higher ball velocity causes increased disruption in the structure of the medium surrounding the ball, the time evolution of the structural parameter is assumed proportional to the instantaneous ball velocity, V, during the fall.

We can therefore simplify Eqn.3.2 and propose the following modified kinetic equation for the time-dependent structural evolution in Laponite suspensions,

$$\frac{d\lambda_f}{dt} \propto -V\frac{D}{V} \tag{3.3}$$

In Eqn.3.3, the time dependent structural parameter of the aging Laponite suspension for falling ball experiments is denoted by λ_f. The negative sign is incorporated to account for shear-thinning due to disruption of the fragile suspension structures by the falling ball. Eqn.3.3 reduces to:

$$\frac{d\lambda_f}{dt} = -\epsilon D \tag{3.4}$$

$$\implies \lambda_f = \lambda_0(1-\beta t) \tag{3.5}$$

where ϵ is a proportionality constant of dimension (length $\times$ time)$^{-1}$, $\lambda_f = \lambda_0$ at time $t = 0$ and the rate of destructuring is $\beta = \epsilon D/\lambda_0$. The viscoelastic, structured nature of the suspension can be incorporated in the expression for terminal velocity, V_{ter} obtained from Eqn.3.1, by considering the functional form [38] for viscosity $\eta = \eta_0\lambda_f^n$ where η_0 is the zero-shear viscosity and $n = 1$ for a Laponite suspension [36]. Viscosity of the suspension at each point changes with its structural parameter. The expression for the structure dependent terminal velocity, V_λ, of the ball falling

through a thixotropic Laponite suspension can therefore be written as:

$$\begin{aligned} V_\lambda(t) &= \frac{(\rho_s - \rho)gD^2}{18\eta(t)} \\ &= \frac{(\rho_s - \rho)gD^2}{18\eta_0\lambda_0(1-\beta t)} \end{aligned} \tag{3.6}$$

Here, we have used Eqn.3.5 and the expression for viscosity of Laponite suspensions [38] to obtain the expression for instantaneous viscosity, $\eta(t) = \eta_0\lambda_0(1-\beta t)$. Using Eqns.3.1 and 3.6, we rewrite the equation of motion of a ball falling through a thixotropic suspension with an initial velocity V_0:

$$\begin{aligned} V &= V_\lambda + (V_0 - V_\lambda)\exp(-t/\tau) \\ &= \frac{W}{(1-\beta t)} + (V_0 - \frac{W}{(1-\beta t)})\exp(-t/\tau) \end{aligned} \tag{3.7}$$

where $W = (\rho_s - \rho)gD^2/18\eta_0\lambda_0$, β, V_0, τ are the fitting parameters. Here, $\tau = m/3\pi\lambda_0\eta_0 D$ where m = mass of the ball, η_0 = zero-shear viscosity of the sample, D = diameter of the ball.

The constant breakdown of the micro-structure as the ball falls through the suspension leads to shear thinning at a rate parametrized by β in Eqn.3.5. Naturally, for a Newtonian sample, we expect the value of β to be zero. The data for balls of different sizes falling through Laponite suspensions of different aging times (Figs.3.5(a-d)) are fitted to Eqn.3.7 (solid lines in Fig.3.5) and the destructuring rate, β, is obtained as one of the fitting parameters. All the fitting parameters are tabulated in Table 3.1. In Fig.3.6, β is plotted for ball sizes between 2 mm - 6 mm for different aging times. This suggests that balls with larger diameters exhibit faster dynamics leading to enhanced shear thinning of the sample. Only the fitting errors are considered in this plot. It is clear from the figure that β decreases with ball size and is approximately zero for the smallest ball of diameter 2 mm studied here. When larger balls are dropped through Laponite suspensions, the destructuring rates increase with ball size and stay nearly unchanged over the entire

range of sample ages. The approximate insensitivity of β to changes in sample age t_w arises from the predominance of destructuring processes over structural recovery in the freshly prepared Laponite suspensions used here. Our assumption that shear thinning of the medium dominates over structural recovery in our falling ball experiments is therefore adequate to accurately compute the ball trajectories. Furthermore, Eqn.3.7 explains our experimental data irrespective of the instantaneous state of the suspension.

We note here that the toy model used here is oversimplified and needs to be improved to include details of the system more effectively. For example, β is considered to be completely independent of the system properties. Unfortunately, it is not possible to measure all the parameters contributing to β separately and precisely. Neither is it possible to accurately estimate λ_0 for real experimental system. Our model also considers that the viscosity of water approaches zero when the suspension is completely destructured. Since we observe that viscosity increases with aging time, surpassing that of water significantly at larger aging times (3.1), we have neglected the viscosity of water since it is 2 orders of magnitude smaller than that of the Laponite medium. Additionally, we would like to point out other limitations of this model. The model only holds for the narrow regime that is explored experimentally. The dimension of β is system dependent and measures the rate of change of structure parameter with time. The exact details of the initial state could not be incorporated in the model due to computational constraints. Furthermore, the asymptotic behaviour of the ball cannot be predicted due to the several simplified assumptions that are inherent in our toy model.

3.4 Conclusions

The destructuring of a Laponite suspension due to a ball falling through it is studied in this work. We show that the motion of solid steel balls through spontaneously evolving colloidal suspensions of Laponite is very different from the motion of a solid

Table 3.1: Parameters measured by fitting Eqn.3.7 to the data in Fig.3.5.

D (mm)	t_w (hr)	V_0 (m/s)	W (m/s)	$1/\tau$ (s^{-1})	β (s^{-1})
2	1	0.653 ± 0.010	0.433 ± 0.004	26.077 ± 2.255	1.07e-17 ± 0.031
2	1.5	0.570 ± 0.019	0.392 ± 0.005	33.232 ± 5.245	1.64e-19 ± 0.037
2	2.5	0.439 ± 0.024	0.238 ± 0.003	45.801 ± 6.843	7.79e-16 ± 0.026
3	1	0.655 ± 0.011	0.747 ± 0.006	16.033 ± 3.814	1.11e-15 ± 0.011
3	3	0.436 ± 0.010	0.543 ± 0.013	6.819 ± 2.001	0.017 ± 0.030
4	1	0.661 ± 0.009	0.876 ± 0.013	10.882 ± 1.499	0.066 ± 0.029
5	1	0.736 ± 0.007	0.982 ± 0.016	9.374 ± 1.130	0.105 ± 0.031
5	2	0.713 ± 0.009	0.947 ± 0.029	8.208 ± 1.719	0.103 ± 0.053
5	3	0.664 ± 0.014	0.793 ± 0.015	11.757 ± 3.456	0.119 ± 0.034
6	1	0.691 ± 0.010	1.001 ± 0.008	16.261 ± 1.206	0.218 ± 0.018
6	3	0.627 ± 0.006	0.802 ± 0.004	15.872 ± 1.242	0.232 ± 0.010

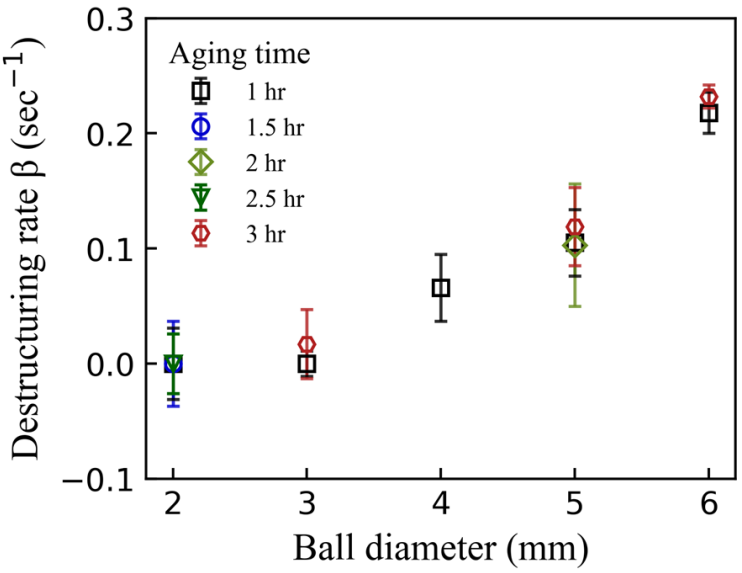

Figure 3.6: Destructuring rate, β, *vs.* ball diameter, D, is plotted for different aging times (t_w) of Laponite suspensions.

object in a Newtonian fluid.

Falling ball experiments are performed by dropping millimeter-sized balls in Laponite suspensions of different ages. In contrast to a ball falling through a Newtonian fluid, we find that the larger balls do not attain a steady state while falling through Laponite suspensions during the experimental time window. By modifying a mathematical model proposed by Moore [28] to account for balls falling over time scales much faster than the suspension aging times, we successfully extract the destructuring rates of Laponite suspensions of different ages for different ball sizes. Interestingly, the gradual increase of velocity within the experimental time window accessible in these measurements can also be explained using this model. Eventually at later times and for longer viscometer heights, the ball would have certainly reached a steady state. The restructuring contribution in Eqn.3.2 that we have neglected for the present measurements would then be non-negligible. However, trying to observe the motion of the ball till it reaches a steady state would require us to perform experiments with much longer cylinders and enormous sample volumes. We have therefore restricted our study by exploring the motion of the falling ball in a

regime that can be described by the simplest mathematical model that quantifies the gradual increase of ball velocity due to shear thinning of the Lapaonite suspensions. Further, the initial velocity of the ball when it enters the medium is non-zero as the ball is released from a fixed height above the fluid surface. Further experiments need to be performed to determine the effect of initial velocity on the destructuring rate of the suspension.

Our results are fairly general and are applicable in the study of the settling dynamics of macroscopic objects in a wide variety of thixotropic suspensions. Balls of different materials can be used to explore microscopic viscosities and destructuring rates of complex fluids over a large range of shear rates. We note here that while the viscosity measured by a rheometer reflects the response of the entire sample, falling ball viscometry explores the viscosity of the medium only in the neighbourhood of the falling ball. We have parametrized the destructuring rate of the Laponite suspension medium in terms of a parameter β. Rheometry and falling ball viscometry probe the system differently, involve very different shear profiles, and are complementary to each other. A quantitative relation between β and bulk viscosity of a non-Newtonian fluid obtained in rheological measurements is therefore well outside the scope of this discussion.

To conclude, falling ball viscometry, which involves the macroscopic measurement of the velocity of a ball falling through a medium, can be employed to successfully estimate the microscopic dynamics of fragile structures in shear thinning suspensions. The experiments reported in this chapter provide important insights into the physical aging process in the presence of externally-imposed forces and contribute to our understanding of the motion of macroscopic objects through non-Newtonian fluids.

Bibliography

[1] George Gabriel Stokes et al. On the effect of the internal friction of fluids on the motion of pendulums. 1851.

[2] J M Coulson, J F Richardson, J H Harker, and J R Backhurst. *Coulson and Richardson's Chemical Engineering*. Pergamon Press, 2002.

[3] Phillip P Brown and Desmond F Lawler. Sphere drag and settling velocity revisited. *Journal of Environmental Engineering*, 129(3):222–231, 2003.

[4] Walter RA Goossens. Review of the empirical correlations for the drag coefficient of rigid spheres. *Powder Technology*, 352:350–359, 2019.

[5] AR Khan and JF Richardson. The resistance to motion of a solid sphere in a fluid. *Chemical Engineering Communications*, 62(1-6):135–150, 1987.

[6] FX Hart and CA Little III. Student investigation of models for the drag force. *American Journal of Physics*, 44(9):872–878, 1976.

[7] Blandine Gueslin, Laurence Talini, Benjamin Herzhaft, Yannick Peysson, and Catherine Allain. Flow induced by a sphere settling in an aging yield-stress fluid. *Physics of Fluids*, 18(10), 2006.

[8] JB Freund, J Kim, and RH Ewoldt. Field sensitivity of flow predictions to rheological parameters. *Journal of Non-Newtonian Fluid Mechanics*, 257:71–82, 2018.

[9] Murat Guvendiren, Hoang D Lu, and Jason A Burdick. Shear-thinning hydrogels for biomedical applications. *Soft matter*, 8(2):260–272, 2012.

[10] Abdoulaye Fall, Jose Paredes, and Daniel Bonn. Yielding and shear banding in soft glassy materials. *Physical Review Letters*, 105(22):225502, 2010.

[11] CF Chan Man Fong, G Turcotte, and D De Kee. Modelling steady and transient rheological properties. *Journal of Food Engineering*, 27(1):63–70, 1996.

[12] Konstantinos Giannokostas, Pantelis Moschopoulos, Stylianos Varchanis, Yannis Dimakopoulos, and John Tsamopoulos. Advanced constitutive modeling of the thixotropic elasto-visco-plastic behavior of blood: Description of the model and rheological predictions. *Materials*, 13(18):4184, 2020.

[13] Casey C Clark, Julio Aleman, Lysette Mutkus, and Aleksander Skardal. A mechanically robust thixotropic collagen and hyaluronic acid bioink supplemented with gelatin nanoparticles. *Bioprinting*, 16:e00058, 2019.

[14] Yingxin Liu, Shengjie Ling, Suhang Wang, Xin Chen, and Zhengzhong Shao. Thixotropic silk nanofibril-based hydrogel with extracellular matrix-like structure. *Biomaterials Science*, 2(10):1338–1342, 2014.

[15] Raj P Chhabra. *Bubbles, drops, and particles in non-Newtonian fluids*. CRC press, 2006.

[16] Guanzheng Zhuang, Zepeng Zhang, and Maguy Jaber. Organoclays used as colloidal and rheological additives in oil-based drilling fluids: An overview. *Applied Clay Science*, 177:63–81, 2019.

[17] Magdalena M Mrokowska and Anna Krztoń-Maziopa. Viscoelastic and shear-thinning effects of aqueous exopolymer solution on disk and sphere settling. *Scientific Reports*, 9(1):7897, 2019.

[18] H Tabuteau, FK Oppong, JR De Bruyn, and P Coussot. Drag on a sphere moving through an aging system. *Europhysics Letters*, 78(6):68007, 2007.

[19] Anandhan Jayaraman and Andrew Belmonte. Oscillations of a solid sphere falling through a wormlike micellar fluid. *Physical Review E*, 67(6):065301, 2003.

[20] Nitin Kumar, Sayantan Majumdar, Aditya Sood, Rama Govindarajan, Sriram Ramaswamy, and AK Sood. Oscillatory settling in wormlike-micelle solutions: bursts and a long time scale. *Soft Matter*, 8(16):4310–4313, 2012.

[21] Nestor Z Handzy and Andrew Belmonte. Oscillatory rise of bubbles in wormlike micellar fluids with different microstructures. *Physical Review Letters*, 92(12):124501, 2004.

[22] Brian J Briscoe, Mathias Glaese, Paul F Luckham, and Shaoran Ren. The falling of spheres through bingham fluids. *Colloids and Surfaces*, 65(1):69–75, 1992.

[23] A Shahin and Yogesh M Joshi. Irreversible aging dynamics and generic phase behavior of aqueous suspensions of laponite. *Langmuir*, 26(6):4219–4225, 2010.

[24] Roberta Angelini, Laura Zulian, Andrei Fluerasu, Anders Madsen, Giancarlo Ruocco, and Barbara Ruzicka. Dichotomic aging behaviour in a colloidal glass. *Soft Matter*, 9(46):10955–10959, 2013.

[25] Mina Fazilati, Nahid Maleki-Jirsaraei, Shahin Rouhani, and Daniel Bonn. Quasi-periodic and irregular motion of a solid sphere falling through a thixotropic yield-stress fluid. *Applied Physics Express*, 10(11):117301, 2017.

[26] Peder CF Møller, Jan Mewis, and Daniel Bonn. Yield stress and thixotropy: on the difficulty of measuring yield stresses in practice. *Soft matter*, 2(4):274–283, 2006.

[27] AMV Putz, TI Burghelea, IA Frigaard, and DM Martinez. Settling of an isolated spherical particle in a yield stress shear thinning fluid. *Physics of Fluids*, 20(3), 2008.

[28] F Moore. The rheology of ceramic slips and bodies. *Transactions of the British Ceramic Society*, 58:470, 1995.

[29] Alejandro L Garcia. *Numerical methods for physics*. Prentice Hall Englewood Cliffs, NJ, 2000.

[30] Yan Feng, John Goree, and Bin Liu. Errors in particle tracking velocimetry with high-speed cameras. *Review of Scientific Instruments*, 82(5), 2011.

[31] Ralf Kehlenbeck and Renzo Di Felice. Empirical relationships for the terminal settling velocity of spheres in cylindrical columns. *Chemical Engineering & Technology: Industrial Chemistry-Plant Equipment-Process Engineering-Biotechnology*, 22(4):303–308, 1999.

[32] RP Chhabra, S Agarwal, and K Chaudhary. A note on wall effect on the terminal falling velocity of a sphere in quiescent newtonian media in cylindrical tubes. *Powder Technology*, 129(1-3):53–58, 2003.

[33] Christopher W Macosko. *Rheology: Principles, Measurements, and Applications*. Wiley, 1994.

[34] Randy H Ewoldt, Michael T Johnston, and Lucas M Caretta. Experimental challenges of shear rheology: How to avoid bad data. *Complex Fluids in Biological Systems: Experiment, Theory, and Computation*, pages 207–241, 2015.

[35] B Gueslin, L Talini, and Y Peysson. Sphere settling in an aging yield stress fluid: link between the induced flows and the rheological behavior. *Rheologica Acta*, 48:961–970, 2009.

[36] T Ferroir, HT Huynh, Xavier Chateau, and Philippe Coussot. Motion of a solid object through a pasty (thixotropic) fluid. *Physics of Fluids*, 16(3):594–601, 2004.

[37] Erik A Toorman. Modelling the thixotropic behaviour of dense cohesive sediment suspensions. *Rheologica Acta*, 36:56–65, 1997.

[38] MM Gumulya, RR Horsley, and Vishnu Pareek. Numerical simulation of the settling behaviour of particles in thixotropic fluids. *Physics of Fluids*, 26(2), 2014.

Chapter 4

Correlating microscopic viscoelasticity and structure of an aging colloidal gel using active microrheology and cryo-FESEM

4.1 Introduction

As a result of the pioneering work of Arthur Ashkin and coworkers [1], optical tweezers (OTs) have become an invaluable tool for studying various processes in physical and biological systems [2–7]. An OT utilizes the forces exerted by a focused laser beam to confine a micron-sized dielectric particle suspended in a medium [8]. It can operate as a non-invasive force transducer, which can accurately produce and measure pico-Newton (pN) range forces and nanometer (nm) range displacements with high temporal resolution (down to a few μs) [9, 10]. Their utility as a single molecule manipulation technique makes OTs an important resource for investigating various processes, such as in quantifying the kinetics of kinesin motors walking on microtubules [2], in unzipping of DNA [3], in cell sorting [4], and in measuring the mechanical responses of soft materials, such as colloidal suspensions [11, 12],

polymer networks [5, 6] and bio-samples [7].

The study of the flow and deformation of materials and the determination of their mechanical properties is known as rheology [13]. Conventional viscometers and rheometers can measure mechanical properties of a material even with sample volumes less than a milliliter [14]. Passive microrheology requires a much smaller sample volume and can measure linear viscoelastic responses in a broad frequency domain by tracking the thermal motion of a probe particle suspended in the medium [15]. This technique uses the generalized Stokes-Einstein relation to connect the mean square displacement (MSD) of the probe particle with the viscoelastic properties of the medium [16, 17]. Video particle tracking microrheology [18], dynamic light scattering [19], magnetic tweezers [20] and optical tweezers [21] have been used successfully to study the viscoelastic properties of a range of materials. Passive microrheology provides useful information on local micro-structures of the material and has been used to probe spatial heterogeneities and non-ergodicity in the suspending medium [22].

The measured microrheological properties of viscoelastic materials depend on the size of the trapped probe particle [23–25]. The surface chemistry of the probe particle and its interaction with the medium also influence the measurement [24, 25]. Valentine *et al.* [24] showed that in the absence of interactions between the probe and viscoelastic medium, a probe size larger than the characteristic lengthscale relevant to the viscoelastic medium is necessary to interpret the results accurately. Interestingly, the authors also noted that elasticity of the viscoelastic matrix, which arises due to the presence of suspension microstructures, can be measured using a relatively smaller probe particle in the presence of significant probe-medium interactions. Owing to the smaller sizes of the probe particles in this last case, the measurements are not sensitive to the spatial heterogeneity present in the viscoelastic medium.

He *et al.* [25] showed that surface adsorption on a probe particle embedded in a network of actin filaments results in an enhanced estimate for the stiffness of

the biopolymer network. An earlier work had proposed a scheme to study colloidal forces, structure, dynamics and rheology of attractive colloidal gels by combining microscopy, OT and rheology [26]. Passive microrheology becomes less effective with highly viscous or gel-like samples due to reduced motion of the probe particle, and a simultaneous reduction in the signal-to-noise ratio [27]. In such cases, active microrheology can be used, wherein an external force is applied to the probe particle and its resultant motion is measured to determine the viscoelastic properties of the surrounding matrix. Optical tweezers [21], magnetic tweezers [28] and atomic force microscopy [29] are the most commonly used active microrheology techniques. Active microrheology with optical tweezers can be implemented using two methods, *viz.*, oscillatory measurements and creep measurements [5]. In oscillatory measurements, the sample stage is moved in an oscillatory fashion, and the resultant force experienced by the trapped probe particle is computed. The amplitudes of the two signals and the phase difference between them are analyzed to determine the viscoelastic properties of the medium [5]. On the other hand, in creep measurements, a constant stress is applied to the medium by displacing the probe particle, following which the response of the material is measured. The oscillatory active microrheology technique is more closely related to conventional bulk rheology as its output is in the form of the frequency-dependent storage and loss moduli, G' and G'' respectively, of the sample [5].

Aqueous suspensions of Laponite have been widely used as model systems to probe the properties of non-ergodic states such as gels and glasses [30]. As mentioned in previous chapters, Laponite particles exist in a stacked powder form and undergo exfoliation upon adding it to water. This exfoliation process results in the release of Na^+ ions. These ions serve to electrostatically shield the negatively charged Laponite particles. However, when the concentration of counterions increases, the Debye length decreases [31]. This reduction in Debye length leads to an enhancement in the rate of formation of house of cards suspension structures. We have shown in the last chapter that falling ball viscometry can be used success-

fully to quantify the shear thinning property of a freshly prepared Laponite sample in terms of the destructuring rate of the suspension [32]. The time-dependent aging behaviour of soft colloidal glasses and their dependence on the physicochemical properties of the suspension have been studied extensively using macroscopic rheology and passive microrheology [11, 12, 23, 33, 34]. There are a few reports on the passive microrheology of soft glassy clay suspensions that validate the fluctuation-dissipation theorem in non-equilibrium systems [11, 12, 33]. Another passive microrheology study of Laponite suspensions reported that microscopic mechanical properties approach those extracted from bulk rheology measurements as the size of the embedded probe is increased [23], with the viscoelastic liquid to soft solid transition occurring earlier at the bulk scale than at the microscopic scale [34]. However, to the best of our knowledge, oscillatory active microrheology has never been performed to study the length-scale dependent mechanical response of aging aqueous Laponite clay suspensions. The falling ball experiments in Chapter 3 reported the destructuring of Laponite structures as a ball falls through Laponite suspension. A limitation of this experiment is that the ball can probe a specific region in the system for a very short time while disrupting the suspension structures that it encounters in its path. This chapter reports OT-based microrheology experiments, wherein we trap colloidal particles in a shear cell loaded with an aging Laponite suspension. Since the forces exerted on the suspension by the trapped bead are many orders of magnitude smaller when compared to the forces exerted by the ball in Chapter 3, OT-based microrheology results such as those presented in the present chapter give complementary results related to the suspension mechanical properties without destructing the system. In these OT experiments therefore, it is much easier to probe the material for a longer time with better statistics.

In this chapter, we employ oscillatory active microrheology to investigate the mechanical properties of aqueous Laponite suspensions at various aging times t_w and concentrations C_L. We apply sinusoidal oscillations to the sample cell and measure the force experienced by an optically trapped probe particle that is physically

attached to the suspension microstructure network. The piezo-controlled stage is oscillated over a range of frequencies to determine the frequency-dependence of the elastic (G′) and viscous (G″) moduli of Laponite suspensions of different C_L and at various t_w. We observe that G″ dominates over G′ at smaller stage oscillation frequencies, ω, while G′ exceeds G″ when ω is increased beyond a crossover frequency, ω_{co}. The characteristic relaxation time τ of the suspension varies as the inverse of the crossover frequency, $\tau = 2\pi/\omega_{co}$. The crossover modulus G_{co} is the modulus value where G′ = G″. We report a systematic increase in G_{co} as the concentration of the suspension, C_L, is increased, thereby signaling the onset of a jamming transition. Furthermore, at a fixed C_L, we see that G_{co} increases with aging time t_w for the range of aging times explored here. We also investigate the length-scale dependence of G_{co} by varying the size of the probe particle. Cryogenic field emission scanning electron microscopy (cryo-FESEM) images of Laponite suspensions at various t_w and C_L reveal that the average pore diameters $\langle D_p \rangle$ of the underlying fragile suspension microstructures do not change significantly with t_w but decrease with increasing C_L, for the ranges of C_L and t_w explored here. Finally, we show that the crossover modulus G_{co} of the suspension is inversely related to the average diameter of the microscopic pores of the fragile suspension structures that evolve spontaneously and gradually due to the physical aging process for different Laponite concentrations and probe diameters.

4.2 Materials and Methods

The principle and calibration of optical tweezers are discussed in sections 1.4 and 2.2.4 of Chapters 1 and 2, respectively. The preparation of Laponite suspension is covered in section 2.1.1 of Chapter 2. Section 2.2.5 in Chapter 2 also contains a brief overview of cryo-FESEM.

4.3 Results and Discussion

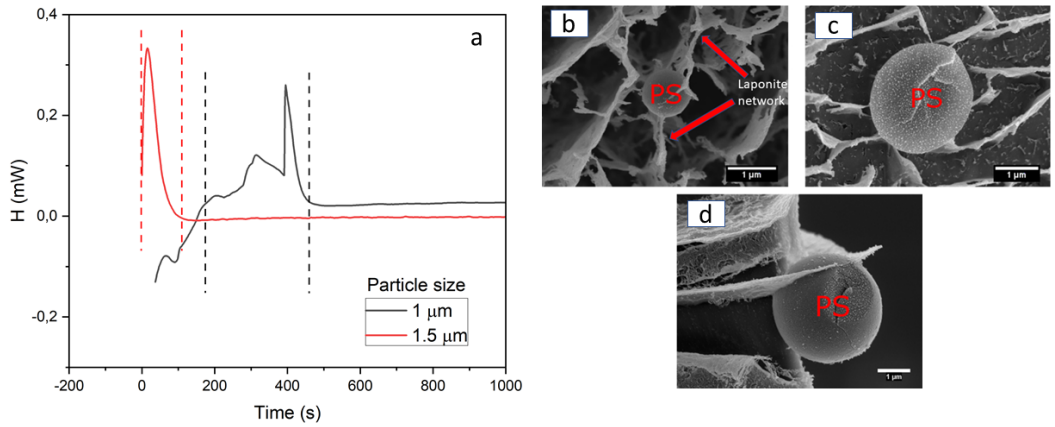

Figure 4.1: (a) Isotherm curve (relative heat released, H) for Laponite suspensions having polystyrene particles, when compared with pure Laponite suspension at 25°C temperature for two different particle sizes vs. measurement time. Polystyrene (PS) particles attached to the branches of the Laponite suspension networks (white connected regions) for particles of diameter (b) 1 μm (c) 1.5 μm and (d) 3.34 μm.

An aqueous Laponite suspension shows physical aging [35, 36], with the suspension viscoelasticity spontaneously increasing due to the gradual formation of medium-spanning self-assembled microstructures [37]. The microstructures can rupture or destructure under shear forces. When the shear is removed, these structures heal or restructure spontaneously. For our OT-based active microrheology experiments, we study the dynamics of polystyrene particles trapped in the Laponite medium. Information about interaction between the probe and Laponite suspension microstructures is necessary for interpretation of microrheology measurements [24, 25]. We perform isothermal calorimetry and cryogenic scanning electron microscopy images to visualize the extent of probe-Laponite attachment.

For the calorimetry experiments, freshly prepared Laponite suspensions with and without PS particles were loaded into two different measuring cells of the calorimeter. The peak observed in the figure represents the heat release in the suspension with PS particles when compared to the suspension without PS particles. The heat release results from bond formation between Laponite and PS particles. The energy

associated with this interaction is calculated by integrating the area under the peak (between the dashed lines in Fig.4.1(a)), and indicates an attractive force between the negatively charged PS particles and the positive rims of the Laponite particles. Isothermal calorimetry indicates an exothermic reaction ($\approx$ 350 and 560 mJ/g) which we attribute to the attachment of PS to Laponite network strands shown in Fig.4.1(a). This energy release is much higher than that estimated between Laponite particles due to attractive interactions ($\approx$ 200 mJ/g [23]) and confirms probe particle attachment to Laponite networks. Probe-Laponite attachment is further supported by the cryo-FESEM images in Fig.4.1(b-d) and can be explained by considering attachment of the positive rim of a Laponite particle to the negatively charged surface of a probe particle as schematically illustrated in Fig.4.2. Since the attachment of the probe particle with suspension microstructure obstructs its thermal motion, we choose to implement active microrheology to probe the Laponite system by applying an external force larger than the thermally induced fluctuations of the probe particle.

We perform active oscillatory microrheology [38] using optical tweezers (OT) to extract the elastic and viscous moduli, G′ and G″ respectively, of an aging Laponite clay suspension in the presence of a very low volume fraction (10^{-6} % v/v) of probe particles. The combination of high-accuracy position sensing of the probe using a quadrant photodiode (QPD) and highly sensitive measurements of displacements of the sample stage using piezoelectric actuators allow us to acquire data with micrometer precision. While the probe particle is optically trapped in the Laponite suspension, we oscillate the sample cell sinusoidally (Fig.4.3 top panel) along the x-axis with a maximum amplitude of 1 μm for a range of stage oscillation frequencies ω. The oscillatory movement of the sample stage results in a net oscillatory force experienced by the optically trapped probe, which is calculated by measuring its nanometer-scale oscillatory displacement. The displacement of the probe from the trap center, caused by the sinusoidal motion of the piezoelectric stage, is converted to the corresponding spring force using the trap stiffness calculated as discussed in

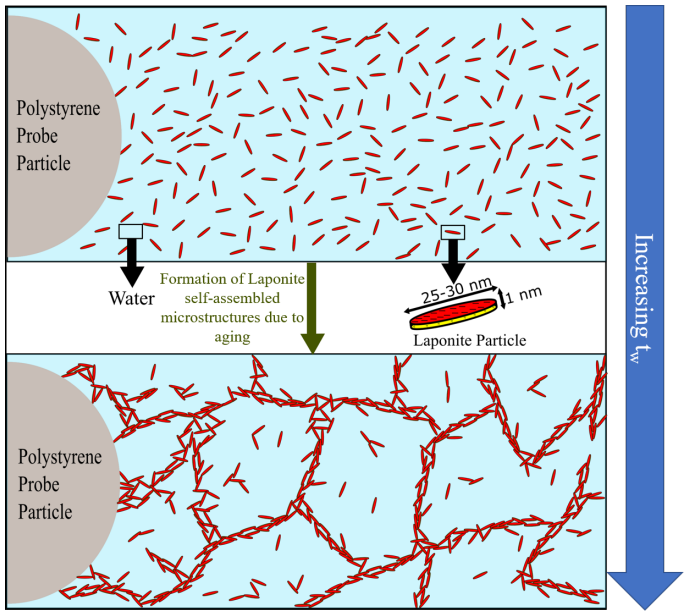

Figure 4.2: Schematic illustration showing the temporal evolution of Laponite microstructure in the presence of a polystyrene probe particle. Top panel: The probe particle attaches to the Laponite microstructure, with the number of contacts depending on particle size. Bottom panel: Individual Laponite particles self-assemble at higher aging times to form network structures through house of cards and overlapping coin assemblies.

section 2.2.4 of Chapter 2. The microscopic elastic and viscous moduli, G' and G'' respectively, of the underlying suspension are then calculated using the relations [38]:

$$G' = \frac{F_{max}}{6\pi R X_{max}} \cos(\Delta\phi), \tag{4.1}$$

$$G'' = \frac{F_{max}}{6\pi R X_{max}} \sin(\Delta\phi) \tag{4.2}$$

where F_{max} is the maximum force acting on the trapped particle, R is the radius of the trapped particle, X_{max} is the maximum amplitude of stage oscillation, and $\Delta\phi$ is the phase difference between the displacement of the sample stage and the force experienced by the trapped particle as shown in Fig.4.3.

We oscillate the sample stage at various frequencies ranging from $\approx$ 3 rad/s to 24 rad/s (0.47 - 3.81 s^{-1}), with the maximum oscillation frequency limited by the speed of data transfer during a given time interval. Simultaneously, the minimum oscillation frequency is set by the relative contributions of the viscous drag and

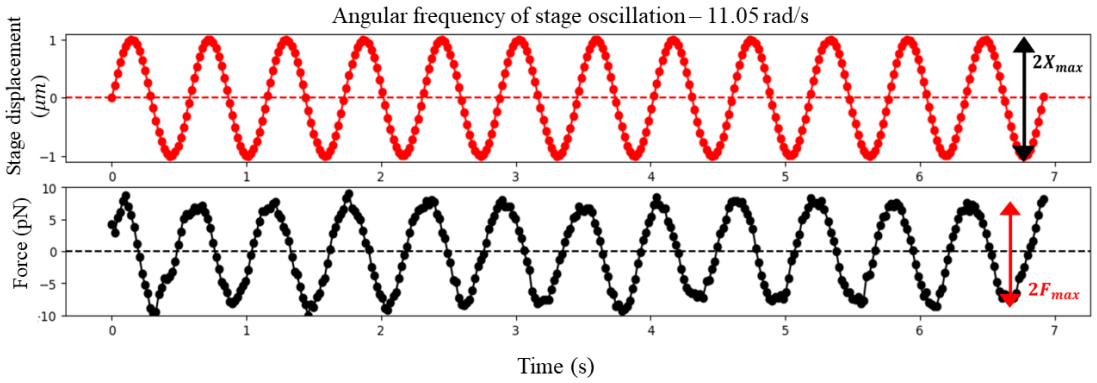

Figure 4.3: Sinusoidal displacement of the sample stage *vs.* time; Bottom: Force experienced by the trapped probe particle.

thermal forces acting on the trapped probe particle. The force experienced by the probe at a very small stage oscillation frequency produces very low signal to noise ratios. Therefore, below a certain frequency, acquisition of meaningful data acquisition is not possible. The data presented here is only for frequencies that are higher than this threshold value which depends on Laponite concentration C_L and aging time t_w. We oscillate the stage with a fixed amplitude and measure the oscillatory drag force and phase difference at a fixed frequency. We estimate the elastic and viscous moduli, G' and G'', of the Laponite suspension by repeating stage oscillations at each frequency for 12 cycles to ensure adequate statistics. We note here that since all the measurements were performed for Laponite ages t_w ranging from 90 to 150 minutes, the evolution of the viscoelastic moduli during the data acquisition interval of 5 minutes is expected to be minimal. The above range of aging times is chosen to ensure that the viscosity contribution of the underlying medium causes a measurable displacement of the trapped bead, while still localizing it within the optical trap. We present below the key results of our active microrheology experiments and a discussion on error calculation.

Error calculation: For each measurement, 12 sinusoidal oscillations have been implemented and the force on the trapped bead has been measured. We have excluded the initial and the final oscillations to avoid any artefact driven by transient signals. To compute error bars in measuring G' and G'', we have therefore used

the ten intermediate oscillations. The computed values of G' and G'' are seen to be reasonably consistent and the deviations for these ten different cycles are presented as error bars.

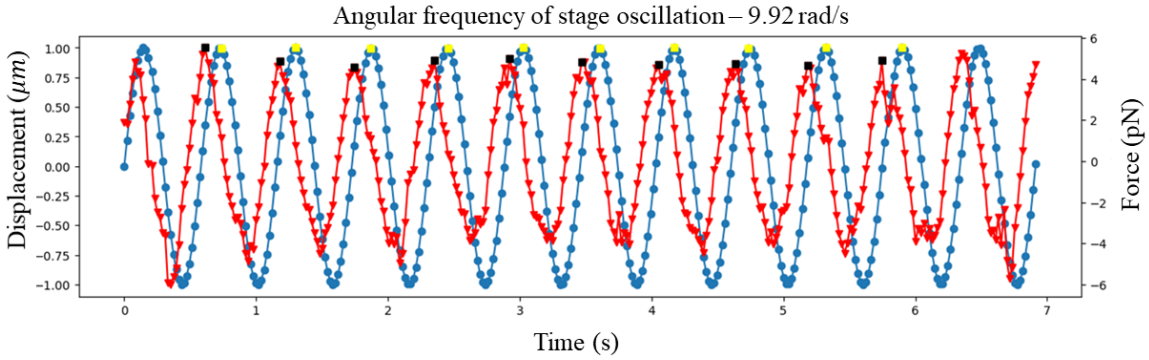

Figure 4.4: The blue curve with solid circles indicates the stage position with time. The peaks in the signal are detected using scipy module in Python. The peaks in the stage oscillation signals are indicated using yellow squares. The force on the trapped particle is shown by the red curve with red triangles. The black squares indicate the peaks of the force signal.

The ten intermediate peaks, obtained after excluding the first and last oscillations as discussed in the previous paragraph, are used to calculate the time difference between the peaks of the applied stage displacement and the corresponding force measurement in Fig.4.4. This results in 10 estimates of time differences which are used to compute the mean and standard deviation in the phase angles measured using the protocol below,

$$t_{diff} = mean(t_1, t_2, ., t_{10}) \tag{4.3}$$

$$t_{error} = standard\ deviation(t_1, t_2, ., t_{10}) \tag{4.4}$$

Phase angles in degree are estimated computing, $\phi_{diff} = 360^\circ * f * t_{diff}$, $\phi_{error} = 360^\circ * f * t_{error}$ where f = stage oscillation frequency (in Hz). The mean and standard deviation of the phase angles calculated according to the method as described above are used to calculate the mean and standard deviation values of the elastic and viscous moduli using Eqns.4.1 and 4.2,

$$G' = \frac{F_{max}}{6\pi RX_{max}} cos(\frac{\pi\phi_{diff}}{180}),\ \Delta G' = \frac{F_{max}}{6\pi RX_{max}} sin(\frac{\pi\phi_{diff}}{180})(\pi\phi_{error}/180) \quad (4.5)$$

$$G'' = \frac{F_{max}}{6\pi RX_{max}} sin(\frac{\pi\phi_{diff}}{180}),\ \Delta G'' = \frac{F_{max}}{6\pi RX_{max}} cos(\frac{\pi\phi_{diff}}{180})(\pi\phi_{error}/180) \quad (4.6)$$

where $\Delta\phi = \frac{\pi\phi_{diff}}{180}$. G' and G'' with error bars are plotted in transparent colors in the Fig.4.5. The maximum error propagation while computing G_{co} and ω_{co} is estimated by considering the maximum ranges of errors of these two variables, marked using the dashed lines for both horizontal and vertical directions. To calculate the errors in crossover modulus G_{co} and relaxation time τ_{co}, the following relations have been used: $G_{co} = (G_{co2} + G_{co1})/2$, $\Delta G_{co} = (G_{co2} - G_{co1})/2$, $\omega_{co} = (\omega_{co2} + \omega_{co1})/2$, $\Delta\omega_{co} = (\omega_{co2} - \omega_{co1})/2$, $\tau_{co} = 2\pi/\omega_{co}$, $\Delta\tau_{co} = (2\pi/\omega_{co}^2)\Delta\omega_{co}$.

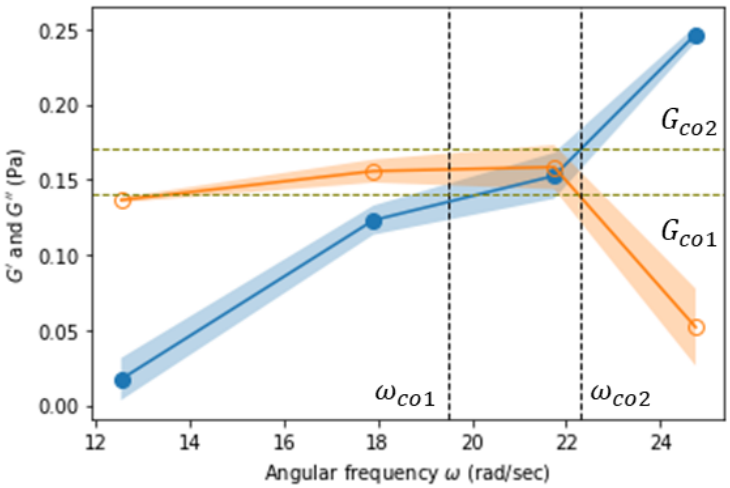

Figure 4.5: G' (solid blue symbols) and G'' (hollow orange symbols) and the corresponding error bars are shown by the shaded regions of the same colour. The maximum possible ranges of the crossover values of the moduli and angular frequencies are marked using the dashed horizontal and vertical lines.

Strengthening of Laponite networks with increasing Laponite concentration at a fixed aging time: Fig.4.6(a) shows the elastic modulus, G′, and the viscous modulus, G″, as a function of stage oscillation frequency ω at a predetermined aging time t_w = 90 minutes for various Laponite suspension concentrations

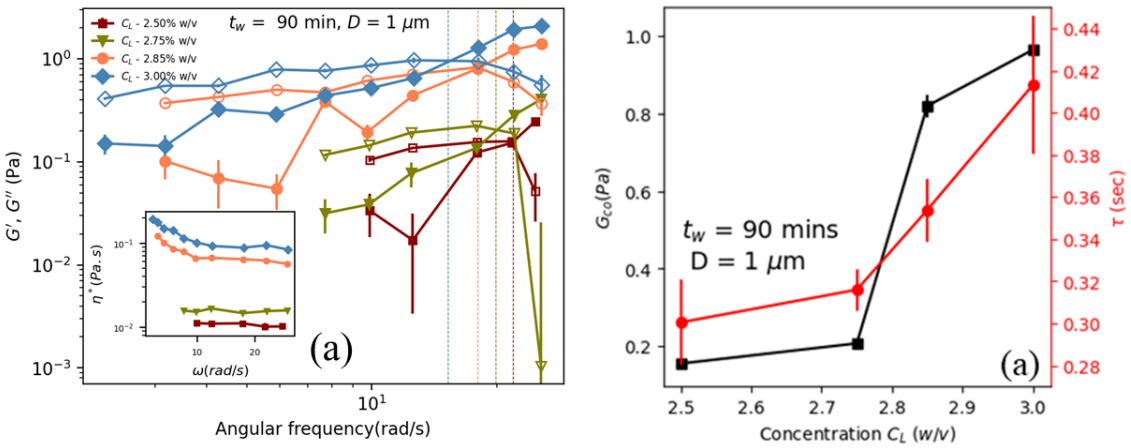

Figure 4.6: (a) Elastic moduli G' (solid symbols) and viscous moduli G'' (hollow symbols) obtained in microrheological measurements using a probe particle of diameter $D = 1$ μm and plotted *vs.* angular frequencies of the sample stage for different Laponite suspension concentrations C_L at an aging time $t_w = 90$ min. The vertical dashed lines represent the crossover frequencies where $G' = G''$ for data acquired at different C_L. In the inset, the frequency-dependent complex viscosities $\eta^* = \sqrt{G'^2 + G''^2}/\omega$ are plotted for the same Laponite concentrations. (b) Crossover modulus G_{co} (black) and relaxation time τ (red) of the underlying Laponite suspensions are plotted for different Laponite suspension concentrations C_L.

C_L. All the active microrheology measurements are performed using an optically trapped probe particle of diameter $D = 1$ μm. At small ω, we note that the G'' dominates over G' for all Laponite concentrations C_L, indicating viscoelastic liquid-like response of the suspension at small frequencies even 90 minutes after preparation.

We see that G' increases with increasing ω and becomes numerically equal to G'' at a crossover frequency ω_{co}, with a corresponding crossover modulus G_{co}. The suspension starts showing viscoelastic solid like behaviour when the stage oscillation frequency exceeds ω_{co}. We also calculate the frequency-dependent complex viscosities, $\eta^* = \sqrt{(G'^2 + G''^2)}/\omega$, for Laponite suspensions of various C_L at an aging time t_w of 90 minutes (inset of Fig.4.6(a)). The complex viscosity at low C_L remains almost unchanged with increasing ω, implying that the suspension structure remains invariant under the applied external perturbations. The shear exerted by the probe polystyrene particle is therefore too weak to destructure the underlying Laponite microstructures under these conditions. We note that η^* increases with in-

creasing C_L, which is in agreement with a previous report on passive microrheology experiments with Laponite suspensions [39]. The characteristic relaxation time τ corresponding to each C_L is obtained from the reciprocal of the crossover frequency $\tau = 2\pi/\omega_{co}$. Fig.4.6(b) shows that the crossover modulus G_{co} and τ increase monotonically with increasing C_L thereby indicating the strengthening of the underlying Laponite suspension networks with increasing suspension concentration at a fixed Laponite age.

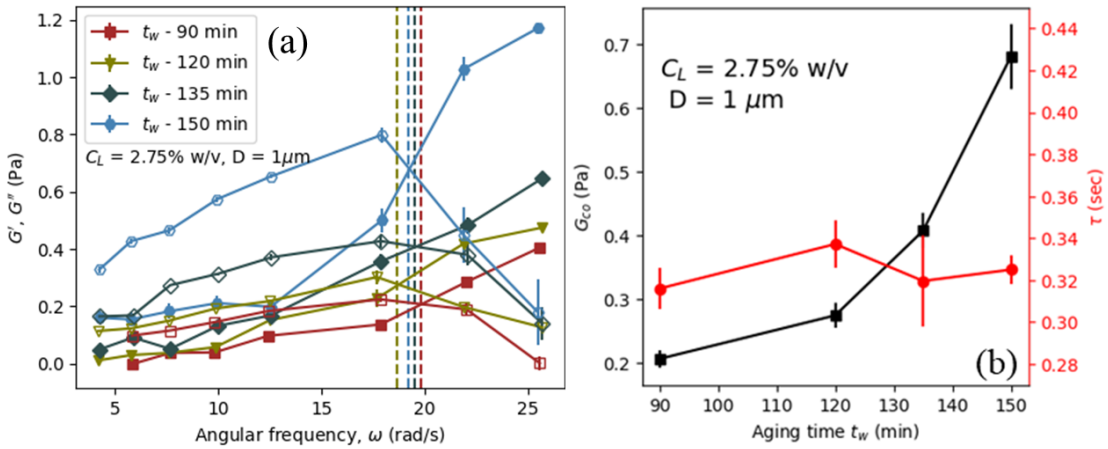

Figure 4.7: (a) Elastic and viscous moduli, G′ and G″ respectively, are estimated using oscillatory active microrheology for a 2.75% w/v Laponite suspension at different aging times t_w. (b) Crossover modulus G_{co} (black) and relaxation time τ (red) of the underlying Laponite suspensions are plotted for different Laponite suspension aging times t_w.

Strengthening of Laponite network structures with increasing suspension age at a fixed suspension concentration: To understand the temporal evolution of the mechanical moduli of a Laponite suspension of fixed concentration C_L = 2.75% w/v, we perform active microrheology experiments at various suspension aging times, t_w, ranging from 90 to 150 minutes using a probe particle of diameter D = 1 μm. We observe that G' and G'' follow similar trends with varying t_w (plotted in Fig.4.7(a)) as observed in the earlier experiments in which C_L was varied at a fixed t_w (plotted in Fig.4.6(a)). The crossover modulus G_{co} and characteristic relaxation time τ for Laponite suspensions at different t_w are shown in Fig.4.7(b). G_{co} increases with aging time t_w and suggests the strengthening of the suspension networks with

time due to enhancement in the inter-particle electrostatic interactions. Interestingly, we observe that τ does not change significantly over the range of t_w explored here. As the probe particle is attached to the Laponite networks, the relaxation process during stage oscillation depends on both the probe particle and morphology of the Laponite networks. The interaction between the probe particle connected to the network and the solvent is important for understanding the relaxation process observed in experiments. The approximately constant values of τ in Fig.4.7(b) indicate minimal changes in the suspension dynamics within the explored t_w range. We note that all the measurements are performed with Laponite suspensions of ages $t_w \geq 90$ minutes and Laponite microstructures are presumably already well-formed within the suspension. Therefore, even though the networks continue to strengthen with age, the data in Fig.4.7(b) indicates that dynamical changes of the kinetically arrested medium are minimal at the microscopic scale.

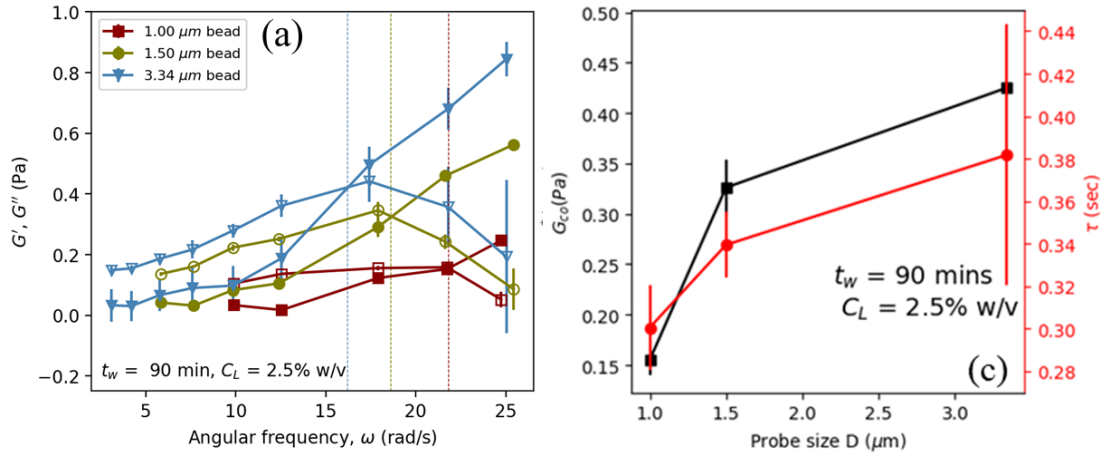

Figure 4.8: (a) G′ and G″ are estimated for a 2.75% w/v Laponite suspension at aging time $t_w = 90$ minutes using oscillatory active microrheology with probe particles of different sizes D. (b) Crossover modulus G_{co} (black) and relaxation time τ (red) of the underlying Laponite suspensions are plotted for different trapped probe particle sizes D.

Probe size dependence of measured Laponite viscoelasticity: We next explore the lengthscale dependent microrheology of Laponite suspensions by varying the sizes D of the trapped colloidal probe particles. Active microrheology measurements are performed to study Laponite suspensions of $C_L = 2.5\%$ w/v and

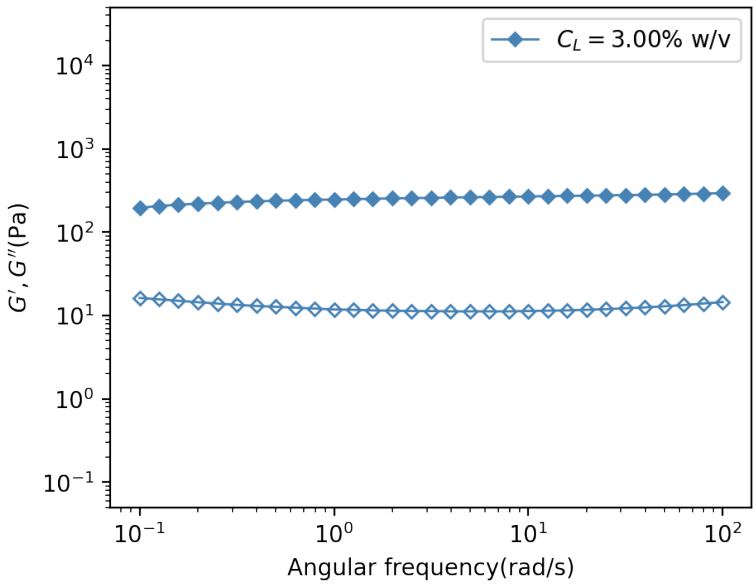

Figure 4.9: Macroscopic or bulk elastic and viscous moduli, G′ and G″ respectively, of a Laponite suspension of concentration $C_L = 3.00\%$ w/v at aging time $t_w = 90$ min measured using a rheometer.

$t_w = 90$ minutes while trapping probe particles of sizes 1, 1.5 and 3.34 μm shown in Fig.4.8(a).The elastic modulus G' and viscosity η^* of the underlying Laponite suspension measured using a larger probe is higher when compared to that measured with smaller probes. Since the surface area of a bigger bead is larger, the connectivity between the bead and suspension microstructure is stronger. The drag on a probe particle therefore increases as its size becomes larger. We note that active microrheology with bigger probes results in estimates of longer characteristic relaxation times τ and higher crossover moduli G_{co} of the underlying Laponite suspension medium, as displayed in Fig.4.8(b). Therefore, active microrheology experiments can reveal the length-scale dependence of mechanical properties which, in turn are directly dependent on the connectivity between the probe and Laponite particles.

Correlating pore sizes of Laponite networks with suspension dynamics: We note from Fig.4.1 of probe particles are comparable with the characteristic structural lengthscales of the suspension. In comparison to our microrheological mea-

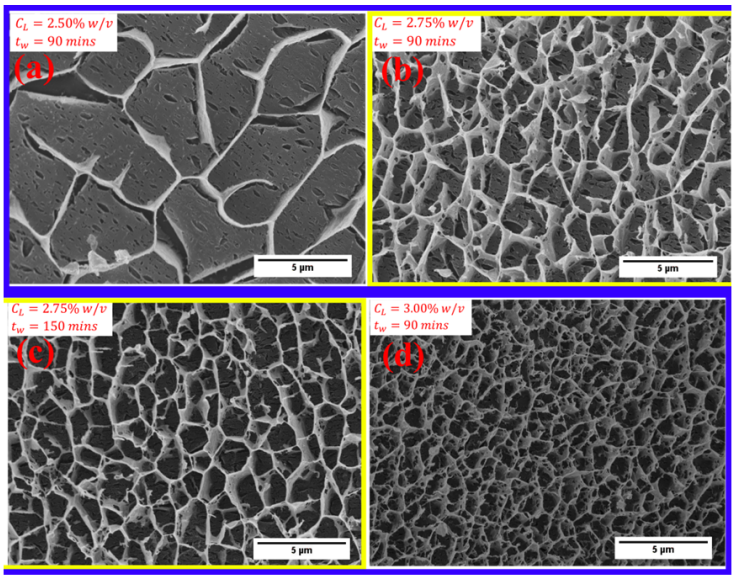

Figure 4.10: Cryo-FESEM images of Laponite suspensions of different concentrations C_L and aging times t_w **(a)** $C_L = 2.5$ % w/v, $t_w = 90$ mins, **(b)** $C_L = 2.75$ % w/v, $t_w = 90$ mins, **(c)** $C_L = 2.75$ % w/v, $t_w = 150$ mins, **(d)** $C_L = 3.0$ % w/v, $t_w = 90$ mins.

surements, representative bulk frequency response data for a Laponite suspension of concentration 3% w/v at $t_w = 90$ minutes (shown in Fig.4.9) shows solid like behaviour, as indicated by $G' >> G''$, over the entire frequency range explored. We note here that the microrheological data emphasises the liquid like response of the medium as the immediate neighbourhood of the probe particle comprises mostly the water medium. We directly visualize Laponite microstructures in suspensions of different C_L and t_w using cryo-FESEM. Figs.4.10(a-b,d) show that microstructures are denser for suspensions with higher C_L. In contrast, we see that the network morphology does not change appreciably when suspensions of fixed concentration are imaged at different t_w (Figs.4.10(b-c)). The acquired cryo-FESEM images are binarized to emphasise the Laponite networks using an inbuilt module in the ImageJ software. The area within each pore is measured using ImageJ. The equivalent pore diameter is then estimated by assuming that the measured pore is circular. The average diameter $\langle D_p \rangle$ is determined by averaging the diameters of various pores (between $\approx$ 10-50). We observe that $\langle D_p \rangle$ decreases with increasing C_L but remains

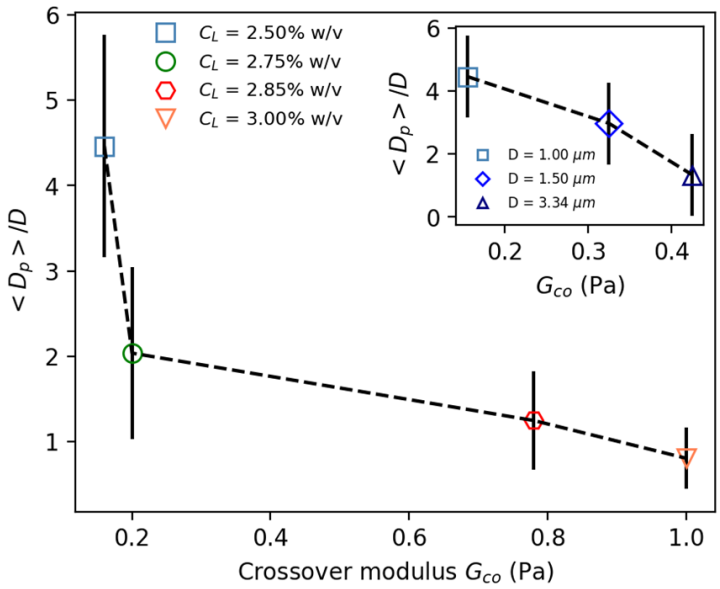

Figure 4.11: Pore size ratio $\langle D_p \rangle / D$, the ratio of average pore diameter $\langle D_p \rangle$ and the diameter of the trapped particle (D=1 μm), is plotted vs. crossover modulus G_{co} obtained from OT-based active microrheology for different Laponite concentrations C_L at t_w = 90 min. In the inset, the pore size ratio is plotted for different sizes of probe particles D = 1 μm, 1.5 μm, 3.34 μm for Laponite suspension concentration C_L = 2.5% and aging time t_w = 90 min.

almost unchanged with increasing t_w. This result is in agreement with passive microrheology results reported earlier [40, 41] and implies a correlation between the sample structure and its mechanical response at microscopic lengthscales.

Fig.4.11 consolidates the OT and cryo-FESEM data analyses to display the variation of the average dimensionless pore diameters, $\langle D_p \rangle / D$, where $\langle D_p \rangle$ is obtained from cryo-FESEM and normalized by the probe size D. $\langle D_p \rangle / D$ is a dimensionless lengthscale and is plotted as a function of the crossover modulus G_{co} extracted from our active microrheology experiments (Fig.4.11). We note that the lower values of G_{co} in Fig.4.11 correspond to data analyzed from active microrheology measurements performed with samples of lower C_L. We observe a clear inverse correlation between $\langle D_p \rangle / D$ and the crossover modulus G_{co}. This implies that Laponite suspensions having denser microstructures at larger C_L show increasingly viscoelastic solid-like behaviour and have larger characteristic relaxation times. We note from the inset of Fig.4.11 that for a fixed Laponite concentration of 2.75% w/v, $\langle D_p \rangle / D$

decreases with increasing crossover modulus G_{co} for various probe particle sizes D. This observation clearly shows that active microrheology measurements are probe size-dependent and soft glassy Laponite suspensions having finite rigidities exhibit lengthscale dependent mechanical properties. This observation agrees with a previous report on passive microrheology of Laponite suspensions [23]. The length-scale dependent mechanical properties of Laponite suspensions is a direct consequence of the heterogeneous network structures that evolve in aging Laponite suspensions. Interestingly, a theoretical work that proposed an elastic model to describe the hierarchical arrest of attractive colloidal particles demonstrated that it is possible to distinguish between the microscopic (particle-scale) and mesoscopic (cluster-scale) contributions to the macroscopic shear modulus [42]. OT based active microrheology studies can therefore serve as an excellent starting point to quantify such spatiotemporal heterogeneities.

4.4 Conclusions

A Laponite suspension shows physical aging, which is manifested as a continuous evolution of the mechanical properties of the suspension with time [35, 37]. While in passive microrheology, accurate measurements are limited by the probe-size dependence of the diffusive dynamics, the application of external forces in active microrheology allows the measurement of mechanical properties that are inaccessible using the former method. In this chapter, we systematically perform oscillatory active microrheological experiments with aging aqueous Laponite suspensions using an optical tweezer. The aim of this work is to uncover correlations between the morphologies of the aging Laponite suspension structures and the probe particle dynamics at micrometer lengthscales.

Polystyrene particles interact with Laponite particles and attach physically to the suspension microstructures. We visualize this attachment using cryo-FESEM imaging. Typically, the size of the probe used in tweezing experiments should be

larger than the characteristic lengthscale of the underlying system [43]. When the probe particle interacts with the network, microrheological responses can be extracted even when the characteristic lengthscales of the suspension microstructures are larger in comparison to the probe size [24]. Controlled sinusoidal oscillations of the sample stage, even as the probe particle is optically trapped and attached to the microstructures of the suspension, allows us to extract the viscoelastic properties of the underlying medium. We note that the measured complex viscosities of the suspension do not change appreciably over the range of frequencies explored in our experiment, particularly for the samples of lower concentrations. The Laponite medium is therefore not destructured by the shear forces exerted by the trapped probe particle. Our microrheology data establishes that the suspension networks can strengthen significantly regardless of whether suspension concentration or age is changed. With increasing suspension age and concentration, the Debye layer surrounding each Laponite particle shrinks [44], resulting in increased participation of the particles in the branches of the Laponite gel network due to enhancement in the particle edge-face attractive interactions. While the crossover modulus G_{co} measures the strengthening of the gel network due to enhanced Laponite particle self-assembly, the relaxation time τ provides an estimate of the dynamics of the probe particle trapped in the network pore. We show here that while the network strengthens considerably when suspension concentration, age and probe particle diameter are increased, the dynamical timescale shows only modest change over the parameter space explored. Our observations such as enhancement of moduli with increase in suspension concentration and age resemble the results extracted from bulk rheology experiments [45] but have never been reported at microscopic lengthscales using active microrheology. It has been predicted that the macroscopic rheology of arrested states depends on the ratio of particle cluster size and dimension of an individual particle [42]. Interestingly, this would result in lengthscale dependent rheology as demonstrated here and also previously reported for other soft materials in the literature in different contexts [23, 46, 47].

We systematically demonstrate that the rheological properties of soft glassy Laponite suspensions [48, 49] are correlated with the underlying suspension structure, *viz.*, the average network pore sizes of the suspension networks imaged using Cryo-FESEM. We show that over the range of aging times investigated here for a fixed Laponite concentration, the underlying structure is approximately invariant. When the Laponite concentration C_L increases, the network structure, visualized using cryo-FESEM, becomes denser. We demonstrate that the crossover modulus of the suspensions, obtained from active microrheology measurements, are inversely correlated with the average pore sizes of the Laponite networks. Such a correlation between the lengthscale characterising the suspension network and the characteristic relaxation times of the suspensions at micrometre scales is shown for the first time using optical tweezer based active microrheology.

Our results can be applied to study the effects of local sample heterogeneities during transport of micron-sized particles through complex environments, for example, in drug delivery [50]. Laponite is utilised as a rheological modifier [51, 52] in material processing applications, and knowledge of micron-scale local dynamics is necessary for achieving the desired outcomes. A possible extension of the present work could involve the setting up of multiple traps to precisely study the short-range suspension-mediated interactions [53, 54], or to understand the effects of quenched defects in a viscoelastic medium [55]. Non-linear vicoelasticity [56] of aging Laponite suspensions can be explored even at microscopic lengthscales by applying large amplitude stage oscillations. These studies could shed additional light on the dynamics of local relaxations and defects in kinetically arrested states of colloidal suspensions. Different additives and external fields can be incorporated in Laponite suspensions to fine-tune the rheological response of the latter [57]. This work could be extended to estimate micron-scale mechanical responses due to incorporation of a range of additives or the application of various external fields.

Bibliography

[1] Arthur Ashkin, James M Dziedzic, John E Bjorkholm, and Steven Chu. Observation of a single-beam gradient force optical trap for dielectric particles. *Optics Letters*, 11(5):288–290, 1986.

[2] Scot C. Kuo and Michael P. Sheetz. Force of Single Kinesin Molecules Measured with Optical Tweezers. *Science*, 260(5105):232–234, 1993.

[3] Ulrich Bockelmann, Ph Thomen, B Essevaz-Roulet, Virgile Viasnoff, and Francois Heslot. Unzipping dna with optical tweezers: high sequence sensitivity and force flips. *Biophysical Journal*, 82(3):1537–1553, 2002.

[4] Kosta Ladavac, Karen Kasza, and David G Grier. Sorting mesoscopic objects with periodic potential landscapes: Optical fractionation. *Physical Review E*, 70(1):010901, 2004.

[5] Rae M Robertson-Anderson. Optical tweezers microrheology: from the basics to advanced techniques and applications. *ACS Macro Letters*, 7(8):892–1050, 2018.

[6] Tobias Neckernuss, Lina Katinka Mertens, Ines Martin, Tobias Paust, Michael Beil, and Othmar Marti. Active microrheology with optical tweezers: a versatile tool to investigate anisotropies in intermediate filament networks. *Journal of Physics D: Applied Physics*, 49(4):045401, 2015.

[7] Ellas Spyratou. Advanced Biophotonics Techniques: The Role of Optical Tweezers for Cells and Molecules Manipulation Associated With Cancer. *Frontiers in Physics*, 10, 2022.

[8] Keir C Neuman and Steven M Block. Optical trapping. *Review of scientific instruments*, 75(9):2787–2809, 2004.

[9] Philip H Jones, Onofrio M Maragò, and Giovanni Volpe. *Optical tweezers: Principles and applications*. Cambridge University Press, 2015.

[10] Jan Gieseler, Juan Ruben Gomez-Solano, Alessandro Magazzù, Isaac Pérez Castillo, Laura Pérez García, Marta Gironella-Torrent, Xavier Viader-Godoy, Felix Ritort, Giuseppe Pesce, Alejandro V Arzola, et al. Optical tweezers—from calibration to applications: a tutorial. *Advances in Optics and Photonics*, 13(1):74–241, 2021.

[11] Pierre Jop, Juan Ruben Gomez-Solano, Artyom Petrosyan, and Sergio Ciliberto. Experimental study of out-of-equilibrium fluctuations in a colloidal suspension of laponite using optical traps. *Journal of Statistical Mechanics: Theory and Experiment*, 2009(04):P04012, 2009.

[12] Sara Jabbari-Farouji, Daisuke Mizuno, Maryam Atakhorrami, Fred C MacKintosh, Christoph F Schmidt, Erika Eiser, Gerard H Wegdam, and Daniel Bonn. Fluctuation-dissipation theorem in an aging colloidal glass. *Physical Review Letters*, 98(10):108302, 2007.

[13] Christopher W Macosko. *Rheology: Principles, Measurements, and Applications*. VCH Publishes, New York, 1994.

[14] Daniel T.N. Chen, Qi Wen, Paul A. Janmey, John C. Crocker, and Arjun G. Yodh. Rheology of soft materials. *Annual Review of Condensed Matter Physics*, 1(1):301–322, 2010.

[15] Thomas G Mason and David A Weitz. Optical measurements of frequency-dependent linear viscoelastic moduli of complex fluids. *Physical Review Letters*, 74(7):1250, 1995.

[16] Thomas A Waigh. Microrheology of complex fluids. *Reports on Progress in Physics*, 68(3):685, 2005.

[17] Antonio M Puertas and Thomas Voigtmann. Microrheology of colloidal systems. *Journal of Physics: Condensed Matter*, 26(24):243101, 2014.

[18] John C. Crocker and David G. Grier. Methods of Digital Video Microscopy for Colloidal Studies. *Journal of Colloid and Interface Science*, 179(1):298–310, 1996.

[19] Bivash R Dasgupta, Shang-You Tee, John C Crocker, B J Frisken, and D A Weitz. Microrheology of polyethylene oxide using diffusing wave spectroscopy and single scattering. *Physical Review E*, 65(5):051505, 2002.

[20] M. Tassieri, T. A. Waigh, John Trinick, Amalia Aggeli, and R. M. L. Evans. Analysis of the linear viscoelasticity of polyelectrolytes by magnetic microrheometry—Pulsed creep experiments and the one particle response. *Journal of Rheology*, 54(1):117–131, 2010.

[21] Manlio Tassieri, Graham M. Gibson, R. M. L. Evans, Alison M. Yao, Rebecca Warren, Miles J. Padgett, and Jonathan M. Cooper. Measuring storage and loss moduli using optical tweezers: Broadband microrheology. *Phys. Rev. E*, 81:026308, Feb 2010.

[22] S. Jabbari-Farouji, R. Zargar, G. H. Wegdam, and Daniel Bonn. Dynamical heterogeneity in aging colloidal glasses of laponite. *Soft Matter*, 8:5507–5512, 2012.

[23] Jason P Rich, Gareth H McKinley, and Patrick S Doyle. Size dependence of microprobe dynamics during gelation of a discotic colloidal clay. *Journal of Rheology*, 55(2):273–299, 2011.

[24] M.T. Valentine, Z.E. Perlman, M.L. Gardel, J.H. Shin, P. Matsudaira, T.J. Mitchison, and D.A. Weitz. Colloid surface chemistry critically affects multiple particle tracking measurements of biomaterials. *Biophysical Journal*, 86(6):4004–4014, 2004.

[25] Jun He and Jay X Tang. Surface adsorption and hopping cause probe-size-dependent microrheology of actin networks. *Physical Review E*, 83(4):041902, 2011.

[26] Lilian C Hsiao, Michael J Solomon, Kathryn A Whitaker, and Eric M Furst. A model colloidal gel for coordinated measurements of force, structure, and rheology. *Journal of Rheology*, 58(5):1485–1504, 2014.

[27] D. Mizuno, D. A. Head, F. C. MacKintosh, and C. F. Schmidt. Active and passive microrheology in equilibrium and nonequilibrium systems. *Macromolecules*, 41(19):7194–7202, 2008.

[28] François Amblard, Anthony C Maggs, Bernard Yurke, Andrew N Pargellis, and Stanislas Leibler. Subdiffusion and anomalous local viscoelasticity in actin networks. *Physical Review Letters*, 77(21):4470, 1996.

[29] Annafrancesca Rigato, Atsushi Miyagi, Simon Scheuring, and Felix Rico. High-frequency microrheology reveals cytoskeleton dynamics in living cells. *Nature Physics*, 13(8):771–775, 2017.

[30] Barbara Ruzicka and Emanuela Zaccarelli. A fresh look at the laponite phase diagram. *Soft Matter*, 7:1268–1286, 2011.

[31] A Shahin and Yogesh M Joshi. Physicochemical effects in aging aqueous laponite suspensions. *Langmuir*, 28(44):15674–15686, 2012.

[32] Rajkumar Biswas, Debasish Saha, and Ranjini Bandyopadhyay. Quantifying the destructuring of a thixotropic colloidal suspension using falling ball viscometry. *Physics of Fluids*, 33(1):013103, 2021.

[33] Bérengère Abou and Francois Gallet. Probing a nonequilibrium einstein relation in an aging colloidal glass. *Physical Review Letters*, 93(16):160603, 2004.

[34] Felix K Oppong, P Coussot, and John R de Bruyn. Gelation on the microscopic scale. *Physical Review E*, 78(2):021405, 2008.

[35] Daniel Bonn, Sorin Tanase, Bérengère Abou, Hajime Tanaka, and Jacques Meunier. Laponite: Aging and shear rejuvenation of a colloidal glass. *Physical Review Letters*, 89(1):015701, 2002.

[36] Samim Ali and Ranjini Bandyopadhyay. Evaluation of the exfoliation and stability of na-montmorillonite in aqueous dispersions. *Applied Clay Science*, 114:85–92, 2015.

[37] Samim Ali and Ranjini Bandyopadhyay. Effect of electrolytes on the microstructure and yielding of aqueous dispersions of colloidal clay. *Soft Matter*, 12:414–421, 2016.

[38] F Ziemann, J Rädler, and E Sackmann. Local measurements of viscoelastic moduli of entangled actin networks using an oscillating magnetic bead microrheometer. *Biophysical journal*, 66(6):2210–2216, 1994.

[39] Pierre Jop, Juan Ruben Gomez-Solano, Artyom Petrosyan, and Sergio Ciliberto. Experimental study of out-of-equilibrium fluctuations in a colloidal suspension of laponite using optical traps. *Journal of Statistical Mechanics: Theory and Experiment*, 2009(04):P04012, 2009.

[40] Bingqian Zheng, James R Breton, Ruchi S Patel, and Surita R Bhatia. Microstructure, microrheology, and dynamics of laponite® and laponite®-poly (ethylene oxide) glasses and dispersions. *Rheologica Acta*, 59(6):387–397, 2020.

[41] Bhavna M Vyas, Ashish V Orpe, Manish Kaushal, and Yogesh M Joshi. Passive microrheology in the effective time domain: analyzing time dependent colloidal dispersions. *Soft Matter*, 12(39):8167–8176, 2016.

[42] Alessio Zaccone, Hua Wu, and Emanuela Del Gado. Elasticity of arrested short-ranged attractive colloids: Homogeneous and heterogeneous glasses. *Physical Review Letters*, 103(20):208301, 2009.

[43] Manlio Tassieri. *Microrheology with Optical Tweezers: Principles and Applications*. CRC Press, 2016.

[44] Debasish Saha, Ranjini Bandyopadhyay, and Yogesh M Joshi. Dynamic Light Scattering Study and DLVO Analysis of Physicochemical Interactions in Colloidal Suspensions of Charged Disks. *Langmuir*, 31(10):3012–3020, 2015.

[45] D Bonn, P Coussot, HT Huynh, F Bertrand, and G Debrégeas. Rheology of soft glassy materials. *Europhysics Letters*, 59(5):786, 2002.

[46] J Liu, ML Gardel, K Kroy, Erwin Frey, Brenton D Hoffman, John C Crocker, AR Bausch, and DA Weitz. Microrheology probes length scale dependent rheology. *Physical Review Letters*, 96(11):118104, 2006.

[47] Nicholas Agung Kurniawan, Chwee Teck Lim, and Raj Rajagopalan. Image correlation spectroscopy as a tool for microrheology of soft materials. *Soft Matter*, 6(15):3499–3505, 2010.

[48] A Mourchid, A Delville, J Lambard, E Lecolier, and P Levitz. Phase diagram of colloidal dispersions of anisotropic charged particles: equilibrium properties, structure, and rheology of laponite suspensions. *Langmuir*, 11(6):1942–1950, 1995.

[49] Hajime Tanaka, Jacques Meunier, and Daniel Bonn. Nonergodic states of charged colloidal suspensions: Repulsive and attractive glasses and gels. *Physical Review E*, 69(3):031404, 2004.

[50] C Viseras, C Aguzzi, P Cerezo, and MC Bedmar. Biopolymer–clay nanocomposites for controlled drug delivery. *Materials Science and Technology*, 24(9):1020–1026, 2008.

[51] Seyed Amir Oleyaei, Seyed Mohammad Ali Razavi, and Kirsi S Mikkonen. Novel nanobiocomposite hydrogels based on sage seed gum-laponite: Physicochemical and rheological characterization. *Carbohydrate Polymers*, 192:282–290, 2018.

[52] José Luis Dávila and Marcos Akira d'Ávila. Laponite as a rheology modifier of alginate solutions: Physical gelation and aging evolution. *Carbohydrate Polymers*, 157:1–8, 2017.

[53] Jens-Christian Meiners and Stephen R Quake. Direct measurement of hydrodynamic cross correlations between two particles in an external potential. *Physical Review Letters*, 82(10):2211, 1999.

[54] R Di Leonardo, S Keen, F Ianni, J Leach, MJ Padgett, and G Ruocco. Hydrodynamic interactions in two dimensions. *Physical Review E*, 78(3):031406, 2008.

[55] M Cristina Marchetti and Karl Saunders. Viscoelasticity from a microscopic model of dislocation dynamics. *Physical Review B*, 66(22):224113, 2002.

[56] Juan Ruben Gomez-Solano and Clemens Bechinger. Probing linear and nonlinear microrheology of viscoelastic fluids. *Europhysics Letters*, 108(5):54008, 2014.

[57] Chandeshwar Misra, Venketesh T Ranganathan, and Ranjini Bandyopadhyay. Influence of medium structure on the physicochemical properties of aging colloidal dispersions investigated using the synthetic clay laponite®. *Soft Matter*, 17(41):9387–9398, 2021.

Chapter 5

AC electric field induced controlled aging of aqueous Laponite suspension

5.1 Introduction

Colloidal suspensions or complex fluids whose rheological properties can be varied reversibly using an electric field are known as electrorheological (ER) fluids. Since their discovery by Willis Winslow in 1949 [1], ER fluids have been a relevant subject of research due to their broad range of applications. A wide variety of organic and inorganic materials such as polymer composites, colloidal suspensions, clay suspensions, are categorised as ER materials. The constituent particle sizes can range from nanometers to micrometres, and they may take on different forms, including spherical, fibrous, sheet-like, and rod-like in the presence of an electric field. Immediately upon application of an electric field, ER fluids start to polarise and the particles assemble to form chains [2, 3]. Consequently, their rheological properties, such as viscosity, shear stress, dynamic moduli and stress relaxation, are altered substantially depending on the strength of the field. These changes in rheological properties are not permanent and can be reversed by removing the field. Electrorheological flu-

ids are used in various industrial fields for their ability to generate resistive forces and damping. Their application in microfluidics has been reported by Wang *et.al.* [4]. Moreover, ER fluids have growing demands and large applications as dampers [5], shock absorbers, tactile displays [6] and clutches [7]. Automobile industries nowadays utilise ER fluids for increased efficiency of cooling engines, torque controlled brakes [8, 9].

Under the influence of an external electric field, electrorheological fluids can undergo a phase change from liquid to solid. The constituent particles in these fluids percolate due to the formation of long-range inter-particle attractions induced by the electric field. The formation of medium-spanning structures enhances the medium's viscosity. Researchers have studied silica particles in PDMS and observed gelation in an electric field resembling chemical gelation [10]. Additionally, natural polymers such as starch, chitosan, and cellulose exhibit structure formation in the direction of an electric field [11]. Under an electric field, clay particles such as beidellite exhibit a nematic-like phase [12]. A mixture of Laponite clay and silicone oil also acts as an electrorheological fluid. The viscosity of the suspension changes dramatically above a certain amplitude of the applied electric field due to chain like structure formation of the Laponite particles [3]. Laponite clay suspensions in water, unlike the conventional electrorheological fluids, show irreversible mechanical changes due to the application of an external electric field [13]. Under DC electric field conditions, synthetic Laponite clay particles show a concentration gradient that is observable in the presence of a dye [14]. The evolution of spontaneous interparticle electrostatic interactions or aging in Laponite suspensions can be altered by applying an external electric field. Since interactions between Laponite particles are time-dependent in aqueous suspension, the microstructures formed in Laponite suspensions under an electric field do not disappear when the field is turned off.

As discussed in section 1.6 of Chapter 1, Laponite is a disk-shaped clay particle. Laponite tactoids swell and exfoliate to eventually break up into smaller particle clusters when dissolved in deionised water [15, 16]. A single Laponite particle devel-

ops negative charges on its face due to the dissolution of constituent Na^+ ions into the aqueous medium and positive charges on the rim due to hydration of magnesia groups. Electrical charges on the surface of Laponite particles and those contributed by Na^+ counterions play an important role on the aging property of Laponite suspensions [17], as discussed in previous chapters. The effect of DC electric field on the rheological property of Laponite suspension has been reported by Gadige et al. [13]. In the paper, the authors applied a range of DC fields from 2.5 V/mm to 10 V/mm. They explained their results by considering the separation of counterions and Laponite particles in the presence of the DC fields. The counterions move towards the anode and the Laponite particles, due to their negative charges, displace towards the cathode. The absence of counterions near the cathode enhances network formation by the asymmetrically charged Laponite particles, thereby speeding up the aging process.

In this work, we investigate the evolution of the microstructure of a Laponite suspension due to the application of an AC electric field. We use a rheometer and an optical tweezer to study the rheological properties of soft glassy Laponite suspensions at different lengthscales. A Laponite suspension (concentration, $C_L = 3.00$ % w/v) is loaded into a rheometer and subjected to an AC electric field while it ages. The field is turned off after 90 minutes and amplitude sweep measurements are performed. In the linear viscoelastic regime, G′ and G″ are insensitive to applied strain amplitude. Complex viscosity is defined $\eta^* = \sqrt{G'^2 + G''^2}/\omega$. We find that for increasing electric field strength, the complex viscosity of the sample in the linear viscoelastic regime, measured after subjecting the sample to different AC electric fields for 90 minutes, varies non-monotonically. The microrheology of the soft glassy Laponite suspension is also studied using optical tweezers (OT). In our OT measurements, we monitor the viscosity of a Laponite suspension ($C_L = 2.5$ % w/v) under the influence of external AC electric fields. The viscosity values are extracted from the corner frequency f_c, by fitting the power spectrum data of the displacements of the trapped bead (having a diameter of 1 μm) to Lorentzian functions (section 2.2.4 of Chapter 2). Rheology

and OT-based active microrheology in the presence of an electric field therefore both show non-monotonic evolutions of the complex viscosities and shear viscosities of the suspensions.

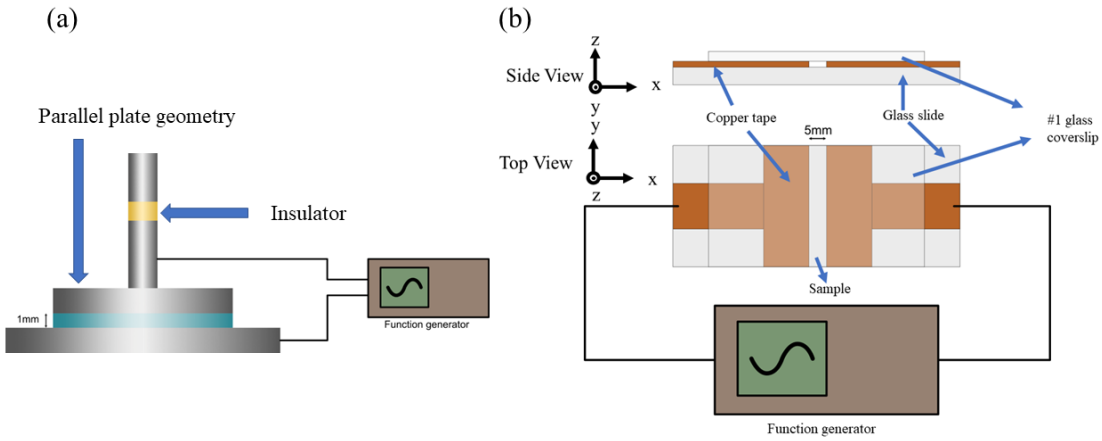

Figure 5.1: (a) A parallel plate geometry connected to a function generator is shown. The yellow patch is the insulating material used to insulate the rotating motor of a rheometer from the voltage source. The samples are filled between the parallel plates and shown in blue color. (b) The sample cell for electric field experiments used in the optical tweezer setup. The brown colour indicates the copper tape, which is connected to a function generator.

5.2 Materials and Methods

The experiments are performed in this chapter using Laponite clay suspensions. A detailed discussion about Laponite suspension and its aging property are mentioned in section 1.6 of Chapter 1. The sample preparation protocol is discussed in section 2.1 of Chapter 2. In this work, we apply an electric field to the Laponite suspension and measure its response using a rheometer and an optical tweezer. For the experiments using the rheometer, a modified measuring geometry is used for applying an external electric field to the suspension. We use a parallel plate geometry with conducting top plate and a base plate shown in Fig.5.1(a). The measuring head is connected to the function generator. This head has a small insulating element in the upper section. The insulating section stops the current from moving towards

the rotating synchronous motor of the rheometer. Laponite suspensions are loaded in between the rheometer base plate and measuring head. The lower base plate is also connected to a function generator. As a result, a uniform electric field can be applied to the samples loaded in the parallel plate geometry. For optical tweezer experiments, the sample cell is modified by using copper tape as spacers, shown in Fig.5.1(b). A function generator is connected to the copper tapes that are placed parallelly on both sides of the sample for applying an electric field in the x direction. The approximate distance between the copper tapes is kept around 5 mm. The electric field is calculated by dividing the peak voltage of the applied sinusoidal signal by the 5 mm gap value between the two electrodes.

5.3 Results and Discussion

5.3.1 Bulk rheology

The transformation of the aging clay suspensions to soft solids due to the presence of an AC electric field is studied by measuring the viscoelastic properties of the suspension. Laponite suspensions are prepared at a concentration of 3% w/v for bulk rheological experiments. After sample preparation, 2.5 ml of the suspension is filtered using a 0.45 μm Millipore sheet to avoid big clusters of Laponite particles and loaded into the parallel plate geometry of the rheometer using a syringe. The gap between the two parallel plates is fixed at 1 mm. After the loading is completed, a large shear rate (500 s^{-1}) is applied to the suspension for 5 mins to remove the initial loading effects. The sample is then kept undisturbed and an electric field is applied using an external function generator for the next 90 mins. Silicone oil is applied to the boundary of the parallel plate geometry to avoid evaporation during the waiting period. The field is turned off after 90 mins and rheological measurements are conducted. The microstructures of Laponite particles that presumably form due to the application of AC electric fields are studied using amplitude sweep measurements. Amplitude sweep experiments are performed for an angular frequency of 6

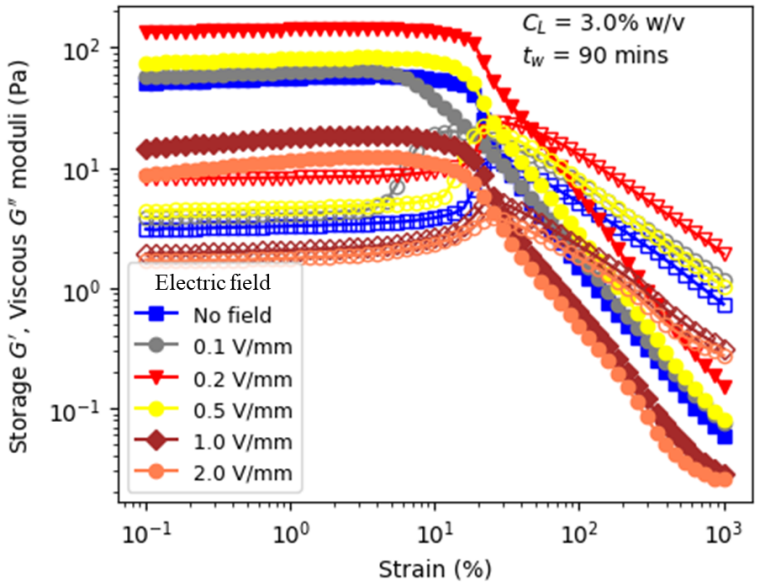

Figure 5.2: Elastic (G') and viscous (G'') moduli are plotted *vs.* strain amplitudes after applying different electric fields during 90 mins of aging to Laponite suspensions of concentration C_L = 3.00% w/v. Measurements are made immediately after the field is switched off.

rad/sec (0.95 s^{-1}) for strain amplitudes varying from 0.1% to 1000%. Storage (G') and viscoelastic (G'') moduli are measured with increasing strain amplitudes. The experimental data of G' (solid symbols) and G'' (hollow symbols) for Laponite suspensions corresponding to different electric fields are shown in Fig.5.2. At low strain values, G' and G'' are independent of applied strain amplitudes, implying that the microstuctures remain intact under low deformations. This range of strain values defines the linear viscoelastic region. In this region, G' values are higher than G'' which represents viscoelastic solid-like nature of the sample. As the strain increases, the crossover of G'' and G' indicates the onset of suspension flow. The strain value where $G' = G''$ is known as the yield point. At large strains, the suspension behaves like a viscoelastic liquid where G'' is higher than G' due to the breakdown of the underlying microstructures of Laponite suspensions.

Complex viscosity ($\eta^* = \frac{\sqrt{G'^2+G''^2}}{\omega}$), calculated using G' and G'' from the amplitude sweep measurements, is plotted versus strain amplitudes in Fig.5.3(a). In the linear viscoelastic region, the complex viscosity remains constant. The breakdown

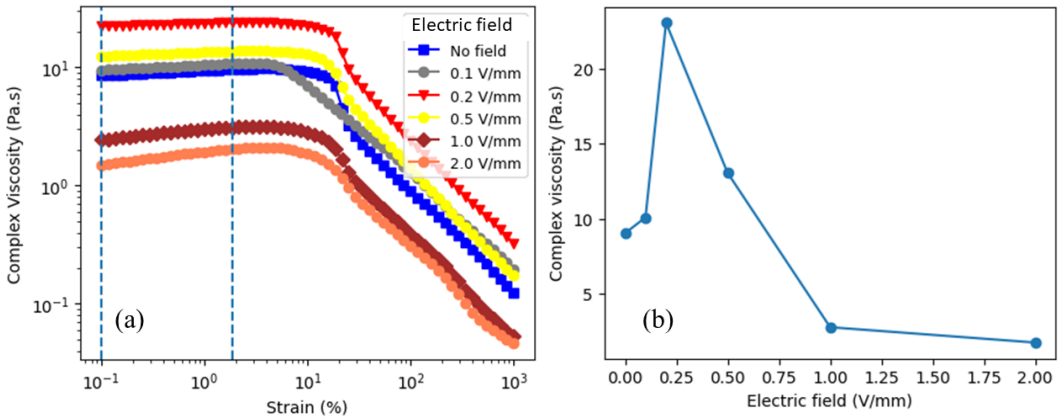

Figure 5.3: (a) Complex viscosity *vs.* strain amplitude is shown for various electric fields applied for 90 mins to Laponite suspensions of $C_L = 3.00\%$ and $t_w = 90$ mins. Complex viscosities in the linear regime, shown by the dashed lines, are used to calculate average complex viscosity values which are shown in (b) and plotted vs. electric field.

of structures in Laponite suspensions at high strain amplitudes results in the decrease of the measured complex viscosities. The linear viscoelastic region is roughly identified to lie between the dashed blue lines in Fig.5.3(a). The average complex viscosity in the linear regime is calculated and plotted for different applied sinusoidal electric field amplitudes at 1 kHz frequency in Fig.5.3(b). It is seen from this figure that the average complex viscosity increases with electric field amplitude and attains a peak at 0.2 V/mm before decreasing at high field amplitudes. To the best of our knowledge, such non-monotonic behaviour with increasing AC electric field has never been observed before for soft glassy Laponite suspensions.

5.3.2 Micro-rheology

The non-monotonic evolution of complex viscosities of Laponite suspensions with increase in AC electric field amplitudes as discussed in the previous section are expected due to changes in the microscopic assembly of Laponite particles. To investigate the effect of an electric field on the microrheology of a soft glassy sus-

pension, we prepare a Laponite suspension of 2.5% w/v and add a small amount of polystyrene beads of diameter 1 μm to perform OT-based microrheology experiments. A polystyrene bead is optically trapped in the Laponite suspension by

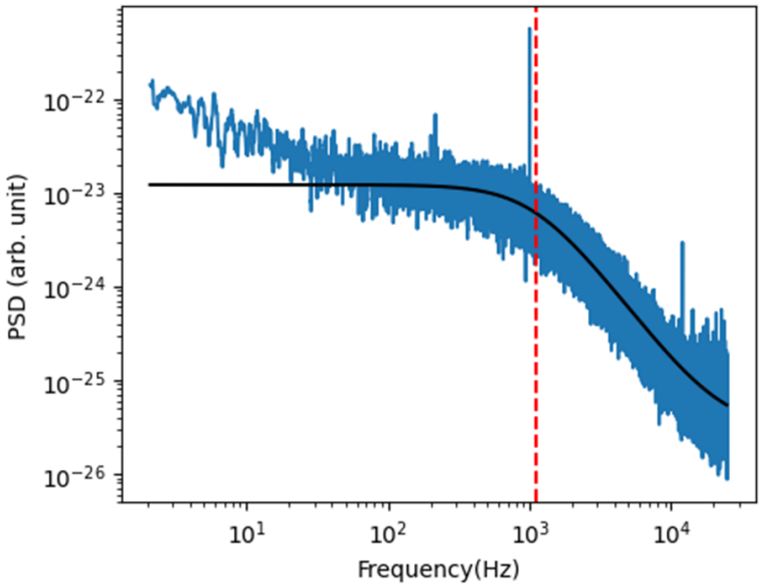

Figure 5.4: Power spectral density is plotted *vs.* frequency for a Laponite suspension of $C_L = 2.5\%$ w/v at $t_w = 30$ mins subjected to AC electric field of 0.5 V/mm (frequency 1 kHz). The black line is a fit to a Lorentzian function, $\frac{A}{f^2+f_c^2}$. The red vertical dashed line indicates the position of corner frequency obtained from the fit.

employing an optical tweezer set up to measure the viscosity of the suspension. In the presence of an electric field of 0.2 V/mm, a Laponite suspension of 3% w/v ages rapidly and it is not possible to study the evolution of its microstructure for a sufficient amount of time using the optical tweezer setup. So, we perform microrheology experiments with OT at a lower concentration of Laponite suspension (2.5% w/v), which ages more slowly than a sample having a concentration of 3% w/v.

Details of our OT-based microrheology experiment were discussed in Chapter 4. Here, we use the thermal motion of the trapped bead to calculate the viscosity of the medium. The trap stiffness calculation and the QPD calibration were discussed in section 2.2.4 of Chapter 2. We trap a bead of $D = 1$ μm in a Laponite suspension loaded in the sample cell (Fig.5.1(b)) and apply AC electric fields of magnitudes 0.1 V/mm - 2 V/mm. The displacement of the bead is tracked over time and the

Aging time (min) t_w	Corner frequency (Hz)				
	No field	0.1 V/mm	0.2 V/mm	0.5 V/mm	2.0 V/mm
0	1523.18	1490.70	1655.09	1568.78	1722.35
10	1347.40	1453.88	1505.47	1368.48	1691.88
20	1211.38	1191.86	1166.82	1401.59	1667.95
30	1222.55	912.29	449.40	1176.34	1404.87
40	1074.35	612.68		1058.54	1390.32
50	970.38	424.00		889.01	1204.22
60	882.06			630.11	1038.97
70	774.21			524.68	883.92

Table 5.1: Corner frequencies obtained for OT based microrheology experiments for different aging times and electric fields are shown for Laponite suspensions of $C_L = 2.5\%$ w/v and for different ages t_w.

corresponding power spectral density is computed. Fig.5.4 displays a representative power spectral density (PSD) computed for displacements of the trapped bead in a Laponite suspension of aging time t_w=30 minutes subjected to an electric field of 0.5 V/mm. The power spectral density data shown here is fitted using a Lorentzian function, PSD $= \frac{A}{f^2+f_c^2}$ [18], where A depends on the surrounding temperature, f is the frequency, $f_c = \kappa/2\pi\gamma$ is the corner frequency, κ is the trap stiffness and γ is the drag coefficient of the medium. At low Reynolds number, we can write $\gamma = 6\pi\eta R$, where η is the viscosity of the medium and R is the radius of the trapped bead [19]. By fitting the PSD data, corner frequencies obtained for different aging times and electric fields are tabulated in Table 5.1. The fitting error for the corner frequency is determined to be approximately 0.1%. From the corner frequency, the viscosity of the medium is calculated and the data is plotted in Fig.5.5(a) *vs*. Laponite aging time for different field strengths.

We see from Fig.5.5(a) that the viscosity increases with age which we attribute to the evolution of fragile suspension structures that develop due to the physical aging process discussed earlier in section 1.6. We see from Fig.5.5(b) that the viscosity of Laponite suspensions at $t_w = 30$ minutes is maximum at an applied external electric field of 0.2 V/mm. The viscosity of Laponite suspensions therefore evolves

differently for different electric fields. At 0.2 V/mm, there is a sharp increase in viscosity with aging time as seen in Fig.5.5(a), which precludes the measurement of viscosity beyond the aging time of 30 mins. A comparison of viscosities for different electric fields is restricted by this limitation and all the data is therefore plotted at an aging time of 30 mins in Fig.5.5(b). We see that the viscosity of the Laponite suspension at $t_w = 30$ mins, plotted in Fig.5.5(b), is maximum when 0.2 V/mm is applied to the sample. Therefore, we note that similar non-monotonic behaviour of viscosity is observed for both optical tweezer and rheometer measurements, with the viscosity being maximum when the magnitude of the applied field is 0.2 V/mm.

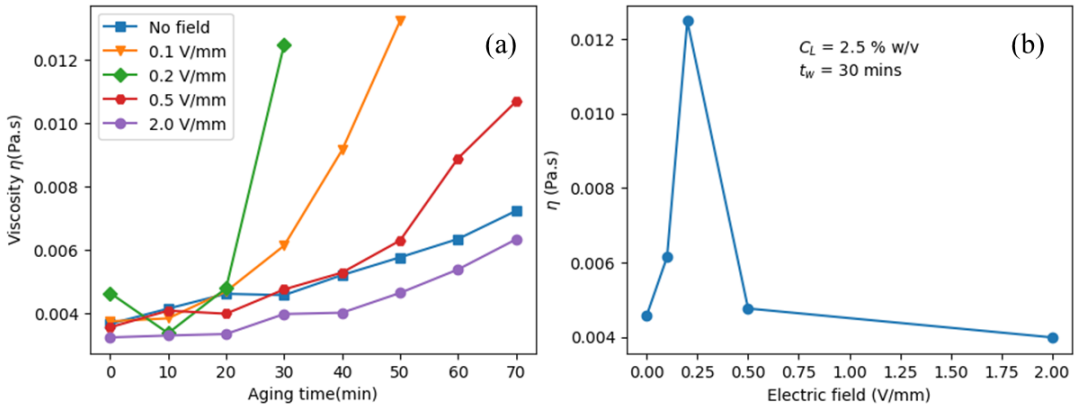

Figure 5.5: (a) Viscosity is plotted with aging time for different electric field strengths for Laponite concentration $C_L = 2.5\%$ w/v. (b) The viscosity of Laponite suspensions at $t_w = 30$ mins aging time *vs.* electric field is plotted.

As discussed in previous chapters, the viscosity of a Laponite suspension increases due to the slow evolution of the microstructure composed by the self-assembly of Laponite particles. We have already discussed that sodium ions Na^+ diffuse out from the interparticle space and form a double layer around Laponite particles.

The application of an electric field can perturb the double layer even at low amplitudes because Na^+ ions have higher mobility than Laponite particles [13, 20]. The deformation of the double layer consequently exposes the Laponite disks and modifies inter-Laponite interactions, resulting in the formation of edge-to-face contacts which enhances network formation. However, at the highest field amplitudes, it is possible that forces on the Laponite microstructures due to the applied electric

fields break or rupture the structures that are formed due to aging, leading to the slower increase in viscosity with aging time compared to the data acquired at 0.1 and 0.2 V/m (Fig.5.5(a)).

Bulk rheological measurements are conducted at a higher Laponite concentration than microrheological experiments. High Laponite concentrations result in denser microstructures of Laponite particles, as shown in Chapter 4. In this study, we observe that the decrease in complex viscosity or shear viscosity with increasing electric field from the peak value (at electric field of 0.2 V/mm) is slower for higher concentrations of Laponite with dense microstructures (Fig.5.3(b) and Fig.5.5(b)). The OT-based microrheology experiments probe much smaller lengthscales when compared to those investigated in bulk rheometric measurements. Interestingly, despite the different lengthscales involved, we see the same non-monotonic behaviour of the viscosities when the electric field strength is increased. When compared to bulk rheometric measurements, the significantly smaller values of viscosity obtained using the OT based microrheology experiments point to the fact that the latter technique is more sensitive to the surrounding water medium. This aspect was discussed in Chapter 4.

5.4 Conclusions

In this chapter, we presented results from bulk rheology and microrheology measurements that were performed to investigate the effect of AC electric fields on the aging of Laponite suspensions. It has been reported that dielectric particles and charged clay particles show exotic phases and patterns due to applied electric field [21–23]. Laponite has a negative charge on the face and a slight positive charge on the rims. The particle experiences force toward the anode under a DC field due to negative charges on its two faces [13]. It was also reported in this work that Laponite suspensions exhibit enhanced aging and concentration gradient towards the anode under the DC electric field. However, the effect of an AC electric field on soft glassy

Laponite suspensions has not been studied earlier to the best of our knowledge.

Using a rheometer and an optical tweezer, we investigate the rheological properties of Laponite suspensions that are subjected to AC electric fields of progressively larger strengths. The complex viscosities calculated from the amplitude sweep measurements show non-monotonic behaviour with increasing electric fields. Viscosity measurements using an optical tweezer under similar conditions also show accelerated aging, as manifested by an increase in the measured viscosity at a comparable electric field where the complex viscosity peak appears in the bulk rheology data. We propose that the non-monotonic behaviour of the viscosity with respect to electric field strength is due to the formation and disruption of Laponite microstructures driven by the applied external electric field.

The mobility and self-assembly of charged clay particles in aqueous suspension can therefore be manipulated using an AC electric field. These results shed further light on the significant alterations in the fragile Laponite microstructures due to the application of external perturbations. Laponite is used as a rheological modifier in various industrial sectors like paint, cosmetics, etc and the application of electric fields can be considered as a useful method to control the rheological properties of these Laponite composites. An earlier report shows that the gelation of Laponite suspensions can be controlled using different additives like chaotropes and kosmotropes [24]. The controlled aging of Laponite using an AC electric field as reported in this chapter can provide new insight on the correlations between structure and dynamics in fragile clay suspensions under external fields.

Bibliography

[1] Willis M. Winslow. Induced fibration of suspensions. *Journal of Applied Physics*, 20:1137–1140, 1949.

[2] James E. Martin, Judy Odinek, Thomas C. Halsey, and Randall D. Kamien. Structure and dynamics of electrorheological fluids. *Physical Review E*, 57:756–775, 1998.

[3] KPS Parmar, Yves Méheust, Børge Schjelderupsen, and JO Fossum. Electrorheological suspensions of laponite in oil: rheometry studies. *Langmuir*, 24(5):1814–1822, 2008.

[4] Limu Wang, Xiuqing Gong, and Weijia Wen. Electrorheological fluid and its applications in microfluidics. In *Microfluidics: Technologies and Applications*, pages 91–115. Springer, 2011.

[5] Hiroshi Yamaguchi, Xin-Rong Zhang, Xiao-Dong Niu, and K. Nishioka. Investigation of impulse response of an er fluid viscous damper. *Journal of Intelligent Material Systems and Structures*, 21:423 – 435, 2010.

[6] Yanju Liu, Robert Oscar Davidson, and Paul Taylor. Touch sensitive electrorheological fluid based tactile display. *Smart Materials and Structures*, 14:1563 – 1568, 2005.

[7] S B Choi and D. Y. Lee. Rotational motion control of a washing machine using electrorheological clutches and brakes. *Proceedings of the Institution of*

Mechanical Engineers, Part C: Journal of Mechanical Engineering Science, 219:627 – 637, 2005.

[8] Martin Gurka, Lucien Johnston, and Raino Petricevic. New electrorheological fluids — characteristics and implementation in industrial and mobile applications. *Journal of Intelligent Material Systems and Structures*, 21:1531 – 1535, 2009.

[9] Sudipto Datta, Ranjit Barua, and Jonali Das. A review on electro-rheological fluid (er) and its various technological applications. *Extremophilic Microbes and Metabolites - Diversity, Bioprospecting and Biotechnological Applications*, 2020.

[10] Byung Doo Chin and H. Henning Winter. Field-induced gelation, yield stress, and fragility of an electro-rheological suspension. *Rheologica Acta*, 41:265–275, 2002.

[11] Young Gun Ko and Ung Su Choi. Gelation of natural polymer dispersed suspensions under electric field. *Soft Matter*, 8:253–259, 2012.

[12] E Paineau, K Antonova, C Baravian, I Bihannic, P Davidson, I Dozov, M Impéror-Clerc, P Levitz, A Madsen, F Meneau, et al. Liquid-crystalline nematic phase in aqueous suspensions of a disk-shaped natural beidellite clay. *The Journal of Physical Chemistry B*, 113(48):15858–15869, 2009.

[13] Paramesh Gadige and Ranjini Bandyopadhyay. Electric field induced gelation in aqueous nanoclay suspensions. *Soft matter*, 14 34:6974–6982, 2018.

[14] Yun Tan, Ronglan Wu, Huili Li, Wenchen Ren, Juan Du, Shimei Xu, and Jide Wang. Electric field-induced gradient strength in nanocomposite hydrogel through gradient crosslinking of clay. *Journal of Materials Chemistry B*, 3(21):4426–4430, 2015.

[15] Barbara Ruzicka and Emanuela Zaccarelli. A fresh look at the laponite phase diagram. *Soft Matter*, 7:1268–1286, 2011.

[16] Samim Ali and Ranjini Bandyopadhyay. Use of ultrasound attenuation spectroscopy to determine the size distribution of clay tactoids in aqueous suspensions. *Langmuir*, 29(41):12663–12669, 2013.

[17] Hajime Tanaka, Jacques Meunier, and Daniel Bonn. Nonergodic states of charged colloidal suspensions: Repulsive and attractive glasses and gels. *Physical Review E*, 69(3):031404, 2004.

[18] Jan Gieseler, Juan Ruben Gomez-Solano, Alessandro Magazzù, Isaac Pérez Castillo, Laura Pérez García, Marta Gironella-Torrent, Xavier Viader-Godoy, Felix Ritort, Giuseppe Pesce, Alejandro V Arzola, et al. Optical tweezers—from calibration to applications: a tutorial. *Advances in Optics and Photonics*, 13(1):74–241, 2021.

[19] AR Khan and JF Richardson. The resistance to motion of a solid sphere in a fluid. *Chemical Engineering Communications*, 62(1-6):135–150, 1987.

[20] MM Ramos-Tejada, FJ Arroyo, and AV Delgado. Negative electrorheological behavior in suspensions of inorganic particles. *Langmuir*, 26(22):16833–16840, 2010.

[21] Ajay Singh Negi, Kheya Sengupta, and AK Sood. Frequency-dependent shape changes of colloidal clusters under transverse electric field. *Langmuir*, 21(25):11623–11627, 2005.

[22] Erwan Paineau, Ivan Dozov, Isabelle Bihannic, Christophe Baravian, Marie-Eve M Krapf, Adrian-Marie Philippe, Stéphan Rouzière, Laurent J Michot, and Patrick Davidson. Tailoring highly oriented and micropatterned clay/polymer nanocomposites by applying an ac electric field. *ACS Applied Materials & Interfaces*, 4(8):4296–4301, 2012.

[23] Hiroshi Kimura, Taiki Sugiyama, Shinya Takahashi, and Akira Tsuchida. Viscosity change in aqueous hectorite suspension activated by dc electric field. *Rheologica Acta*, 52:139–144, 2013.

[24] Chandeshwar Misra, Venketesh T Ranganathan, and Ranjini Bandyopadhyay. Influence of medium structure on the physicochemical properties of aging colloidal dispersions investigated using the synthetic clay laponite®. *Soft Matter*, 17(41):9387–9398, 2021.

Chapter 6

Influence of particle size polydispersity on dynamical heterogeneities in dense particle packings

A molecular system can approach a glassy state if its temperature is lowered rapidly enough that it undergoes dynamical arrest even while its structure remains disordered or liquidlike [1–3]. The temperature at which this transition occurs, commonly referred to as the glass transition temperature, depends on material properties and cooling rate. Changes in dielectric constant, viscosity, and thermodynamic properties like enthalpy, free volume, heat capacity, and thermal expansion coefficient are frequently used to identify the glass transition point [4–6]. Owing to the very small sizes of the constituents of glass forming materials, the length and time scales characterising their structure and dynamics are inaccessible in laboratory experiments. In this context, soft materials such as dense colloidal suspensions, comprising macromolecules that can be likened to scaled up atoms, have been used as model systems [7, 8] to unravel the structural and dynamical properties of glassforming materials. As the sizes of the constituent particles in jammed colloidal suspensions

are many orders larger than those of atoms or molecules, their relaxation processes are amenable to measurement using common laboratory techniques such as bright field and confocal microscopy, dynamic light scattering, etc. [8]. In contrast to a molecular system which can be transformed to a glassy state by a rapid temperature quench, the transition of a dense colloidal system to a glassy state can be achieved by increasing the volume fraction of the dispersed phase (colloidal particles) [9]. Particles near their jamming or glass transition are trapped in cages formed by their neighbours and move in a correlated manner due to cage rearrangements [10]. The progressive slowing down of particle dynamics and simultaneous growth of the characteristic lengthscales associated with cooperatively rearranging particles are ubiquitous near the jamming transition point [11, 12].

The transition of a supercooled liquid to a glassy state is accompanied by a divergence of its relaxation time [13, 14]. Mode coupling theory (MCT) predicts a glass transition in amorphous materials at a volume fraction ≈ 0.516 [15, 16]. Interestingly, experiments show that particle dynamics persist even above the glass transition volume fraction predicted by MCT, with significant slowing down of the dynamics in cooperatively rearranging regions (CRRs) [17]. Molecular dynamics simulations [18, 19] were performed to define a maximally random jammed state and the emergence of rigidity at a volume fraction ≈ 0.64 for monodisperse hard spheres. Glasses are characterised by disorder and metastability which can be sustained only in the presence of size polydispersity [20, 21]. For samples of negligible size polydispersity, a dense system eventually settles in crystalline configurations. The presence of size polydispersity shifts the glass transition point to a particle volume fraction that is higher than that predicted for a monodisperse system [22].

Particle dynamics in a dilute colloidal suspension are purely diffusive and particle displacements are well-characterised by a Gaussian distribution function [23]. Particles in dense colloidal suspensions, in contrast, are trapped in cages constituted by their neighbours. While particle dynamics are restricted within the cage for short observation times, a cage hopping phenomenon facilitated by the coopera-

tive diffusion of particles is ubiquitous for long waiting times [24, 25]. Such particle displacements between cages result in a structural relaxation process characterised by an α-relaxation timescale. The cage-hopping phenomenon breaks the symmetry of particle motion, with the distribution of displacements deviating significantly from Gaussian statistics [26]. Such distributions are often quantified using a non-Gaussian parameter α_2 [27], defined as the ratio of the fourth to second moments of the probability distribution of particle displacements. It has been reported that the time at which the peak in α_2 appears is correlated with the α-relaxation time and sets a timescale for the cooperative diffusion process [25]. Experiments [28, 29] suggest that the peak in α_2 signals the emergence of spatiotemporal heterogeneities in the system.

Dynamical heterogeneities (DHs) have been reported near the jamming transition of various systems such as granular materials, colloidal suspensions, molecular and supercooled liquids, and have been studied using four-point correlation functions [30–32]. The dynamics of a quasi-two-dimensional and bi-disperse dense granular material under cyclic shear were found to be strongly correlated but spatially heterogeneous as its jamming transition was approached [33]. Using a novel method based on local topology [34], the evolution of spatially heterogeneous dynamics and their connection with local structure were studied for a quasi-two-dimensional granular system of air fluidised beads approaching the jamming transition. In another study involving a binary colloidal suspension in a quasi-two-dimensional geometry, it was noted that dynamical heterogeneities grow rapidly during the crystal to glass transition in a process that is accompanied by an abrupt increase in the dynamical correlation length [35]. Fragility, the rate at which a system approaches its glass transition, and the growth of dynamical heterogeneities have been shown to be closely correlated [36, 37]. In fragile colloidal glasses where fragility is determined by particle-scale elasticity, the suspension viscosity and particle relaxation time increase dramatically for a very small change in volume fraction ϕ near the glass transition point [38]. It was reported that fragility is determined by the stiffness and size poly-

dispersity of the constituent particles and on the compressible interactions between them [39]. A theoretical study concluded that fragility of a supercooled liquid decreases with polydispersity [40]. This was verified experimentally for suspensions of soft colloidal glasses [41]. Dynamical heterogeneities imply the existence of different dynamical relaxation rates within a dense system near its glass transition and results in the correlated motion of particles. The extent of heterogeneity is quantified in terms of the number of correlated particles, N_{corr}, which is estimated from the four-point dynamic susceptibility χ_4 [34]. Nonlinear susceptibilities have been computed in theoretical studies to quantify the extents of cooperatively rearranging regions in spin glasses, dense colloidal systems and the Lennard Jones liquid [42–45]. χ_4 exhibits a peak near the α-relaxation time of the particles [46], with the height of the χ_4 peak directly correlated with the average number of particles, N_{corr}, participating in cooperative rearrangements during structural relaxation.

Molecular dynamics simulations have reported that size polydispersity smears out the kinetic arrest of particles in dense packings due to a lubrication effect [40, 47]. In the present chapter, we experimentally investigate the effect of continuous size polydispersity on the correlated motion of particles as their dense packings approach kinetic arrest. To this end, we prepare dense colloidal microgel suspensions by synthesising fluorescent PNIPAM particles characterised by a range of continuous size polydispersities. We control the polydispersity index (PDI), defined as the ratio of the the standard deviation to the mean of a Gaussian particle size distribution, by controlling reaction rates during particle synthesis. The evolution of particle dynamics with time is observed by tracking individual particles using a confocal microscope. The growth of DHs in these polydisperse systems are quantified by calculating four-point dynamic susceptibility functions, χ_4 [45], as a function of time t. Our measurements provide detailed information on the effect of particle polydispersity on the relaxation dynamics, spatiotemporal heterogeneity, and number of correlated particles in cooperatively rearranging regions in disordered materials approaching their dynamically arrested states. We also demonstrate that increas-

ing temperature and suspension dilution result in the disappearance of dynamical heterogeneities. Finally, we perform molecular dynamics simulations and compute N_{corr} for crowded packings of particles having continuous size polydispersity. We show that these numerical results match our experimental results very well.

6.1 Materials and methods

In this work we have used fluorescent PNIPAM particles. The synthesis process is discussed in section 2.1.3 of Chapter 2. The values of the flow rates that are used to synthesize particle batches of distinct size polydispersities of PNIPAM particles are reported in Table.6.1. Below the LCST, PNIPAM particles swell by absorbing water and have a poor refractive index mismatch with the surrounding water medium. It is therefore not possible to distinguish individual PNIPAM particles in brightfield microscopy. We therefore attach fluorescein dye to PNIPAM particles as discussed in section 2.1.3 and image the fluorescent PNIPAM particles using a Leica TCS SP8 confocal microscope. The attached dye is excited using a 488 nm Argon laser and a photo multiplier tube is used as a detector to record the output signal of higher wavelength. We perform XY directional scanning of dense PNIPAM suspensions loaded in a sample cell constructed using a glass slide and a #1 coverslip, separated by two #0 coverslips as shown in section 2.1.2 of Chapter 2. After loading the sample, UV glue was used to block the open ends of the sample cell which was kept inside a temperature-controlled enclosure box and imaging was performed using a Nikon 100x oil immersion objective lens of numerical aperture NA = 1.4. All experiments were performed in the temperature range 25°C - 31°C which lies below the lower critical solution temperature (LCST) of PNIPAM where the average sizes of the swollen particles do not change appreciably, as discussed in section 1.7 of Chapter 1.

PDI (%)	Flow rate (ml/min)
13.62	0.8
22.20	0.6
20.18	0.7
45.26	0.5

Table 6.1: The flow rate of the solution of reaction ingredients during synthesis of PNIPAM particles to achieve various size distributions (PDIs).

6.2 Results and Discussion

6.2.1 Experimental Results

Aqueous suspensions of fluorescent PNIPAM particles are loaded in the sample cell and imaged in two dimensions using a confocal microscope. Confocal images are obtained using a green laser (wavelength 488 nm). The depth of field of the setup is estimated to be around 135 nm. The imaging plane is fixed at $6-8\ \mu m$ above the lower coverslip to avoid any wall effects. Images of different batches of PNIPAM particles in suspension, synthesised by varying the flow rates of the reaction ingredients, are analysed to calculate particle size distributions or particle size polydispersity indices (PDI). For PDI calculation, we have used a suspension of intermediate particle number density so that the edges of individual particles can be detected accurately. The confocal images are then analysed using ImageJ to calculate particle diameters. The distributions of particle diameters (hollow symbols in Fig.6.1) are fitted using Gaussian functions (solid lines in Fig.6.1). From the fitted parameters, the PDIs of particles synthesised in different batches are calculated as percentages using the formula, $\text{PDI} = 100 * W/M$ where W is the width and M is the mean of the fitted Gaussian distribution. To compute the dynamics, image sequences are acquired for 3-4 mins at 0.679 frames/sec, and 1000 PNIPAM particles from the central region

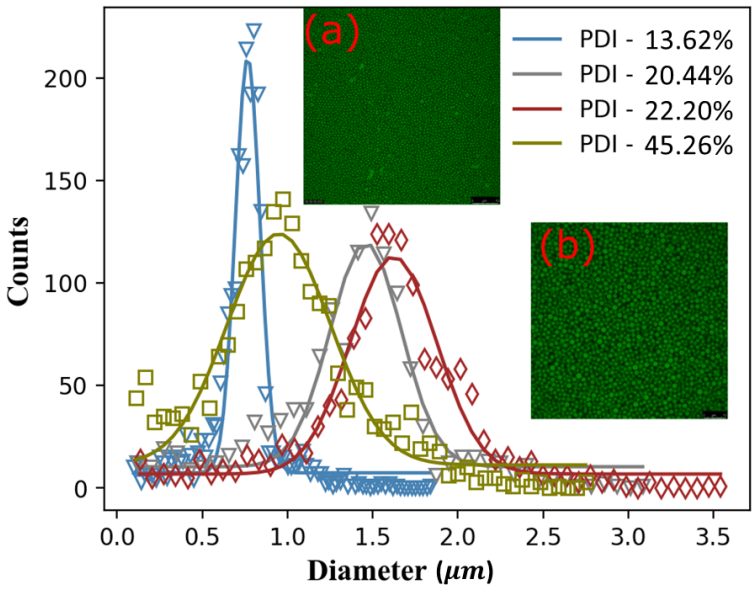

Figure 6.1: The hollow symbols denote histogram plots of the diameter distributions of PNIPAM particles obtained from different synthesis batches. The solid curves are fits to Gaussian functions whose widths and heights are used to calculate the size polydispersity indices (PDIs) of the PNIPAM particles. The insets show confocal images of dense suspensions having PDIs (a) 13.62% and (b) 22.20%.

of the images are tracked using a video spot tracker software (Computer Integrated Systems for Microscopy and Manipulation) [48]. Particles within the plane of interest are monitored for a specific duration. If a particle moves beyond this plane during the experiment, further tracking of that particle was not performed. We have calculated the area fractions, A_p, of PNIPAM particles in suspension for different batches by binarising two dimensional images after setting appropriate intensity threshold values such that individual particles could be distinguished from the background. All analyses and numerical calculations are performed using Python 3.10 (Jupyter notebook). The mean square displacements (MSDs) of PNIPAM particles in suspension are computed to estimate their average dynamics for different particle area fractions A_p, particle PDIs, and medium temperatures using the formula:

$$\langle \Delta r^2(t) \rangle = \frac{1}{N} \sum_i \langle (x_i(t_0 + t) - x_i(t_0))^2 + (y_i(t_0 + t) - y_i(t_0))^2 \rangle_{t_0} \qquad (6.1)$$

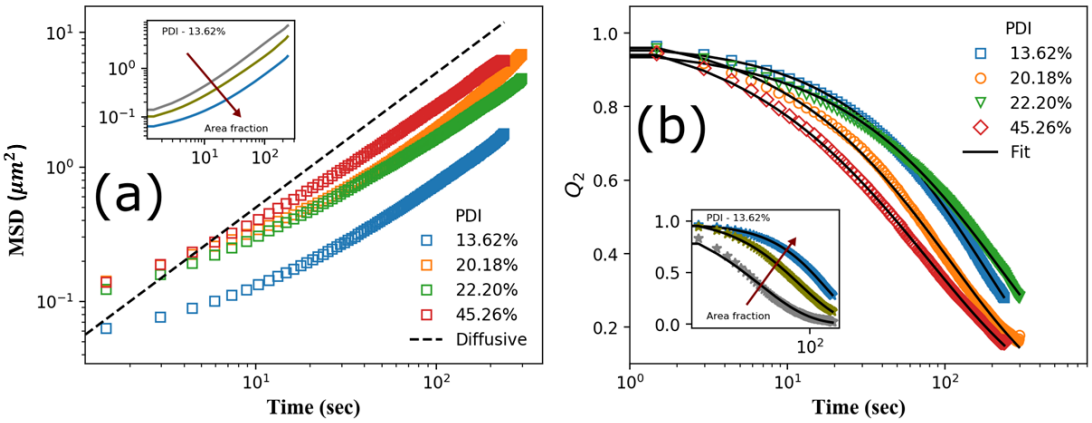

Figure 6.2: (a) Mean square displacements (MSDs) are plotted *vs.* time for dense PNIPAM suspensions constituted by particles of different PDIs at suspension area fraction $A_p \approx 0.65$. The black dashed line represents diffusive dynamics. In the inset, MSD is plotted for PNIPAM suspensions comprising particles of PDI = 13.62% for different area fractions (the arrow indicates increasing area fraction). (b) Two-point density correlation functions, Q_2 are plotted *vs.* time for suspensions of different particle PDIs at a fixed area fraction ($A_p = 0.65$). Q_2 plots for PNIPAM suspensions of different area fractions (0.52, 0.59, 0.65) for a fixed particle PDI = 13.62% are shown in the inset.

Here, t represents the delay time while t_0 denotes the initial time of measurement of a particle trajectory. x_i and y_i are the coordinates of the i-th particle, N is the total number of particles ($N \approx 1000$), and $\langle\rangle$ is an average over t_0.

It is well known that particles in dense suspension have restricted motion due to their confinement in cages constituted by the presence of their neighbours [49]. Cage reorganisation events are characterised by cooperative diffusion [50]. We calculate two-point density correlation functions (Q_2) and four-point susceptibilities (χ_4) to characterise the relaxation timescales and heterogeneous (correlated) dynamics in dense suspensions by using the following relations [33]:

$$Q_i(a, t, t_0) = \exp\left(-\frac{\Delta r_i^2(t_0, t_0 + t)}{2a^2}\right) \tag{6.2}$$

$$Q_2(a, t) = \frac{1}{N}\sum_i \langle Q_i(a, t, t_0)\rangle_{t_0} \tag{6.3}$$

$$\chi_4(a,t) = N(\frac{1}{N}\sum_i \langle Q_i(a,t,t_0)^2\rangle_{t_0} - \frac{1}{N}\sum_i \langle Q_i(a,t,t_0)\rangle_{t_0}^2) \tag{6.4}$$

Experiment			Simulation		
PDI (%)	Area fraction (%)	Optimal probe length (a^*) (μm)	PDI (%)	Volume fraction (%)	Optimal probe length (a^*)
13.62	65.52	0.41	13.06	62.30	0.28
13.62	59.45	0.49	17.37	62.30	0.32
13.62	53.32	0.26	21.77	62.30	0.33
22.20	66.09	0.72	38.67	62.30	0.38
20.18	65.24	0.57			
45.26	65.70	0.57			

Table 6.2: The optimal probe lengths, a^*, used for analyses of both experiments and simulations, are tabulated for suspensions of different PDIs and packing fractions.

where $\Delta r_i(t_0, t_0+t)$ is the displacement of the i-th particle over delay time t from the initial time t_0, a is a probe length that is used to set the extent of the dynamical heterogeneity of the dense suspension and N is the total number of particles. In Eqn.6.2, the exponential form arises from the calculation of a spatial overlap function as outlined in an earlier work [33]. If the displacement $\Delta r_i(t_0, t_0+t)$ of the i-th particle is less than the probe length a, Q_i (Eqn.6.2) will be close to 1, while for displacements larger than a, Q_i will be closer to 0. We calculate Q_2 using Eqn.6.3 by averaging Q_i over all particles and initial times t_0.

MSDs are determined *vs.* delay time t (Fig.6.2(a)) for PNIPAM particles characterised by four distinct PDI values, that were prepared in dense aqueous suspension at a high particle area fraction ($A_p \approx 0.65$). MSD data for particles having a fixed PDI ($= 13.62\%$) and prepared in suspensions of varying area fractions, A_p are shown in the inset. The observed enhancement in MSDs with increasing PDI indicates suspension unjamming or fluidisation, and is reminiscent of earlier results [47]. Furthermore, we see from the inset of Fig.6.2(a) that the calculated MSDs decrease with

increase in particle area fraction due to constrained particle motion in increasingly jammed environments. Increasing suspension area fraction and decreasing particle PDI therefore have analogous effects on suspension jamming. From Fig.6.2(a), we note the emergence of a very weak plateau in the MSD at very low delay times for lower particle PDI values, presumably arising from constrained particle dynamics due to the caging effect [24]. The MSD increases at later times, and approaches a line of slope 1 ($\Delta r^2(t) \propto t$ marked by a dashed line), which indicates diffusive dynamics presumably due to a cage escape process. We see that the extent of the plateau in the MSD reduces with increase in PDI and decrease in area fraction, again pointing to the enhanced fluidisation of the system under these conditions.

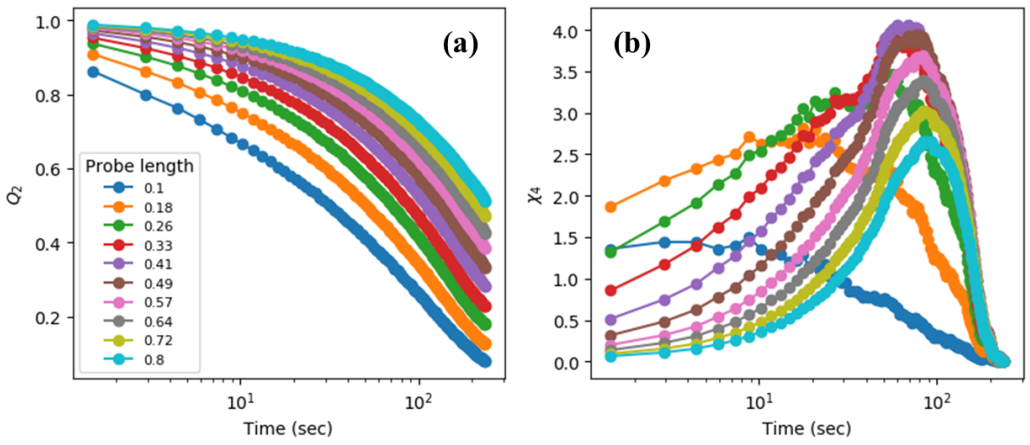

Figure 6.3: (a) Q_2 is plotted for different probe lengths a in μm (shown in the legend) for suspensions of PNIPAM particles of PDI 13.62%, prepared at an area fraction of 0.65. (b) The corresponding χ_4 *vs.* time is plotted.

We see from Fig.6.2(b) that Q_2 decays faster with increase in particle PDI for an approximately constant area fraction $A_p \approx 0.65$. We simultaneously note from the inset of Fig.6.2(b) that for a fixed low particle PDI of 13.62%, Q_2 relaxes faster with decreasing area fraction A_p. The values of Q_2 and χ_4 computed for different probe lengths, a, for data acquired from a dense sample corresponding to $A_p = 0.65$ and

Table 6.3: Parameters extracted from fits of stretched exponential functions to Q_2, shown as black lines in Fig.6.2(b) and in the inset of Fig.6.5(b). Along with the fitted parameters, we have also tabulated the peak values of χ_4, plotted in Figs.6.4(a) and 6.5(b), for experiments and simulations.

Experimental				*Simulation*			
PDI	τ (sec)	β	χ_4^*	PDI	τ (steps)	β	χ_4^*
13.62%	181.81 ± 0.45	0.80 ± 0.003	4.06	13.06%	2211.65 ± 16.08	0.70 ± 0.005	4.35
20.18%	111.43 ± 0.91	0.67 ± 0.005	1.81	17.37%	790.80 ± 6.78	0.59 ± 0.003	2.26
22.20%	229.56 ± 1.13	0.70 ± 0.005	1.80	21.77%	229.75 ± 4.31	0.58 ± 0.006	1.33
45.26%	80.44 ± 0.42	0.60 ± 0.002	0.82	38.67%	156.63 ± 3.14	0.55 ± 0.006	0.41

PDI = 13.62% are displayed in Fig.6.3. As expected, Q_2 relaxes at a faster rate for shorter probe lengths. As probe length increases, the decay times of the two-point correlation functions become slower. For the subsequent analyses, we set the probe length to an optimal value a^* (shown in Table.6.2), such that the fluctuation of Q_2 or the peak value of χ_4 is maximum. Spatial heterogeneities are expected to be maximum at the length scale corresponding to a^* [33, 34].

We fit the two-point correlation data with stretched exponential functions, $Q_2 = A\exp\left(-(t/\tau)^{\beta}\right)$ [51] to compute the characteristic decay times τ. In the expression for Q_2, A is a prefactor and β is a stretching exponent. The fitted parameters τ and β are displayed in Table 6.3. We note again from the values of τ that the relaxation process speeds up significantly with increase in particle PDI. The four-point susceptibility, χ_4, can be interpreted as a measure of the spatio-temporal variation of Q_2. By computing four-point susceptibility functions χ_4 using Eqn.6.4, we systematically study the extent of spatio-temporal heterogeneities in dense PNIPAM suspensions of different area fractions, constituted by particles of different PDIs. In Fig.6.4(a), χ_4 is plotted for the optimal probe length a^*, evaluated as described earlier and tabulated in Table.6.3, for suspensions characterised by different PDIs and area fractions A_p. Using the same analysis protocol, we show that the peak value of χ_4 decreases with temperature for fixed three different temperatures at a

PDI and area fraction. The data is plotted in Fig.6.4(b).

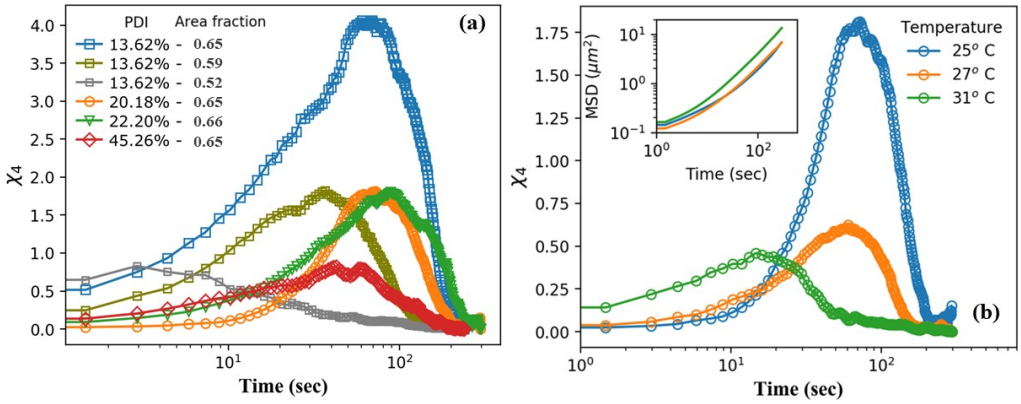

Figure 6.4: (a) χ_4 is plotted *vs.* time for a probe length a^* at which the peak height is maximum for dense PNIPAM suspensions of different size polydispersities (PDIs) and area fractions A_p. (b) χ_4 decreases as temperature increases for PNIPAM suspensions of area fraction = 0.65, constituted by particles of PDI = 20.18%. Simultaneously, we see from the inset that particle MSDs increase with increase in temperature.

It has been reported that the time scales corresponding to the peak positions of χ_4 are comparable to the α-relaxation time scales of supercooled liquids [52]. By combining the data plotted in Fig.6.4(a) and Fig.6.4(b), we see that the χ_4 peak becomes weaker as suspension A_p is decreased and as particle PDI and sample temperature are increased. Decrease in χ_4 indicates a loss of correlation at different spatio-temporal locations. The observed fluidisation of the sample with increasing dilution, achieved by decreasing suspension area fraction, is consistent with the predictions of the jamming phase diagram [53]. When sample temperature is raised, the accelerated motion of PNIPAM particles results in suspension unjamming (Fig.6.4(b)). Furthermore, we note from Fig.6.4(a) that an increase in PDI enhances the lubrication effect as described in earlier reports [40, 47] and also results in suspension unjamming.

6.2.2 Molecular dynamics simulation

We next verify our experimental results by numerically studying the effect of particle size polydispersity on the dynamics of dense suspensions. We model inter-particle

interactions using a Lennard Jones potential, $V_{LJ}(r) = 4\epsilon[(\sigma/r)^{12} - (\sigma/r)^6]$ where ϵ is the dispersion energy and σ is the minimum centre-centre distance between particles at which the potential is zero. The Lennard-Jones potential is well known and extensively used for studying supercooled colloidal suspensions and their glass transitions [54]. This interaction is different from the experimental counterpart discussed previously and is used for ease of computation. However, the main aim of this work was to study the effect of size polydispersity on the dynamical heterogeneity and compare the results qualitatively. Polydispersity in size is introduced by incorporating a normally distributed function having mean = 0 and standard deviation = 1. In this work, the distribution of sizes (D_i) of 50000 particles is defined as $D_i = 1 + \frac{PDI}{100} * ND$, where ND is the normal distribution function. The tails of the distribution are removed to exclude the biggest and smallest particles.

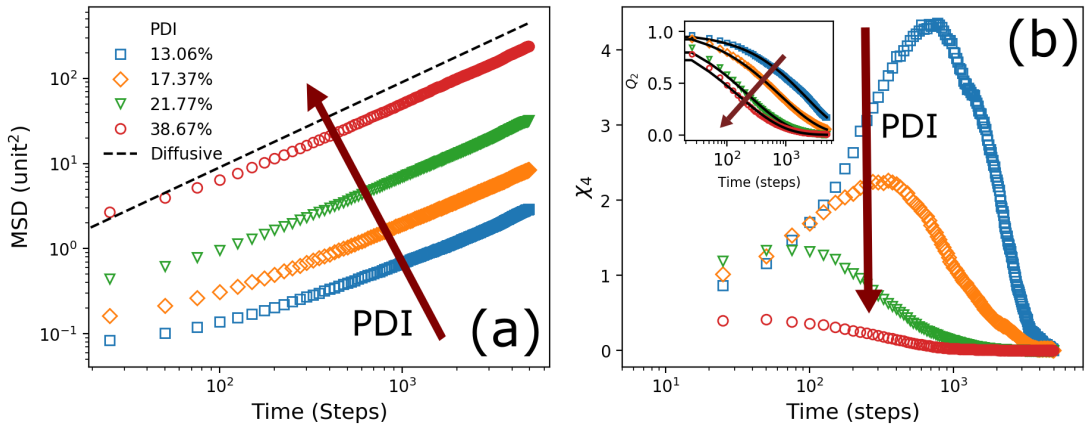

Figure 6.5: (a) Mean square displacements, MSDs, of the simulated particles *vs.* time, shown for different particle PDI values for volume fraction $\phi = 0.6230$. (b) Four-point susceptibilities, χ_4, *vs.* time for distinct polydispersity indices ($\phi = 0.6230$). In the inset, the corresponding two-point correlation functions, Q_2, are shown.

In the molecular dynamics (MD) simulations, the systems are equilibrated at high temperature to avoid artefacts arising from the initial arrangement of particle positions that is selected. The MD simulations are performed for microcanonical ensembles by fixing the volume fraction, ϕ, at 0.6230 ± 0.0005 for a system with $N = 50000$ particles and for particle PDI values 13.06%, 17.37%, 21.77% and 38.67%. The temperature is fixed at 0.9 (Lennard-Jones unit) for the simulations

reported here for particles with varying PDI values. We select seven different regions from the system, each having 1000 particles. MSD, Q_2 and χ_4 are next calculated while averaging over the seven regions comprising 1000 particles each to ensure adequate statistics and maximum overlap with experimental conditions. In Fig.6.5(a), the simulated mean square displacements are plotted for dense suspensions and for different particle PDIs. We see that the computed MSD values increase for samples with higher particle PDIs, thereby verifying our experimental result that higher PDIs enhance the fluidisation of jammed suspensions. Furthermore, as pointed out from the experimental data, caging effects are more prominent for lower particle PDIs at initial times. Next, four-point correlation functions are plotted *vs.* time in Fig.6.5(b) corresponding to the optimal probe length a^*. As in the experiments, a^* is chosen independently for each sample and represents the value of a at which the peak height of χ_4 is maximum (Table.6.2). We note that heights of χ_4 reduce and shift to earlier times for particle assemblies characterised by higher PDIs. In results that are consistent with our experimental observations, we note that dynamical heterogeneities are most significant in dense suspensions characterised by lower particle PDIs. Two-point self correlation functions, Q_2, are plotted in the inset of Fig.6.5(b) for optimal probe length values a^*, for several particle PDIs. Furthermore, we note from the inset of Fig.6.5(b) that the two-point correlation functions Q_2 computed from MD simulations decay faster as PDI is increased at a fixed area fraction. These results are consistent with the conclusions of the experiments reported earlier. We have also performed simulations by varying temperatures (T = 0.8, 0.9 and 1.0) and volume fractions (ϕ = 0.6170, 0.6200 and 0.6230) for the lowest PDI. We note from Figs.6.6(a) and (b) that the speeding up of particle dynamics with increasing temperature and decreasing volume fraction is evident from the MSDs computed from MD simulations. We simultaneously observe a decrease in the extent of dynamical heterogeneities in dense samples with increase in temperature and decrease in volume fraction, as indicated by the reduction in the height of the χ_4 peak in Figs.6.6(c) and (d).

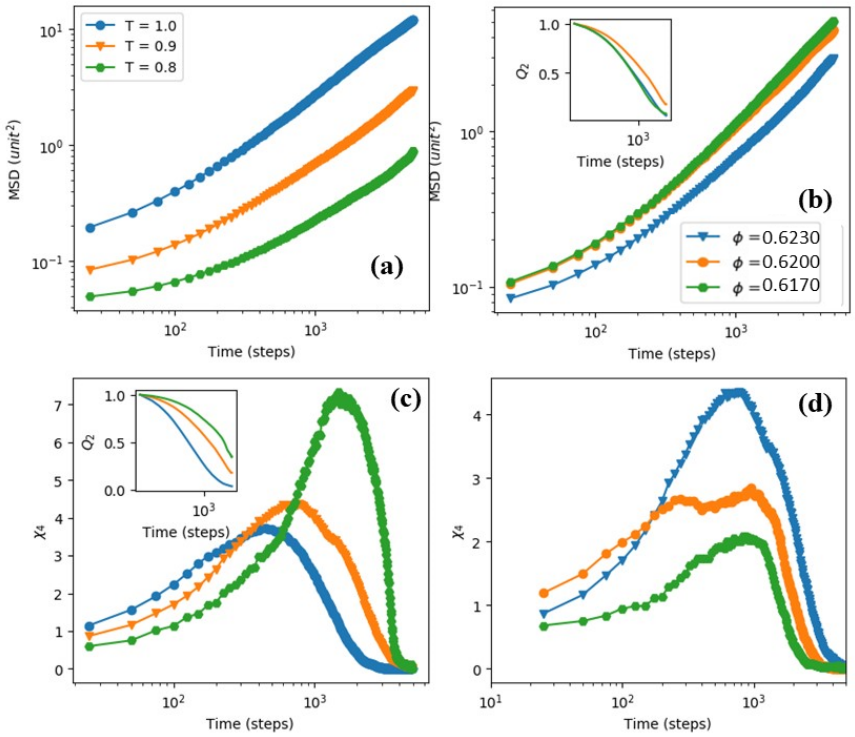

Figure 6.6: (a) MSDs extracted from MD simulations are plotted *vs.* time steps for three different temperatures 0.8, 0.9 and 1 at volume fraction 0.6230. (b) MSDs *vs.* time steps for different volume fractions and Q_2 is shown in the inset for T = 0.9. (c) χ_4 is shown for the same temperatures as in (a) and volume fraction 0.6230 and Q_2 is shown in the inset. (d) χ_4 is shown for the same volume fractions as in (b) at T = 0.9.

In order to estimate the characteristic lengthscales of these cooperatively rearranging regions in dense polydisperse suspensions, the number of correlated particles are estimated from the following equation [34],

$$N_{corr} = \frac{\chi_4^*}{1 - Q_2^*} \tag{6.5}$$

where χ_4^* is the peak value of χ_4 and, Q_2^* is the magnitude of Q_2 corresponding to the delay time at which the peak in χ_4 appears. In Fig.6.7, we plot the number of correlated particles, extracted using Eqn 6.5, computed from both experiments and simulations. N_{corr} is observed to decrease with increasing PDI. It is well known that the random close packing fraction of a suspension shifts towards higher volume fraction with increasing size polydispersity [22]. Polydisperse particles can pack more

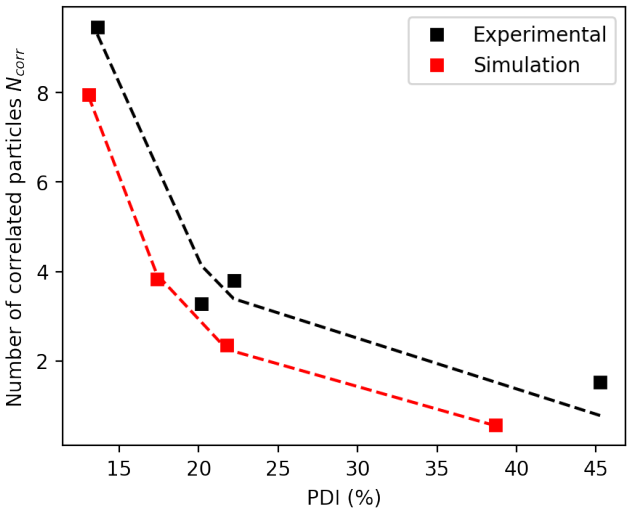

Figure 6.7: Number of correlated particles in cooperatively rearranging regions (CRRs), obtained from experiments (black) and simulations (red), are plotted for different particle PDIs for dense suspensions.

compactly when compared to monodisperse particles, with small particles filling the voids between big particles. Due to the presence of several small particles in a suspension with continuous size polydispersity, the dynamics remain fluid-like even for a high volume fraction at which monodisperse systems are expected to jam [21]. While both experiments and simulations show a good match in Fig.6.7, with N_{corr} values observed to decrease monotonically with particle PDI, we note that the small differences in the calculated values of N_{corr} can arise due to the different geometries used in experiments (2-D) and simulations (3-D). Additionally, the colloidal particles used in experiments bear positive charges, while the simulation algorithm uses a Lennard Jones potential. In spite of these factors, we can safely conclude that jammed suspensions can be fluidised by increasing the particle polydispersity index and sample temperature, and by decreasing concentration. For large particle PDIs, therefore, the small particles of higher mobilities can effectively enhance the lubrication effect. Furthermore, increase in temperature and dilution also contribute to increasing the mobilities of all particles, thereby accelerating the average dynamics of the suspension. Finally, based on our observations, we propose a new phase diagram to highlight the jamming to unjamming transition of dense suspensions. While

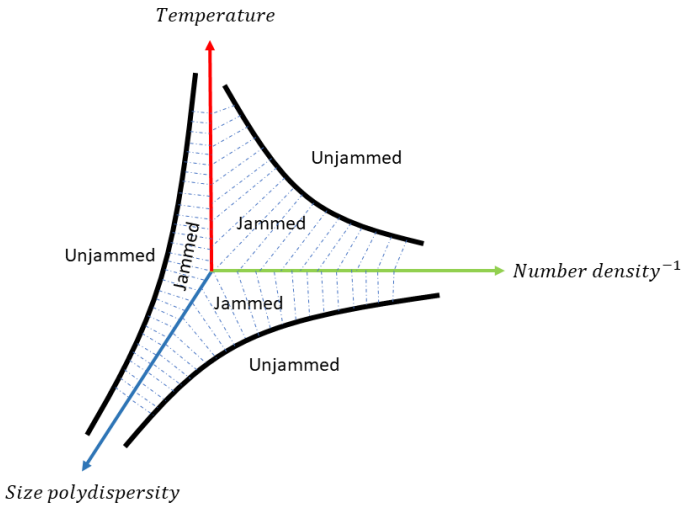

Figure 6.8: A three-dimensional phase diagram depicting jamming to unjamming transitions in dense suspensions for increase in temperature and particle size polydispersity, and for decrease in number density. The jammed region (blue dashed lines) lies around the origin. Arbitrary black solid lines are drawn to visualise the jamming to unjamming transition, achieved by appropriately changing temperature, particle number density or size polydispersity.

fluidisation by increase in temperature, decrease in packing fraction and increase in polydispersity have been discussed earlier works [53, 55, 56], our work systematically studied unjamming due to correlated motion and dynamical heterogeneity in systems comprising particles of different size polydispersities. Our three-dimensional jamming-unjamming phase diagram, displayed in Fig.6.8, includes the enhancement of particle polydispersity as an alternate route to achieve unjamming.

6.3 Conclusions

Using particle tracking experiments and molecular dynamics simulations, we observe the presence of dynamically heterogeneous regions in dense PNIPAM suspensions for low particle polydispersity indices (PDIs) and at low temperatures [57]. The present work reports a combined experimental and numerical study of the dynamics of jammed states comprising particles having continuous size distributions. We com-

pute mean square displacements to estimate the average dynamics of the particles in their dense suspensions and extract multipoint correlation functions to characterise their heterogeneous dynamics. Weakening of particle caging with increase in PDI is evident from our analyses. The faster dynamics of the smaller particles in dense systems facilitate accelerated cage rearrangements and reduce cage-breaking timescales, thereby speeding up structural relaxation. The dynamics are expected to be maximally heterogeneous at the timescale of the structural relaxation process due to the large non-Gaussian displacements of a small fraction of constituent particles during the cage rearrangement process [26, 29]. We report that for dense colloidal suspensions with high PDIs, the presence of a wide range of particle sizes strongly affects cage trapping and cage breaking events and, consequently, the characteristic timescales associated with particle dynamics in crowded environments.

The spatiotemporal heterogeneities in dense suspensions are monitored here by changing the particle area fraction A_p (in experiments) or volume fraction ϕ (in simulations) at a fixed PDI, and by changing particle PDIs at a fixed A_p or ϕ. The effect of temperature on dynamical heterogeneities is also studied using both experiments and simulations. The time- and lengthscales associated with spatiotemporal heterogeneities are extracted from four-point correlation functions, χ_4. The growth of correlations is much stronger for suspensions constituted by particles having narrower size distributions. The presence of heterogeneous and correlated dynamics in dense suspensions, as shown by us via careful experiments and molecular dynamics simulations, points to the analogous natures of the jamming and glass transitions. Despite the distinct natures of the interaction potentials and boundary conditions employed for the experiment and simulation, the observed results exhibit a notable similarity. An increase in the number of particles undergoing correlated motion for suspensions characterised by lower PDIs indicates the existence of a growing lengthscale and critical-like dynamics [58, 58] during the kinetic arrest phenomenon. Besides demonstrating the disappearance of correlated and heterogeneous particle dynamics with increasing particle size distributions, we also demonstrate the de-

crease in heterogeneous dynamics with increase in dilution and temperature. It would be interesting to perform further confocal experiments to study the kinetic arrest phenomenon. One such open question would be to unravel the influence of local order on the emergence and disappearance of dynamical heterogeneities.

Bibliography

[1] Wolfgang Gotze and Lea Sjogren. Relaxation processes in supercooled liquids. *Reports on Progress in Physics*, 55(3):241, 1992.

[2] C Austen Angell. Formation of glasses from liquids and biopolymers. *Science*, 267(5206):1924–1935, 1995.

[3] Ludovic Berthier and Giulio Biroli. Theoretical perspective on the glass transition and amorphous materials. *Reviews of Modern Physics*, 83(2):587, 2011.

[4] Richard S Stearns, IN Duling, and Robert H Johnson. Relationship of glass transition temperature to viscosity-temperature characteristics of lubricants. *Industrial & Engineering Chemistry Product Research and Development*, 5(4):306–313, 1966.

[5] Z Černošek, J Holubová, E Černošková, and M Liška. Enthalpic relaxation and the glass transition. *Journal of Optoelectronics and Advanced Materials*, 4:489–503, 2002.

[6] Ronald P White and Jane EG Lipson. Polymer free volume and its connection to the glass transition. *Macromolecules*, 49(11):3987–4007, 2016.

[7] S Marcelja, DJ Mitchell, and BW Ninham. Phase transitions in aqueous suspensions of spherical colloid particles. *Chemical Physics Letters*, 43(2):353–357, 1976.

[8] PN Pusey. Colloidal glasses. *Journal of Physics: Condensed Matter*, 20(49):494202, 2008.

[9] Peter N Pusey and William van Megen. Observation of a glass transition in suspensions of spherical colloidal particles. *Physical Review Letters*, 59(18):2083, 1987.

[10] Eric R Weeks and DA Weitz. Properties of cage rearrangements observed near the colloidal glass transition. *Physical Review Letters*, 89(9):095704, 2002.

[11] Debasish Saha, Yogesh M Joshi, and Ranjini Bandyopadhyay. Investigation of the dynamical slowing down process in soft glassy colloidal suspensions: comparisons with supercooled liquids. *Soft Matter*, 10(18):3292–3300, 2014.

[12] Paramesh Gadige, Debasish Saha, Sanjay Kumar Behera, and Ranjini Bandyopadhyay. Study of dynamical heterogeneities in colloidal nanoclay suspensions approaching dynamical arrest. *Scientific Reports*, 7(1):8017, 2017.

[13] Elisa Tamborini, C Patrick Royall, and Pietro Cicuta. Correlation between crystalline order and vitrification in colloidal monolayers. *Journal of Physics: Condensed Matter*, 27(19):194124, 2015.

[14] Rajesh K Murarka and Biman Bagchi. Diffusion and viscosity in a supercooled polydisperse system. *Physical Review E*, 67(5):051504, 2003.

[15] Wolfgang Götze. *Complex dynamics of glass-forming liquids: A mode-coupling theory*, volume 143. Oxford University Press, USA, 2009.

[16] Liesbeth MC Janssen. Mode-coupling theory of the glass transition: A primer. *Frontiers in Physics*, 6:97, 2018.

[17] Giovanni Brambilla, Djamel El Masri, Matteo Pierno, Ludovic Berthier, Luca Cipelletti, George Petekidis, and Andrew B Schofield. Probing the equilibrium dynamics of colloidal hard spheres above the mode-coupling glass transition. *Physical Review Letters*, 102(8):085703, 2009.

[18] Vasili Baranau and Ulrich Tallarek. Random-close packing limits for monodisperse and polydisperse hard spheres. *Soft Matter*, 10(21):3826–3841, 2014.

[19] Corey S O'hern, Leonardo E Silbert, Andrea J Liu, and Sidney R Nagel. Jamming at zero temperature and zero applied stress: The epitome of disorder. *Physical Review E*, 68(1):011306, 2003.

[20] Stefan Auer and Daan Frenkel. Suppression of crystal nucleation in polydisperse colloids due to increase of the surface free energy. *Nature*, 413(6857):711–713, 2001.

[21] M Hermes and M Dijkstra. Jamming of polydisperse hard spheres: The effect of kinetic arrest. *Europhysics Letters*, 89(3):38005, 2010.

[22] W Schaertl and H Sillescu. Brownian dynamics of polydisperse colloidal hard spheres: Equilibrium structures and random close packings. *Journal of Statistical Physics*, 77(5):1007–1025, 1994.

[23] Hans Sonntag, Klaus Strenge, Hans Sonntag, Klaus Strenge, and B Vincent. Structure formation in disperse systems. In *Coagulation Kinetics and Structure Formation*, pages 127–182. Springer New York, NY, 1987.

[24] Gary L Hunter and Eric R Weeks. The physics of the colloidal glass transition. *Reports on Progress in Physics*, 75(6):066501, 2012.

[25] Andreas Kasper, Eckhard Bartsch, and Hans Sillescu. Self-diffusion in concentrated colloid suspensions studied by digital video microscopy of core- shell tracer particles. *Langmuir*, 14(18):5004–5010, 1998.

[26] Erica J Saltzman and Kenneth S Schweizer. Non-gaussian effects, space-time decoupling, and mobility bifurcation in glassy hard-sphere fluids and suspensions. *Physical Review E*, 74(6):061501, 2006.

[27] Alice L Thorneywork, Dirk GAL Aarts, Jürgen Horbach, and Roel PA Dullens. On the gaussian approximation in colloidal hard sphere fluids. *Soft Matter*, 12(18):4129–4134, 2016.

[28] Bhanu Prasad Bhowmik, Indrajit Tah, and Smarajit Karmakar. Non-gaussianity of the van hove function and dynamic-heterogeneity length scale. *Physical Review E*, 98(2):022122, 2018.

[29] M Scott Shell, Pablo G Debenedetti, and Frank H Stillinger. Dynamic heterogeneity and non-gaussian behaviour in a model supercooled liquid. *Journal of Physics: Condensed Matter*, 17(49):S4035, 2005.

[30] Raphael Candelier, Olivier Dauchot, and Giulio Biroli. Building blocks of dynamical heterogeneities in dense granular media. *Physical Review Letters*, 102(8):088001, 2009.

[31] Claudio Maggi, Roberto Di Leonardo, Giancarlo Ruocco, and Jeppe C Dyre. Measurement of the four-point susceptibility of an out-of-equilibrium colloidal solution of nanoparticles using time-resolved light scattering. *Physical Review Letters*, 109(9):097401, 2012.

[32] Claudio Donati, Silvio Franz, Sharon C Glotzer, and Giorgio Parisi. Theory of non-linear susceptibility and correlation length in glasses and liquids. *Journal of Non-Crystalline Solids*, 307:215–224, 2002.

[33] Olivier Dauchot, Guillaume Marty, and Giulio Biroli. Dynamical heterogeneity close to the jamming transition in a sheared granular material. *Physical Review Letters*, 95(26):265701, 2005.

[34] Adam Ross Abate and DJ Durian. Topological persistence and dynamical heterogeneities near jamming. *Physical Review E*, 76(2):021306, 2007.

[35] Peter Yunker, Zexin Zhang, and Arjun G Yodh. Observation of the disorder-induced crystal-to-glass transition. *Physical Review Letters*, 104(1):015701, 2010.

[36] Gerold Adam and Julian H Gibbs. On the temperature dependence of cooperative relaxation properties in glass-forming liquids. *The Journal of Chemical Physics*, 43(1):139–146, 1965.

[37] Srikanth Sastry. The relationship between fragility, configurational entropy and the potential energy landscape of glass-forming liquids. *Nature*, 409(6817):164–167, 2001.

[38] Johan Mattsson, Hans M Wyss, Alberto Fernandez-Nieves, Kunimasa Miyazaki, Zhibing Hu, David R Reichman, and David A Weitz. Soft colloids make strong glasses. *Nature*, 462(7269):83–86, 2009.

[39] Pieter Van Der Scheer, Ties Van De Laar, Jasper Van Der Gucht, Dimitris Vlassopoulos, and Joris Sprakel. Fragility and strength in nanoparticle glasses. *ACS Nano*, 11(7):6755–6763, 2017.

[40] Sneha Elizabeth Abraham, Sarika Maitra Bhattacharrya, and Biman Bagchi. Energy landscape, antiplasticization, and polydispersity induced crossover of heterogeneity in supercooled polydisperse liquids. *Physical Review Letters*, 100(16):167801, 2008.

[41] Sanjay Kumar Behera, Debasish Saha, Paramesh Gadige, and Ranjini Bandyopadhyay. Effects of polydispersity on the glass transition dynamics of aqueous suspensions of soft spherical colloidal particles. *Physical Review Materials*, 1(5):055603, 2017.

[42] Jean-Philippe Bouchaud and Giulio Biroli. Nonlinear susceptibility in glassy systems: A probe for cooperative dynamical length scales. *Physical Review B*, 72(6):064204, 2005.

[43] Takayuki Narumi, Scott V Franklin, Kenneth W Desmond, Michio Tokuyama, and Eric R Weeks. Spatial and temporal dynamical heterogeneities approaching the binary colloidal glass transition. *Soft Matter*, 7(4):1472–1482, 2011.

[44] Sharon C Glotzer, Vladimir N Novikov, and Thomas B Schrøder. Time-dependent, four-point density correlation function description of dynamical heterogeneity and decoupling in supercooled liquids. *The Journal of Chemical Physics*, 112(2):509–512, 2000.

[45] N Lačević, Francis W Starr, TB Schrøder, and Sharon C Glotzer. Spatially heterogeneous dynamics investigated via a time-dependent four-point density correlation function. *The Journal of Chemical Physics*, 119(14):7372–7387, 2003.

[46] Elijah Flenner and Grzegorz Szamel. Anisotropic spatially heterogeneous dynamics on the α and β relaxation time scales studied via a four-point correlation function. *Physical Review E*, 79(5):051502, 2009.

[47] Emanuela Zaccarelli, Siobhan M Liddle, and Wilson CK Poon. On polydispersity and the hard sphere glass transition. *Soft Matter*, 11(2):324–330, 2015.

[48] https://cismm.web.unc.edu/. Video spot tracker.

[49] Eric R Weeks and David A Weitz. Subdiffusion and the cage effect studied near the colloidal glass transition. *Chemical Physics*, 284(1-2):361–367, 2002.

[50] Willem K Kegel, van Blaaderen, and Alfons. Direct observation of dynamical heterogeneities in colloidal hard-sphere suspensions. *Science*, 287(5451):290–293, 2000.

[51] Daniel Diaz Vela and David S Simmons. The microscopic origins of stretched exponential relaxation in two model glass-forming liquids as probed by simulations in the isoconfigurational ensemble. *The Journal of Chemical Physics*, 153(23):234503, 2020.

[52] Smarajit Karmakar. An overview on short and long time relaxations in glass-forming supercooled liquids. In *Journal of Physics: Conference Series*, volume 759, page 012008. IOP Publishing, 2016.

[53] Andrea J Liu and Sidney R Nagel. Jamming is not just cool any more. *Nature*, 396(6706):21–22, 1998.

[54] Walter Kob and Hans C. Andersen. Testing mode-coupling theory for a supercooled binary lennard-jones mixture i: The van hove correlation function. *Phys. Rev. E*, 51:4626–4641, May 1995.

[55] Veronique Trappe, V Prasad, Luca Cipelletti, PN Segre, and David A Weitz. Jamming phase diagram for attractive particles. *Nature*, 411(6839):772–775, 2001.

[56] RJ Farris. Prediction of the viscosity of multimodal suspensions from unimodal viscosity data. *Transactions of the Society of Rheology*, 12(2):281–301, 1968.

[57] Michael Heskins and James E Guillet. Solution properties of poly (n-isopropylacrylamide). *Journal of Macromolecular Science—Chemistry*, 2(8):1441–1455, 1968.

[58] Indrajit Tah, Anoop Mutneja, and Smarajit Karmakar. Understanding slow and heterogeneous dynamics in model supercooled glass-forming liquids. *ACS Omega*, 6(11):7229–7239, 2021.

Chapter 7

Dynamical heterogeneities in 2-D granular polydisperse systems

7.1 Introduction

Granular materials are prevalent in everyday life and are used in various industrial applications [1, 2]. Granular matter is the second most abundant substance on Earth, after water. Numerous significant industrial sectors, such as mining, pharmaceuticals, food, agriculture, and cement, employ diverse granular systems to manufacture products. Transporting and processing these systems requires knowledge of flow behaviour and dynamics of the constituent particles [3]. An understanding of the physics of granular systems can boost the output of many industrial sectors. In addition to industrial uses, several geophysical research studies on granular soil systems have been conducted [4, 5]. Landslides and other natural hazards can be predicted by comprehending the flow properties of granular packings. Granular systems show complex flow behaviors depending on the size, shape and roughness of the particles [6, 7]. Depending on the strength of external perturbations, the same granular substance can act as a solid, a liquid, or a gas [5]. The transition from liquid-like to solid-like behaviour due to application of a range of external perturbations is an intriguing topic in soft matter physics [8, 9].

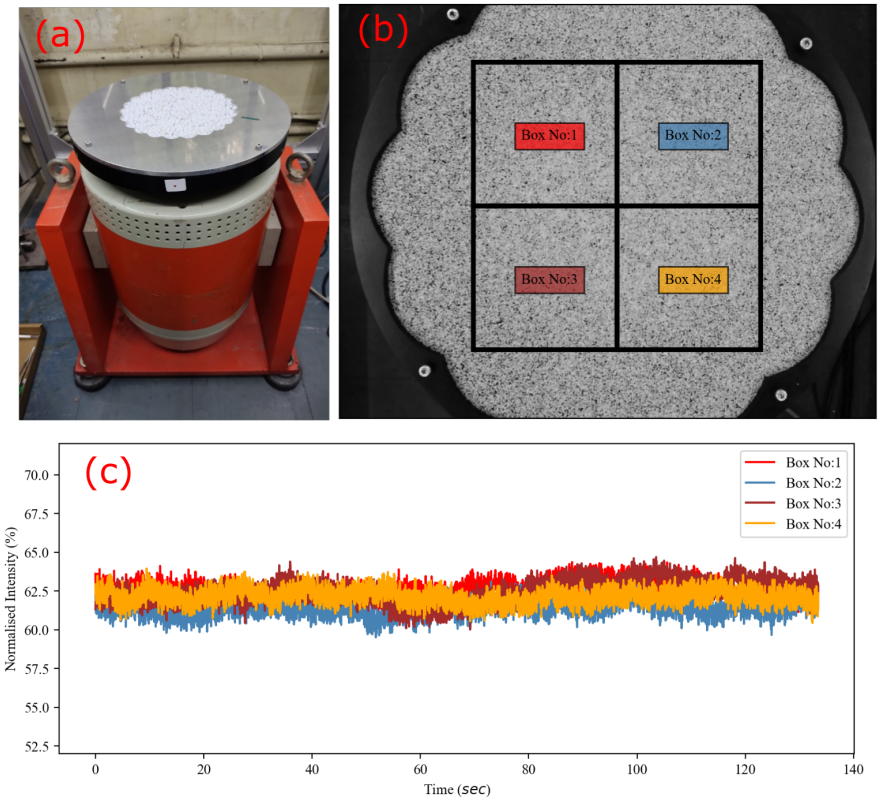

Figure 7.1: (a) Image of electro-dynamic shaker from DESPL(DEV-005). (b) Top view of the top plate: four different spatial regions of the top plate loaded with semolina grains are indicated in black boxes. (c) The area occupied by the grains divided by the total plate area, as analysed from photos using ImageJ, are expressed in terms of normalised intensities. The normalised intensities of the four boxes are plotted with time when the plate is subjected to sinusoidal vibration.

Frictional contacts determine the interaction between granular particles. The role of the medium is also important to understand the bulk flow properties of granular media [10–12]. For dry granular materials, viscosity of air can be neglected. The absence of long-distance interactions between granular particles plays an important role in the measured dynamical properties. In dense granular systems, a network of particles interacting through friction develops and intensifies as jamming is approached [13]. The sizes of granular particles are big enough such that their thermal motion is unimportant. Hence they are called athermal systems. External energy is necessary for athermal particles to remain in motion. In the laboratory, granular particles are energised using a mechanical shaker which is capable of ex-

erting vertical vibrations. The particles harness the vibrational energy of the stage to remain mobile [14].

Due to its similarities with molecular or colloidal glasses [15, 16], granular materials serve as an excellent model system for studying several properties of glassy physics, such as dynamical heterogeneity and the correlated motion of its constituent particles [17, 18]. Jamming or dynamical arrest is extremely common in systems which we use in our everyday life. Dense granular systems have been explored to understand particle dynamics near the jamming transition [19]. Bidisperse driven granular systems have been reported to have heterogeneous dynamics near jamming [20]. The evolution of spatially heterogeneous dynamics and their connection with the local structure was examined for a quasi-two-dimensional granular system of air-fluidised beads approaching the jamming transition using a unique method based on local topology [21]. The cage effect of nearby particles influences particle dynamics near jamming [22]. The random close packing fraction for 2D discs is predicted to be approximately 82% [23]. It has been reported for 2D systems that the transition from at random close packing density goes from chaotic to non-chaotic while the dynamical length- and timescales diverge [24]. Evidence suggests that jamming exhibits properties of a continuous phase transition, including critical fluctuations. The concept of jamming extends to systems with varied particle shapes, obstacles, and longer-range interactions, leading to diverse jamming behaviours and potential applications in various fields, including active matter and quantum systems [25]. The influence of size polydispersity on jamming has not been substantially explored for granular materials. In practice, most industrial goods and natural substances are polydisperse. It has been reported that the glass transition point shifts to a higher volume fraction for higher particle size polydispersity [26]. Size polydispersity is an essential characteristic of granular materials. For instance, a broad variation of particle sizes in cement reduces porosity, strengthening the substance.

Using an electro-dynamic shaker vibrating vertically, we investigate the dynamics of dense packings of granular Teflon balls. The sample stage or plate is attached to

the shaker to conduct experiments in a quasi-2D configuration. A specific number of Teflon balls with varying diameters are mixed to simulate the top section of a Gaussian distribution. Polydispersity of the system (PDI) is determined from the ratio of mean and width of the Gaussian distribution to which the ball size distribution was fitted. Calculation of PDI has been discussed in section 6.2.1. of Chapter 6. The motion of the balls is captured with a DSLR camera. Experiments are conducted for two distinct polydispersities, and area fraction (A_p) is varied for these two PDIs to determine the effect of packing density on the heterogeneous dynamical behaviour of dense packings of granular balls. The images are analysed to track each particle individually. The trajectories of these balls are then utilised to determine the mean square displacements (MSDs). We investigate the dynamical heterogeneity by calculating the two-point correlation function (Q_2) and the four-point susceptibility (χ_4). The peak value of χ_4 is directly related to the extent of dynamical heterogeneities in the system. Finally, we demonstrate the growths of dynamical heterogeneity and number of correlated particles (N_{corr}) in a quasi-2D granular system as the area fraction approaches the random close packing fraction.

7.2 Materials and Methods

We use several Teflon balls having seven different diameters, D = 4, 4.5, 5, 5.5, 6, 6.5 and 7 mm, to perform our granular experiments. The Teflon balls (white colour) are smooth hard spheres and can mimic diffusive dynamics under vibration. The vibrating surface of the shaker (DEV-005, DESPL), where we study the quasi-2D dynamics of the granular particles, needs to be free from any tilt. The calculation of non dimensinal acceleration Γ is shown in section 2.2.7 (Chapter 2). A Nikon DSLR camera is mounted on an external stand to image the dynamics of vibrating Teflon balls from the top of the sample stage shown in Fig.7.1(a).

The shaker has four adjustable legs to align the top plate. To align the sample stage of the shaker, we use granular semolina particles. These grains can move very

easily on the plate under vibration. The images of the top plate is shown in Fig.7.1(b) and the region is divided into four boxes. A series of images are captured while vibrating the stage. The images are binarised by setting a threshold value during image analysis by maintaining semolina grains as white and the background plate as black. After binarising the images, we calculate the ratio of the area occupied by the white pixels (representing semolina grains, Fig.7.1(b)) within each box to the total area of that box. In Fig.7.1(c), the intensities of the four boxes, which we define as the ratio of the white pixels divided by the total number of pixels, are almost constant over a significant period of time. This indicates a proper alignment of the sample stage or the top plate of the shaker.

7.3 Results and Discussion

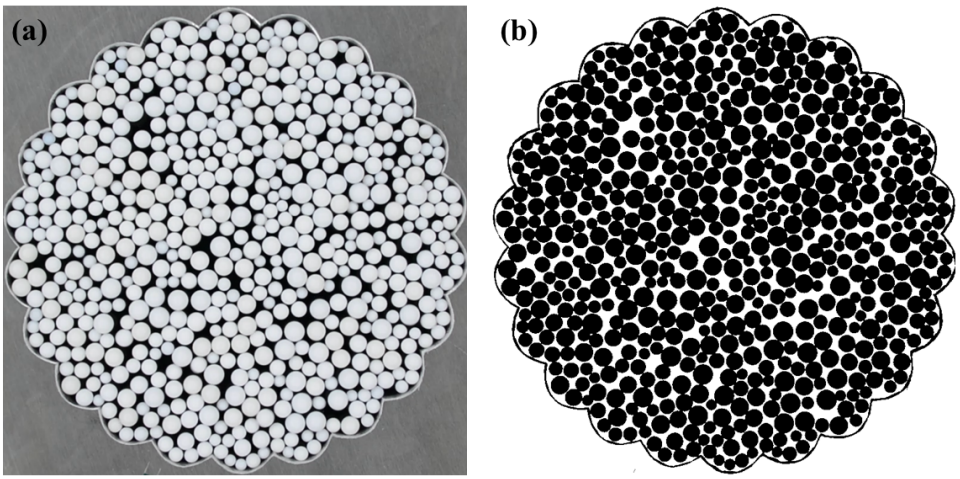

Figure 7.2: (a) The image of the sample plane is taken using the camera from the top. (b) The corresponding binary image is shown.

We use an electro-dynamic shaker to energise the Teflon balls so that we can study their dynamics. An external power supply is used to control the vibration of the shaker stage (anodised aluminium plate) by controlling the input current from

the power supply unit. In our experiments, we record video of vibrating Teflon balls for 5 mins at a frame rate of 29.97 fps using a Nikon DSLR camera set up above the sample stage. The recorded video is then sliced into frames. One of the frames is shown in Fig.7.2(a) where the observed white particles are the Teflon balls, the black colour comes from the stage below the particles and the grey boundary is a flower shaped aluminium plate used for confining the Teflon balls. For a circular boundary, the particles in contact with the boundary undergo a drift, which also affects the dynamics of the neighbours. Flower shaped confinement restricts the particles in the boundary from undergoing any drift. While tracking, we avoid the particles near the boundary to neglect boundary effects. The frames obtained are binarised using ImageJ software, as shown in Fig.7.2(b), to find the area fraction. The frame is first converted to a grey scale image after selecting the region of interest (ROI) in a frame. Every grey scale image is converted to a binary image by applying an intensity threshold. Then the pixels which have zero value in the binary image (Fig.7.2(b)) are counted to obtain the total area of the Teflon balls.

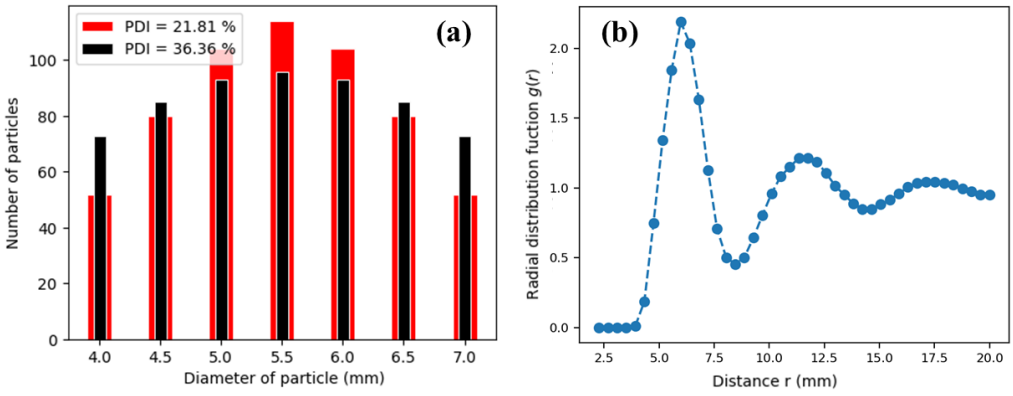

Figure 7.3: (a) Histogram plots of number of particles for two different polydisperse samples are shown. (b) Radial distribution function $g(r)$ *vs.* r is plotted for PDI = 21.81% at area fraction of 0.73.

We conduct granular experiments at two particle distributions with polydispersity indices of 21.81% and 36.36%. For each particle size distribution, we perform experiments at three different area fractions. The desired area fraction and particle size distribution are obtained by carefully placing appropriate number of Teflon balls

of different diameters on the sample plate. The number of Teflon balls of various diameters required to achieve the two PDIs (21.81% and 36.36%) for area fractions A_p = 0.73 and 0.77 is shown in the Fig.7.3(a). The number of Teflon balls to be placed on the sample plate to achieve the desired polydispersity is verified using particle detection method using Python v3.10. The 2D coordinates of Teflon balls obtained after tracking the particles is analysed to obtain the pair correlation function $g(r)$ using the following formula,

$$g(r) = \frac{1}{2N\pi r} \sum_i \sum_{i \neq j} \langle \delta(r - r_{ij}) \rangle \tag{7.1}$$

i and j are the particle index, δ is the delta function and N=40-50 is the total number of particles. We calculate $g(r)$, shown in Fig.7.3(b), by selecting some particles in the central region away from the boundary. We draw a circle around each particle selected in the central region of the plate and measure the distances of other particles which are within the radius. The radius of the circle is fixed to a value which is much larger than the particle sizes and much less than the system size. The $g(r)$ values are calculated by counting the number of particles within circles of different radii while ensuring sufficient averaging. Since these are hard spheres, the shortest possible distance between two particles should be larger than or equal to the smallest diameter. Since the diameters of Teflon balls are between 4 - 7 mm in diameter, we see from the Fig.7.3(b) that $g(r)$ becomes non zero around 4 mm and then rises and peaks around 7 mm before decreasing again. $g(r)$ tends to 1 as distance increases. The pair correlation function $g(r)$ obtained for our systems shows characteristics of amorphous nature of particle arrangements.

Initially, we apply a thorough mixing to the balls on the aluminium plate such that the initial positions of balls of different diameters are randomly distributed. To study the dynamics of the Teflon balls, we switch on the shaker at a fixed amplitude (47 μm) and frequency (78 Hz), and after 1 minute, we record a 5-minute video of the Teflon balls moving due to vibration of the sample stage. The series of images are used to track the centres of the particles and generate trajectories of each Teflon

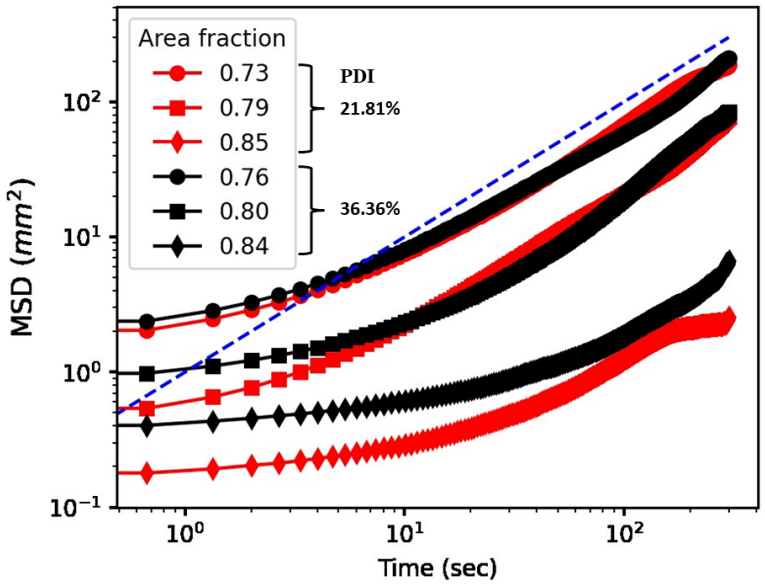

Figure 7.4: Mean square displacements (MSDs) are plotted at different area fractions for two different particle PDIs. The blue dashed line (slope = 1) represents diffusive nature of particle dynamics.

ball using a video spot tracker (Computer Integrated Systems for Microscopy and Manipulation) software. The ensemble-averaged mean square displacement (MSD) of each mixture having discrete PDIs and area fractions is calculated using the following formula,

$$< \Delta r^2(t) >= \frac{1}{N} \sum_i \langle (x_i(t_0 + t) - x_i(t_0))^2 + (y_i(t_0 + t) - y_i(t_0))^2 \rangle_{t_0} \tag{7.2}$$

where t represents the delay time while t_0 denotes the initial time of measurement of a particle trajectory. x_i and y_i are the coordinates of the i-th particle, N is the total number of particles, and $\langle\rangle$ is an average over t_0.

Since the computation time required to process the particle coordinates to calculate MSD for all frames is more than 12 hours, we skipped every 20 frames in between, resulting in a reduced frame rate of 1.5 frames/sec. Nevertheless, the MSD plotted with delay times in Fig.7.4 reflects the characteristic behaviour of particle dynamics even at reduced frame rate. In Fig.7.4, the dashed line indicates Brownian

dynamics. At a high particle area fraction, particle motion is constrained due to the jammed neighbourhood. In highly confined situations such as these, each particle can be thought to be constrained within a cage formed by its neighbours. This cage formation is more prominent at high packing fractions. At higher delay times, the cage relaxes, which is inferred from the rise in the MSD plot after the plateau like regime at lower times. The plateau regime gets more prominent as the packing fraction increases, as seen in Fig.7.4. This indicates that particles are trapped in the cage for longer times as the packing density increases, thereby inhibiting individual particle dynamics. Another important aspect that can be concluded from Fig.7.4 is the effect of the PDI on the average particle dynamics. The MSD values obtained for the system at area fractions A_p= 0.73, PDI 21.81% and A_p=0.76, PDI 36.36% clearly indicate enhanced dynamics due to increasing polydispersity even at higher area fraction. This points towards an increased cage rearrangement rate in the system caused by increased polydispersity of the particles.

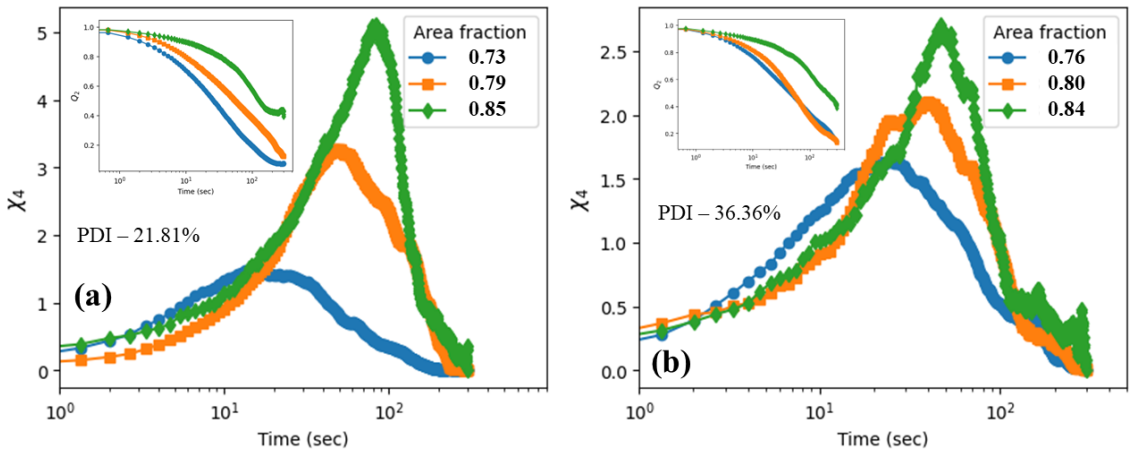

Figure 7.5: χ_4 *vs.* time is shown for (a) PDI = 21.81% and (b) PDI = 36.36% for different area fractions. The corresponding Q_2 are shown in the insets.

We calculate higher-order correlation functions to study the spatially heterogeneous dynamics in dense systems. Spatially heterogeneous dynamics (SHD) result in the correlated motion of neighbouring particles. SHD can be quantified using a four-point susceptibility function, $\chi_4(a,t)$, a measure of spatio-temporal fluctuations of the overlap order parameter Q_i. Q_i is a measure of overlap of two configurations

separated by a delay time t. We calculated Q_i using the following equations,

$$Q_i(a,t,t_0) = \exp\left(-\frac{\Delta r_i^2(t_0, t_0+t)}{2a^2}\right) \tag{7.3}$$

where $\Delta r_i(t_0, t_0+t)$ is the displacement of the i-th particle over delay time t from the initial time t_0, a is a probe length set by the extent of the dynamical heterogeneity of the dense system and N is the total number of particles. If the probe length is too small compared to the displacement of the particle, Q_i is small. On the other hand, if the probe length chosen is large, then Q_i has values close to one.

Two-point correlation function Q_2 is calculated by taking an average of Q_i over initial times t_0 and number of particles, N. The fluctuations in Q_i reveal spatio-temporal correlations present in the system, which is characterised by $\chi_4(a,t)$. Q_2 and $\chi_4(a,t)$ are calculated using the following equations [19],

$$Q_2(a,t) = \frac{1}{N}\sum_i \langle Q_i(a,t,t_0)\rangle_{t_0} \tag{7.4}$$

$$\chi_4(a,t) = N\left(\frac{1}{N}\sum_i \langle Q_i(a,t,t_0)^2\rangle_{t_0} - \frac{1}{N}\sum_i \langle Q_i(a,t,t_0)\rangle_{t_0}^2\right) \tag{7.5}$$

N is the total number of tracked particles, and <> is an average over t_0. χ_4 measures the spatiotemporal correlation between any two points over time t. We calculate $\chi_4(a,t)$ for a set of probe lengths and choose an optimal probe length a^* (Table.7.1) for which $\chi_4(a,t)$ shows the maximum peak height. The plots of χ_4 and Q_2 corresponding to a^* are shown in Fig.7.5. The plots of χ_4 obtained for three different area fractions are plotted for PDI = 21.81% in Fig.7.5(a) and PDI = 36.36% in Fig.7.5(b). As the area fraction increases, we observe that the peak height χ_4^*, characterising the spatial heterogeneities, increases for both PDIs shown in Table.7.1. χ_4^* essentially characterises the number of particles that are involved in cooperative rearrangements during the structural relaxation process. We also clearly observe that on increasing particle area fraction, particle dynamics slow down. This

PDI (%)	Area fraction (%)	Probe length a^* (mm)	Q_2^*	χ_4^*	N_{corr}
21.81	73.61	2.1	0.53	1.48	3.16
21.81	79.21	1.4	0.48	3.27	6.25
21.81	85.00	0.6	0.52	5.11	10.68
36.36	76.00	2.5	0.53	1.64	3.51
36.36	80.91	1.4	0.47	2.11	4.01
36.36	84.37	0.8	0.61	2.71	7.11

Table 7.1: Probe length where χ_4 peak is maximum, Q_2 value at the time where peak in χ_4 appears, peak value of χ_4 and number of correlated particles (N_{corr}) are tabulated for two PDIs at different area fractions.

is evident from the shift of the peak of χ_4^* to a longer delay times denoted by τ^*. Just by comparing χ_4^* for the two different PDIs, we confirm that PDI lowers SHD.

As seen in Fig.7.5, χ_4^* decreases due to increase in PDI, which indicates that system dynamics become less heterogeneous. A similar reduction has also been noted in the study conducted by Avila et al. [20]. The presence of elastic interactions contributes to enhance dynamical heterogeneity. When the coefficient of restitution is low, particles have the tendency to adhere together with minimal kinetic energy. This phenomenon can result in configurations having efficient packing. Our result can also be understood by considering the more efficient packing of the balls by filling available voids as the PDI increases. As the PDI increases for a fixed area fraction, the constituent particles can access various system configurations more efficiently since there is greater accessible space for movement. In order to estimate the characteristic lengthscales of these cooperatively rearranging regions in dense polydisperse granular packings, the number of correlated particles in the dynamically heterogeneous regions are estimated from the following equation [21],

$$N_{corr} = \frac{\chi_4^*}{1 - Q_2^*} \tag{7.6}$$

where χ_4^* is the peak value of χ_4 and, Q_2^* is the magnitude of Q_2 corresponding to the delay time at which the peak in χ_4 appears (shown in Fig.7.5). The number of correlated particles is calculated for all the area fractions at two different PDIs. The

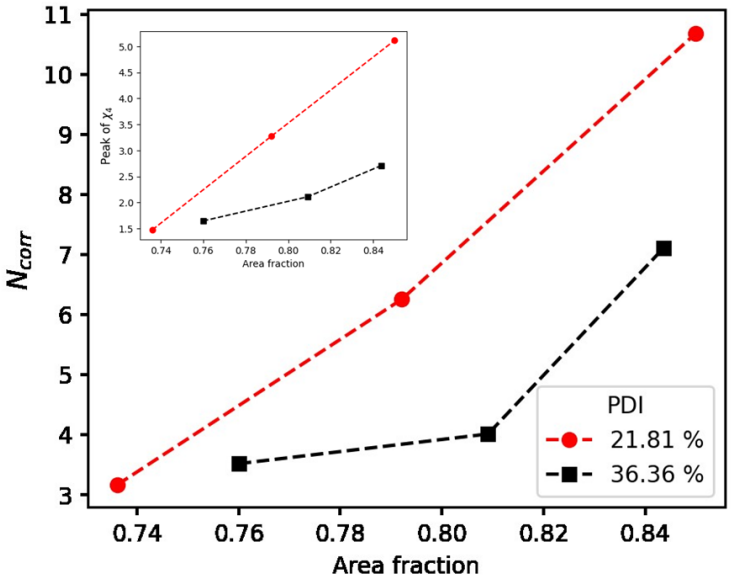

Figure 7.6: Number of correlated particles is plotted *vs.* area fraction for different PDIs. In the inset, the peak values of χ_4, χ_4^*, are shown.

data is plotted in Fig.7.6 and tabulated in Table.7.1. The sample characterised by higher PDI shows decreased cooperative movement of the particles. In the inset, the peak value of χ_4 is plotted *vs.* area fraction for both PDIs. As expected, we see that the systems get increasingly jammed as its area fraction is increased. From the experimental data, we conclude that increase in particle size polydispersity effectively unjams the system, resulting in reduced dynamical heterogeneities. The characteristic decay timescale τ^* when the system exhibits maximum dynamical heterogeneity shifts to earlier times with increasing PDI. This implies that the system exhibits substantially faster dynamics for increasing particle PDIs and for decreasing area fractions. Both these factors can therefore contribute to unjamming of the system. Hence, increasing PDI speeds up the cage rearrangement process, as the wider distribution of particle sizes increases average particle mobility and eventually unjams the system.

7.4 Conclusions

Polydisperse granular particles under vertical vibration are studied to verify the effect of size distribution on dynamical heterogeneities in dense systems. A broader distribution of particle sizes fluidizes the system. Such fluidization smears out dynamical heterogeneities and shifts the jamming transition point to higher particle area fraction. Different bidisperse granular systems [20, 27] have been explored in the past to investigate dynamical heterogeneity. Here, we use Teflon balls of seven different sizes to imitate a Gaussian distribution with a discrete size polydispersity for studying dynamical heterogeneities in dense particle packings with area fraction approaching the random close packing fraction.

We measure mean square displacements of the size polydisperse Teflon balls to analyze the average dynamics of the particles. At similar area fraction, the Teflon balls with higher polydispersity show higher average displacements when compared to particle packings having lower PDI. Q_2 is calculated to compute the characteristic relaxation timescale and χ_4 is calculated to estimate the dynamical heterogeneity present in the system. The characteristic relaxation time required for Q_2 to decay and the peak height of χ_4 to decrease are both seen to reduce with decreasing area fraction and increasing PDI. Finally, the number of correlated particles is calculated.

Understanding the role of PDI near the jamming transition will certainly help to optimize flow properties of granular systems while ensuring the desired output of these dense systems. More extensive studies for different PDIs will be performed to quantify the growth of correlated motion of constituent particles near the jamming transition.

Bibliography

[1] Robert Leslie Brown and John Colin Richards. *Principles of powder mechanics: essays on the packing and flow of powders and bulk solids*, volume 10. Elsevier, 2016.

[2] Pierre-Gilles de Gennes. Reflections on the mechanics of granular matter. *Physica A: Statistical Mechanics and its Applications*, 261(3-4):267–293, 1998.

[3] G. D. R. Midi. On dense granular flows. *The European Physical Journal E*, 14:341–365, 2004.

[4] Daniel L. Lakeland, Amy L. Rechenmacher, and Roger G. Ghanem. Towards a complete model of soil liquefaction: the importance of fluid flow and grain motion. *Proceedings of the Royal Society A: Mathematical, Physical and Engineering Sciences*, 470, 2014.

[5] P. Jop, Yoel Forterre, and Olivier Pouliquen. A constitutive law for dense granular flows. *Nature*, 441:727–730, 2006.

[6] Mehdi Bouzid, Adrien Izzet, Martin Trulsson, Éric Clément, Philippe Claudin, and Bruno Andreotti. Non-local rheology in dense granular flows. *The European Physical Journal E*, 38:1–15, 2015.

[7] Lydie Staron, Pierre-Yves Lagr'ee, and Stéphane Popinet. The granular silo as a continuum plastic flow: The hour-glass vs the clepsydra. *Physics of Fluids*, 24:103301, 2012.

[8] Dapeng Bi, Jie Zhang, Bulbul Chakraborty, and Robert P Behringer. Jamming by shear. *Nature*, 480:355–358, 2011.

[9] Jie Ren, Joshua A Dijksman, and Robert P Behringer. Reynolds pressure and relaxation in a sheared granular system. *Physical Review Letters*, 110(1):018302, 2013.

[10] Christophe P. Goujon, Nathalie Thomas, and Blanche Dalloz-Dubrujeaud. Monodisperse dry granular flows on inclined planes: Role of roughness. *The European Physical Journal E*, 11:147–157, 2003.

[11] Abhinendra Singh. Micro-macro and rheology in sheared granular matter. 2014.

[12] Jonathan Barés, Manuel Cárdenas-Barrantes, David Cantor, Mathieu Renouf, and Émilien Azéma. Softer than soft: Diving into squishy granular matter. *Papers in Physics*, 2022.

[13] Lou Kondic, Miroslav Kramár, Lenka Kovalčinová, and Konstanin Mischaikow. Evolution of force networks in dense granular matter close to jamming. In *EPJ Web of Conferences*, volume 140, page 15014. EDP Sciences, 2017.

[14] Nitin Kumar, Harsh Soni, Sriram Ramaswamy, and AK Sood. Flocking at a distance in active granular matter. *Nature Communications*, 5(1):4688, 2014.

[15] Beatriz Seoane and Francesco Zamponi. Spin-glass-like aging in colloidal and granular glasses. *Soft Matter*, 14(25):5222–5234, 2018.

[16] Takahiro Hatano. Rheology and dynamical heterogeneity in frictionless beads at jamming density. *Journal of Physics: Conference Series*, 319:012011, 2008.

[17] Juan P. Garrahan. Dynamic heterogeneity comes to life. *Proceedings of the National Academy of Sciences*, 108:4701 – 4702, 2011.

[18] Francis W Starr, Jack F Douglas, and Srikanth Sastry. The relationship of dynamical heterogeneity to the adam-gibbs and random first-order transition theories of glass formation. *The Journal of Chemical Physics*, 138(12), 2013.

[19] Olivier Dauchot, Guillaume Marty, and Giulio Biroli. Dynamical heterogeneity close to the jamming transition in a sheared granular material. *Physical Review Letters*, 95(26):265701, 2005.

[20] Karina E Avila, Horacio E Castillo, Andrea Fiege, Katharina Vollmayr-Lee, and Annette Zippelius. Strong dynamical heterogeneity and universal scaling in driven granular fluids. *Physical Review Letters*, 113(2):025701, 2014.

[21] Adam Ross Abate and DJ Durian. Topological persistence and dynamical heterogeneities near jamming. *Physical Review E*, 76(2):021306, 2007.

[22] G Marty and Olivier Dauchot. Subdiffusion and cage effect in a sheared granular material. *Physical Review Letters*, 94(1):015701, 2005.

[23] James G. Berryman. Random close packing of hard spheres and disks. *Physical Review A*, 27:1053–1061, 1983.

[24] Edward J Banigan, Matthew K Illich, Derick J Stace-Naughton, and David A Egolf. The chaotic dynamics of jamming. *Nature Physics*, 9(5):288–292, 2013.

[25] C Reichhardt and CJ Olson Reichhardt. Aspects of jamming in two-dimensional athermal frictionless systems. *Soft Matter*, 10(17):2932–2944, 2014.

[26] Vasili Baranau and Ulrich Tallarek. Random-close packing limits for monodisperse and polydisperse hard spheres. *Soft Matter*, 10(21):3826–3841, 2014.

[27] R Candelier, Olivier Dauchot, and G Biroli. Dynamical facilitation decreases when approaching the granular glass transition. *Europhysics Letters*, 92(2):24003, 2010.

Chapter 8

Summary and future directions

This chapter summarises the key findings of this thesis and addresses the prospect for future research on the topics explored here. One of the main objectives of this thesis is to understand the underlying microstructure of Laponite suspensions using various techniques. The rheological properties of Laponite suspension are governed by these structures that form spontaneously with time. The dynamics of particles in the Laponite suspension are highly correlated to its microstructure. Using falling ball viscometry and optical tweezing methods, we investigated the viscoelastic properties of Laponite suspension at different lengthscales. We also conducted experiments with Laponite suspensions by applying AC electric field, which enabled us to control the evolution of these microstructures. The thesis also presents careful quantification of dynamical heterogeneity in dense colloidal and granular suspensions. Polydisperse particles were used to study dynamical heterogeneity in dense packings. Our findings addressed the effect of size polydispersity on particle dynamics. We demonstrated experimentally that increasing particle polydispersity is an additional route for unjamming dense granular and colloidal systems.

In Chapter 3, falling ball experiments were carried out by dropping millimetre-sized balls into Laponite suspensions of different ages. In contrast to a ball falling through a Newtonian fluid, balls falling through Laponite suspensions did not reach a steady state during the experimental time window. Using a simple model, we suc-

cessfully extracted the destructuring rates of Laponite suspension microstructures for different suspension ages and ball sizes. A simple model was proposed to explain the progressive increase in velocity of the falling ball within the experimental time range accessible in these measurements. We limited our study of the falling ball to a regime that can be described by the simplest mathematical model that measured the steady rise of ball velocity due to shear thinning of the Laponite suspension in the neighbourhood of the ball. The experiments described in this study provided important insights on the motion of macroscopic objects falling through thixotropic fluids and the physical aging process of the medium at the lengthscale of the falling ball.

Chapter 4 discussed the correlation between microscopic viscoelasticity and the structure of Laponite clay suspensions. We investigated the controlled movements of an optically trapped micron-sized colloidal probe particle suspended in an aging Laponite suspension as the underlying Laponite microstructures evolve gradually. Optical tweezer (OT) based oscillatory active microrheology studies were implemented to explore the mechanical responses of the evolving microstructures. Using cryogenic field emission scanning electron microscopy (cryo-FESEM), we investigated the average pore sizes of the Laponite microstructures for different sample concentrations and aging times. Combining our OT and cryo-FESEM data, we reported, for the first time to the best of our knowledge, an inverse correlation between the crossover modulus and the average pore diameter of the microstructures in the aging suspension for different suspension concentrations. Our findings can be used to investigate the consequences of local sample heterogeneities during the transport of micron-sized particles through complex environments, such as in drug delivery. Laponite is utilised as a rheological modifier in material processing applications, and knowledge of micron-scale local dynamics is required to achieve the desired output.

In Chapter 5, we investigated the rheological properties of Laponite suspensions subjected to an external AC electric field using a rheometer and an optical tweezer. The complex viscosity measured by using amplitude sweep oscillatory rheol-

ogy demonstrated a non-monotonic response with increasing electric field strengths. We demonstrated that the AC electric field could be used to influence the mobility of charged clay particles. Using an electric field, therefore, we were able to regulate the gelation caused by structure development in an aging Laponite suspension. These results can be beneficial in industrial scenarios in which Laponite is utilised as a rheological modifier, such as paint, cosmetics, etc. We note that other charged clays should also show similar behaviours under similar conditions. The controlled aging of clay suspensions using an electric field is an intriguing topic and depends sensitively on clay and salt concentration, age and medium temperature. In future research, these parameters and also the frequency of the electric signal could be altered to study controlled aging. Furthermore, the charges on the rims of Laponite particles could be altered by changing solution pH to conduct additional tests.

Chapter 6 presented a combined experimental and numerical investigation of the dynamics of jammed packings of colloidal microgel particles in aqueous suspensions with continuous particle size distributions. We computed mean square displacements to estimate the average dynamics of particles in dense suspensions and extracted multipoint correlation functions to characterise their heterogeneous dynamics. Our findings showed that caging of particles weakens as PDI increases. The rapid dynamics of smaller particles in dense polydisperse systems permitted faster cage rearrangements and shortened cage-breaking timescales, which accelerated structural relaxation. At the timescale of structural relaxation, the dynamics were expected to be most heterogeneous due to significant non-Gaussian particle displacements during cage rearrangement. For suspensions composed of particles with narrower size distributions, the increase in correlations was significantly higher. By carefully performing experiments and running molecular dynamics simulations, we demonstrated the existence of heterogeneous and correlated dynamics in dense suspensions, pointing to the analogous nature of the jamming and glass transitions.

Chapter 7 reported the dynamics of dense quasi-two-dimensional packings of granular balls using a vertically vibrated electrodynamic shaker. To conduct studies

in a quasi-2D configuration, the sample stage or plate was connected to the shaker. The effect of particle size distribution on dynamical heterogeneities in dense systems was examined by vibrating polydisperse granular particles vertically. The jammed state of the system fluidised when the particle size distribution was wider. Such fluidisation smoothed out dynamical heterogeneities and shifted the jamming transition point to a higher area fraction of particles. Finally, the number of particles exhibiting correlated motion was determined. Understanding the role of PDI at the jamming transition could assist in optimising granular systems while ensuring the desired output and flow qualities. To assess the increase in correlated motion of constituent particles approaching the jamming transition, more in-depth research needs to be conducted by changing interaction between particles and particle shape.

To conclude, this thesis examines several issues concerning the dynamics and rheology of jammed suspensions. These studies form a small subset of the several intriguing issues in this area that remain to be addressed. More such studies on related topics will be undertaken in future research.